UNIVERSITÀ DEGLI STUDI DI PADOVA

Dipartimento di Fisica e Astronomia "Galileo Galilei"

Master Degree in Physics

Final Dissertation

Systematic study of the structure of medium-mass mirror nuclei

Thesis supervisor

Prof. Silvia Monica Lenzi

Candidate

Franco Morosin

Anno Accademico 2024/2025

Contents

Abstract

The nuclear force is approximately independent of the nucleon charge. This feature is reflected in the similar structure of mirror nuclei, where the number of protons and neutrons is interchanged. Small differences in the excitation energies of analogue states arise primarily from the Coulomb interaction and to a lesser extent from isospin-breaking components of the nuclear interaction. Recent theoretical and experimental studies have further highlighted the important role of low-l orbitals, which influence not only these energy differences but also broader properties such as neutron skin.

This thesis presents a systematic study of Mirror Energy Differences (MED) for nuclei with masses $19 \leq A \leq 35$ in the sd-shell, carried out within the nuclear shell-model framework. MED act as a magnifying lens for probing the microscopic structure of excited states, providing insights into pairing correlations, angular-momentum–dependent structural evolution, and changes in nuclear radii. For the first time, methods of calculation largely developed for the fp-shell have been applied systematically to both natural-parity positive states within the sd-shell and negative-parity intruder states arising from cross-shell excitations.

The analysis, performed in nuclei with isospin values of up to $T = 2$ for positive parity and up to $T = 3/2$ for negative parity, was carried out using the ANTOINE shell-model code, with effective interactions tailored to the sd-shell. The results demonstrate that the adopted theoretical framework reproduces the main experimental trends. Deviations, particularly at high spin, are interpreted as a consequence of valence-space truncations and the growing role of core excitations, a distinctive feature compared with fp-shell nuclei. Moreover, single-particle energy corrections are found to be larger than those in the fp-shell, emphasising the sensitivity of the sd-shell nuclei to interaction details.

Beyond reproducing the available experimental data, the present calculations also predict yet unobserved states, providing valuable guidance for future measurements. The study establishes a solid framework for extending MED analyses in the sd-shell and for addressing Triplet Energy Differences (TED). It further opens the way to investigations of electromagnetic transitions and to the study of MED in mirror nuclei of astrophysical interest, where sd-shell systems play a central role in explosive stellar nucleosynthesis.

Chapter 1

Introduction

Symmetry is one of the fundamental and most powerful concepts in modern physics, after its introduction by E. Nöther. Symmetries, in fact, are intimately linked to conservation laws and conserved quantities, the latter being fundamental in quantum mechanics because they lead to good quantum numbers.

Along these lines, Heisenberg formulated the notion of isospin, which allows us to study the symmetry between protons and neutrons in an atomic nucleus. The concept of isospin and its formalism are based on the fact that we can see the proton and the neutron as different states of a doublet called the nucleon. Using isospin in nuclear physics, one can test the other two keystones: charge symmetry, which tells us that neutron-neutron and proton-proton interactions are equal, so $V_{nn} = V_{pp}$, and charge independence, $V_{nn} + V_{pp} = 2V_{np}$. The latter implies that all eigenstates of a system of two identical nucleons (i.e. nn or pp) must also be eigenstates of the mixed np system, as these configurations correspond to isospin $T = 1$ states. However, the reverse does not hold, since the np can additionally access states with isospin $T = 0$, which are antisymmetric in isospin and hence forbidden for identical nucleon pairs by the Pauli exclusion principle, see Fig.1.1.

By observing, and moving from the valley of stability towards driplines along the *Segrè chart*[1] (Fig.1.3) one can define isobars, which are nuclei with the same mass $A=N+Z$, but different number of protons and neutrons. States of isobaric nuclei with the same total angular momentum $\vec{J}$, parity, wavefunctions, and isospin $\vec{T}$ are called Isobaric Analogue States=*IAS* and they are degenerate in energy if any symmetry breaking mechanism is absent. So, if even small differences in energies are present, these can be related to electromagnetic origin attributable to the numerical imbalance[2] between protons and neutrons.

The IAS energies differ from each other by a quantity known as *Coulomb Displacement Energy* (CDE) that amount approximately to tens of MeV.

Normalising energies with respect the ground states, another quantity can be introduced: the *Coulomb Energy Differences* (CED), which takes into account the displacement in energy excitation. Isobaric analogue states (IASs) are expected to exhibit slight variations with increasing spin, mainly because of the influence of the Coulomb energy. In fact, this can subtly modify the structure of nuclear orbitals, consequently influencing the wavefunctions of the excited states.

Looking again to the nuclear chart one can define *mirror nuclei*, which are those with same mass

---

[1]Or *chart of nuclides*: it is the "map" of nuclear physics, playing the analogue role of Mendeleev in this context.
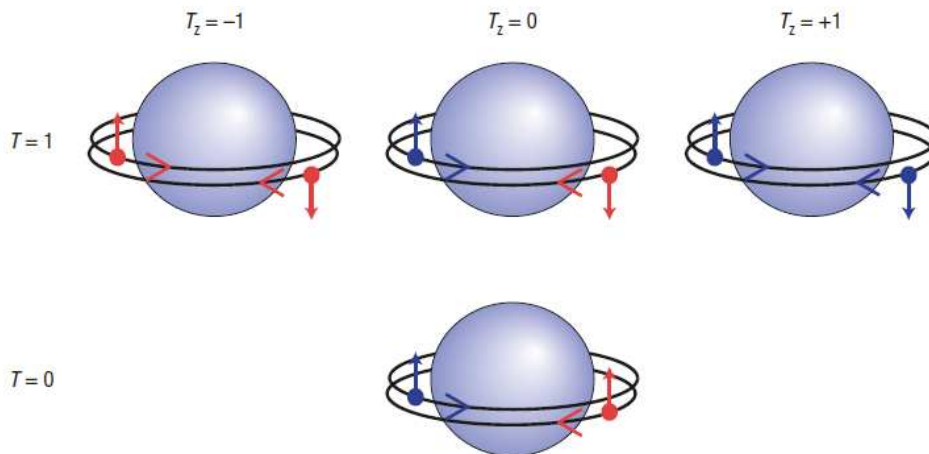[2]assuming equal mass A

Figure 1.1: Nucleon pairs. Schematic representation of the different nuclear Cooper-type pairs. The valence neutrons (blue) or protons (red) that form the pair occupy time-reversed orbits (circling in opposite directions). If the nucleons are identical they must have antiparallel spins—a configuration that is also allowed for a neutron–proton pair (top). These are isovector pairs. The configuration with parallel spin is only allowed for a neutron–proton pair (bottom). This is the isoscalar pair. Ref.[46].

A, but reversed number of protons and neutrons[3]. In this context, the study of the differences in excitation energy between analogue states of pairs of mirror nuclei leads to define the *Mirror Energy Differences* (MED):

$$MED_J^{exp} = E_J(Z_>) - E_J(Z_<)$$

whereas $E_J(Z_>)$ denotes the excitation energy of the state with angular momentum J in the nucleus with the largest Z among those that form a mirror pair. Furthermore, of capital interest in the framework of the nuclear shell model is the study of MED as a function of angular momentum J to obtain information regarding the violation effects of isospin conservation and evolution of the nuclear structure. An example can be seen by observing Fig.1.2.

Bentley and Lenzi [3] successfully implemented this strategy in nuclei with mass range $A = 40 - 55$ using the nuclear shell model in the *fp*-shell.
The purpose of this thesis is to test this strategy for nuclei belonging to the *sd*-shell (in this case $A = 19 - 35$, also predicting some values for states not yet experimentally obtained.

In *Chapter 2* an overview of the Shell Model in nuclear physics is presented, also introducing the code used to perform calculations.
The concept of isospin and its implications in the definition of mirror nuclei and mirror energy differences are treated in *Chapter 3*, while the complete systematic study of MED in the *sd*-shell for both positive and negative parity states is performed in *Chapter 4*. The analysis was conducted following increasing isospin values: from $T = \frac{1}{2}$ to $T = 2$ for states J^+ and from $T = \frac{1}{2}$ to $T = \frac{3}{2}$ for states J^-.
In the final *Chapter 5*, the conclusions of this thesis are presented, as well as potential directions for future research.

---

[3]Given two nuclear species (Z_1, N_1) and (Z_2, N_2), they are mirror if $Z_1 = N_2$ and $Z_2 = N_1$.
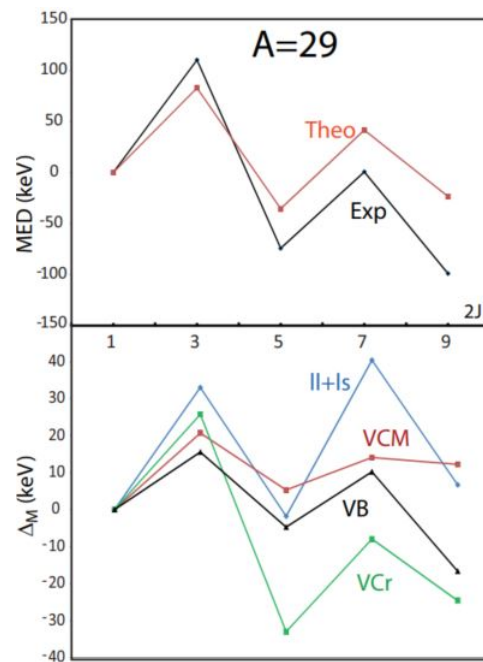
Figure 1.2: Example of MED for the T = 1/2 yrast states in the mirror pair ^{29}P$-^{29}$Si. The lower panel shows the contribution of the different components to the MED. Ref.[31].
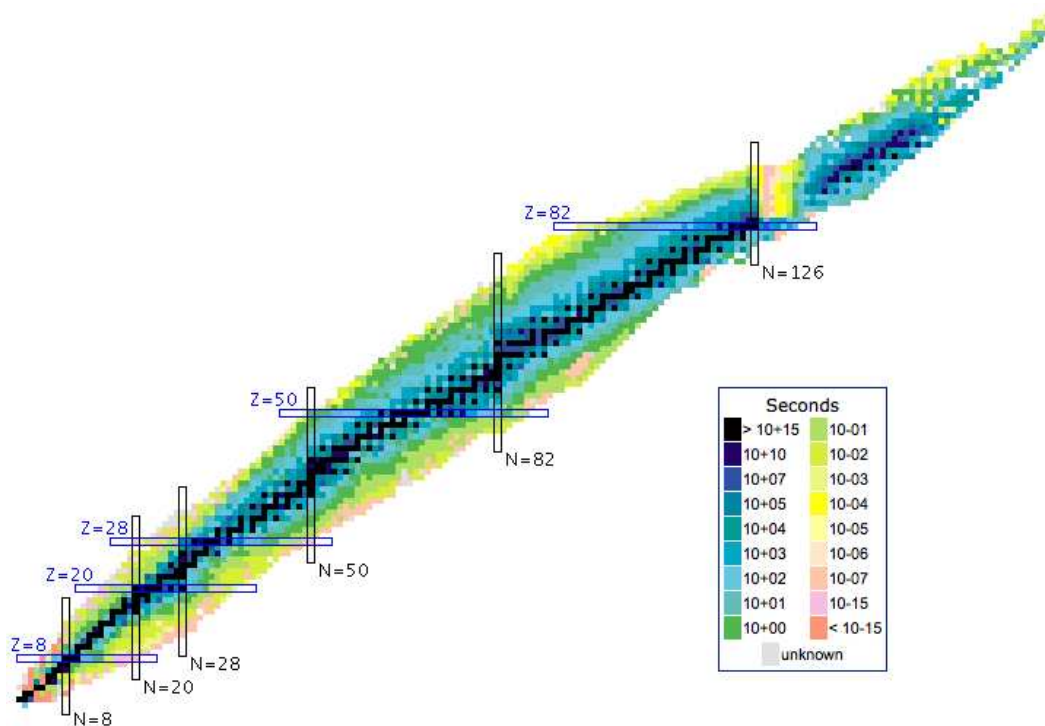
Figure 1.3: *Segrè Chart* in which magic numbers are highlighted and the colours encoded information regarding the half-life of each nuclide. Adapted form [36].

Chapter 2

Theoretical framework

In this chapter, after a brief survey on the experimental Shell Model evidences, the theoretical framework necessary for the development of the thesis work will be introduced. The main references are [5, 14, 24, 25].

2.1 Shell Model experimental evidences

There are a number of experimental facts confirming the validity of shell model and so the shell structure of the nucleus:

- Nuclear mass measurements, when graphed against their neutron number N or proton number Z, reveal systematic deviations from the liquid-drop model. These deviations show extra binding energy at the so-called magic numbers $Z, N = 2, 8, 20, 28, 50, 82, 126$ and reduced binding energy for located nuclei midway between these closed shells, see Fig. 2.1;
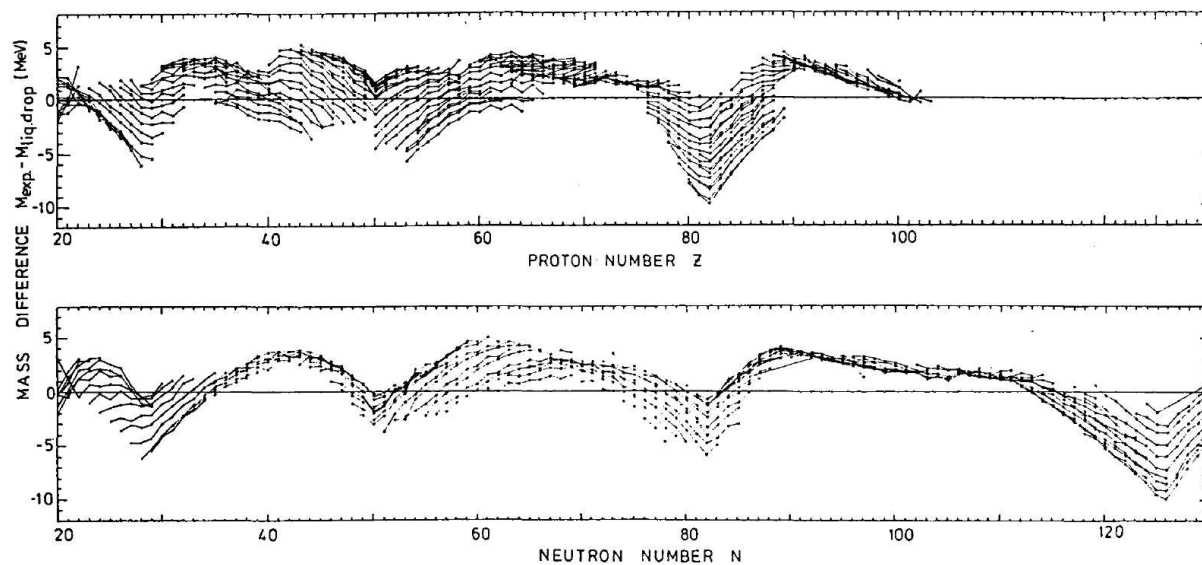
Figure 2.1: Deviation of nuclear masses from their mean (liquid drop) values as a function of Z or N. Taken from [25], adapted from [34].

- Shell structure is underlined in the discrete strength distribution in nucleon-transfer reactions, for example, the pick-up reaction $^{206}Pb(^3He,d)^{209}Bi$ in nucleon (two-nucleon separation energies, see Fig. 2.2;
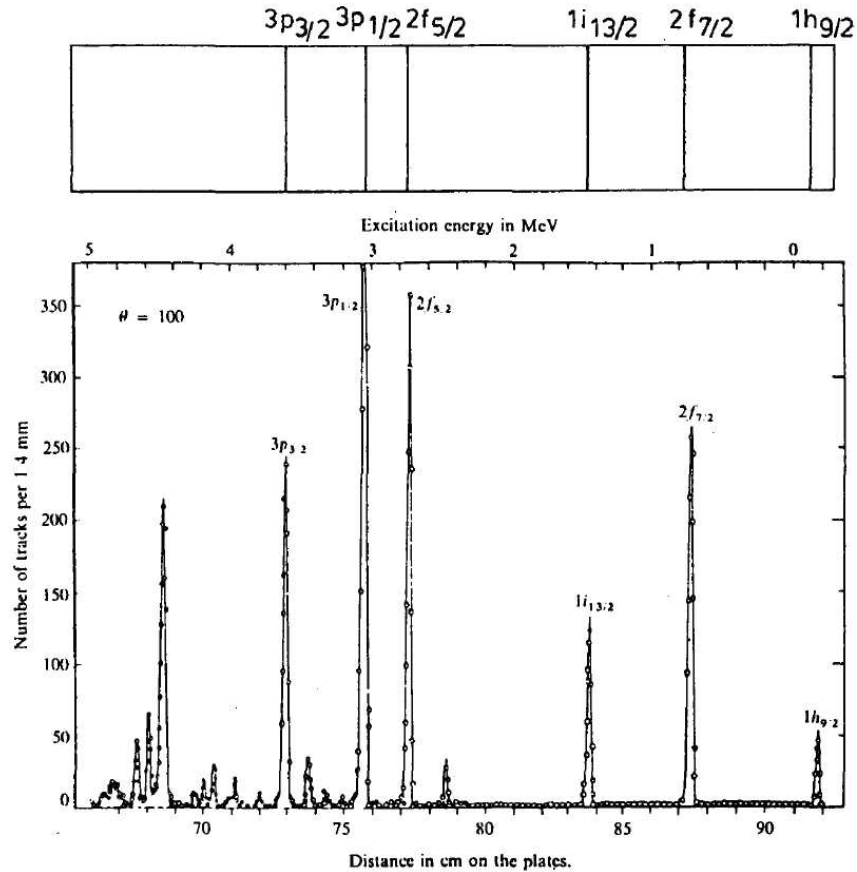
Figure 2.2: Single-nucleon states in ^{209}Bi: the upper figure shows the proton single-nucleon states corresponding to the spectra below; in the lower picture the spectra obtained from the pick-up reaction $^{206}Pb(^3He,d)^{209}Bi$ is shown. Refs. [25, 28].

- Even-even nuclei located near the valley of β-stability and having both proton and neutron numbers equal to magic values, such as $N = 8, 20, 28, 50, 82, 126$, exhibit unusually high excitation energies for their first excited states relative to neighbouring nuclei. As said before, this is similar in atomic physics: atoms with completely filled electronic (sub)shells also have higher first excitation energies than those with partially filled shells, leading to the emergence of analogous magic numbers in both systems, see Fig. 2.3.
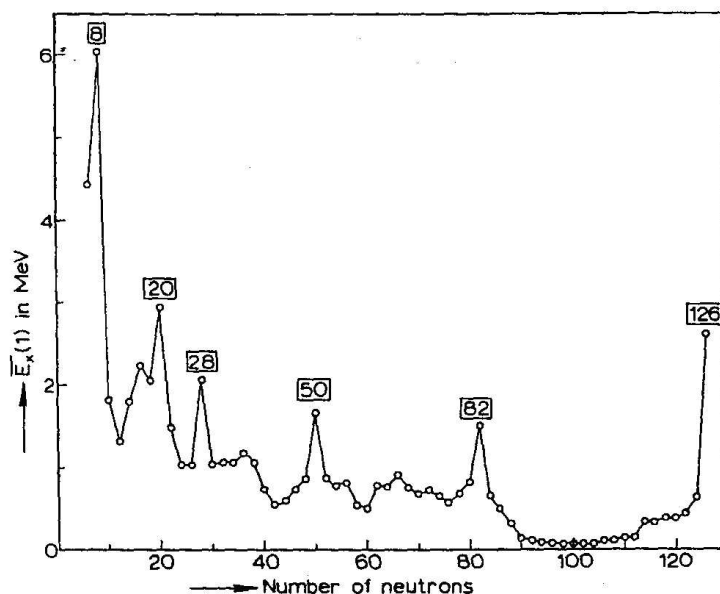
Figure 2.3: The average excitation energies of the first-excited states in doubly-even nuclei, mostly $J^{\pi} = 2^{+}$ level, plotted as a function of the N number. Refs. [13, 25, 28].

2.2 The Nuclear Shell model

Following the discovery of the neutron by Chadwick in 1932, Ivanenko and Gapon, inspired by the atomic model, introduced the first rough idea of a shell model that incorporates proton-neutron interactions [21]. Shortly thereafter, Heisenberg proposed the isospin symmetry, treating protons and neutrons as two states of the same particle, while Majorana and Wigner contributed to the formulation of the nucleon-nucleon force, a short-range, attractive interaction largely charge independent and capable of overcoming Coulomb repulsion. In the 1950s, the modern nuclear shell model was independently developed by Goeppert-Mayer and Jensen, introducing spin-orbit coupling to explain nuclear magic numbers. Although the early models assumed charge symmetry and independence, it is now understood that these are approximate, broken by electromagnetic effects and isospin-violating components in the strong interaction.

As said, the nuclear shell model was introduced, as we know it today, by Mayer and Jensen [23, 32] to solve the puzzle of the experimental observed regularities of nuclear properties related to N and Z numbers: 2, 8, 20, 28, 50, 82, 126, the so-called *magic numbers*. Unlike other models known at the time (i.e. *Liquid Drop Model*), the introduction of the shell model led to a match between theoretical predictions and experimental data on magic numbers. Since then, the shell model has been developed to accurately describe low-energy nuclear structures of nuclei with light- and medium-mass numbers, as well as the decay processes involved.

The name of the model clearly recalls the atomic shell model. The analogy lies in the fact that magic numbers correspond to particularly stable configurations, leading to peaks in separation energy near shell closures. Stable configurations are associated with stable nuclei, which are geometrically spherical and exhibit reduced collective behaviour. It is a quantum many-body model in which the A nucleons forming the nucleus interact through nuclear and Coulomb forces, mediated by a mean field. This is made possible through the following approximations:

- Each nucleon in an A-nucleon system moves independently in an average potential, produced by $\frac{A(A-1)}{2}$ pairs of nucleon-nucleon (NN) interactions in the nuclear medium. Higher

body interactions, such as *NNN* can be effectively thought as in-medium NN interactions. A further distinction must be made, namely the *NN* interaction in a nuclear medium is different from the free *NN* interaction: the free nuclear *NN* interaction is strongly repulsive at short distances and attractive at larger distances and includes non-central and spin-dependent forces that attach two nucleons to a constant distance of about 1 *fm*. This is guaranteed by the antisymmetric nature of fermionic wavefunctions and by the Pauli principle.

Further information regarding the meson exchange theories describing *NN* potential is reported in Fig.2.4.
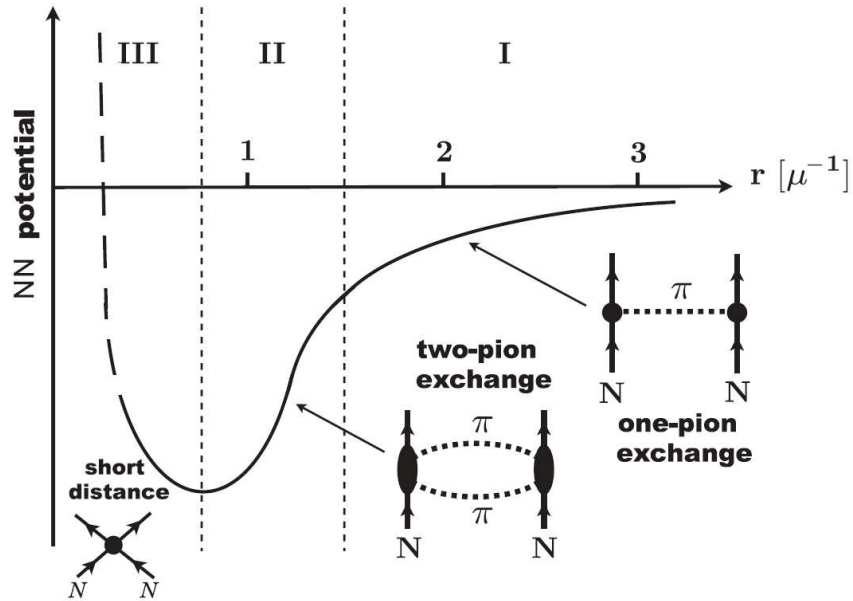
Figure 2.4: *Hierarchy scales of NN potentials type: NN* distance r is given in units of the pion's wavelength $\mu^{-1} \approx 1.4fm$. **Region I** ($r \geq 1.5fm$): π-exchange potential; **region II** ($r \approx 0.8 \div 1.5fm$): $\pi\pi$-exchange potentials; **region III** ($r \leq 0.5fm$): relativistic regime, so multi-pion or heavy-meson exchange potential is needed. Refs.[28, 44, 48].

- Each particle is subject to a central force responsible for the existence of bound states in its motion.

Normally, nucleons will first occupy the lowest energy states, until they reach the Fermi energy E_F. So, a nucleon with energy $E < E_F$ cannot move freely toward a different state because all the others are just saturated. In this way energy and momentum exchange is inhibited by Pauli principle.

2.2.1 The Non-interacting Shell model

In a more general situation, using the approximations exposed before, one can build the non-interacting Shell Model (or, single-particle Shell Model), described by the following Hamiltonian:

$$H_0 = \sum_{i=1}^{A} h_{0i} = \sum_{i=1}^{A} (K_i + U_i) \tag{2.1}$$

whereas the h_{0_i} are the single-particle Hamiltonians, K_i and U_i are respectively the single-particle kinetic and potential term. This arises from the one-particle Schrödinger equation,

describing a nucleon moving in a central spherically symmetric potential:

$$(K + U(r))\phi_\alpha(\mathbf{r}) = \epsilon_\alpha \phi_\alpha(\mathbf{r}) \tag{2.2}$$

in which α is a set of quantum numbers, ϵ_α are the discrete single-particle energies and $\phi_\alpha(\mathbf{r})$ are the single-particle wave functions solutions of the one-body Schrödinger equation. The latter form a complete set of orthonormal states

$$\int \phi_\alpha^*(\mathbf{r})\phi_\alpha(\mathbf{r})\,d\mathbf{r} = \delta_{\alpha\alpha'} = \begin{cases} 1, & \text{for } \alpha' = \alpha, \\ 0, & \text{for } \alpha' \neq \alpha, \end{cases} \tag{2.3}$$

where α is a set of quantum numbers. The nuclear state is described by an anti-symmetrized many-body wave function, specifically a Slater determinant constructed from the single-particle wave functions of the individual nucleons:

$$\Psi(\vec{r}_1, \ldots, \vec{r}_A) = \frac{1}{\sqrt{A!}} \det \begin{pmatrix} \phi_1(\vec{r}_1) & \cdots & \phi_A(\vec{r}_1) \\ \phi_1(\vec{r}_2) & \cdots & \phi_A(\vec{r}_2) \\ \vdots & \ddots & \vdots \\ \phi_1(\vec{r}_A) & \cdots & \phi_A(\vec{r}_A) \end{pmatrix} \tag{2.4}$$

in which $\Psi(\vec{r}_1, ..., \vec{r}_A)$ is the many-body wave-function, $\phi_A(\vec{r}_A)$ are the single-particle wave-functions and A labels the mass number.

Therefore, the eigenproblem can be rewritten as

$$H_0 \left| \Psi \right\rangle = E \left| \Psi \right\rangle = \sum_i \epsilon_i \left| \Psi \right\rangle \tag{2.5}$$

considering E as the total energy of the multi-particle state. Once this approximation has been imposed, one has to choose a single-particle potential to solve the full problem. A realistic and common choice is the Woods-Saxon (WS) potential

$$\text{U}_{\text{WS}}(r) = \frac{V_0}{1 + e^{(r-R_0)/a}} \tag{2.6}$$

in which $V_0 \approx -50$ MeV is a constant well depth, $R_0 = r_0 A^{\frac{1}{3}}$ describes the potential range, with $r_0 \approx 1.2$ fm, while $a \approx 0.7$ fm is a constant that measures the surface diffusion, or *skin thickness*. The WS potential is a phenomenological model that approximates the mean-field potential experienced by nucleons inside the nucleus. It is shaped after the observed nuclear matter density profile and is widely used to fit experimental observables such as energy levels, radii, and scattering data. Despite having an analytic form, the Woods–Saxon potential does not admit exact solutions, so the eigenstates must be computed numerically.

A more practical and analytically solvable choice is the harmonic oscillator (HO) potential Fig.2.5, due to its numerous symmetries and characteristics

$$U_{HO}(r) = \frac{1}{2} M_N \omega^2 r^2 \tag{2.7}$$

describing an isotropic tridimensional harmonic oscillator of a nucleon with mass M_N and ω oscillation frequency. Implementing it in the Schrödinger equation, one gets

$$h_0 \phi(\mathbf{r}) = \left(-\frac{\hbar^2}{2M_N}\nabla^2 + \frac{1}{2}M_N\omega^2 r^2 \right) \phi(\mathbf{r}) = \epsilon \phi(\mathbf{r}) \tag{2.8}$$
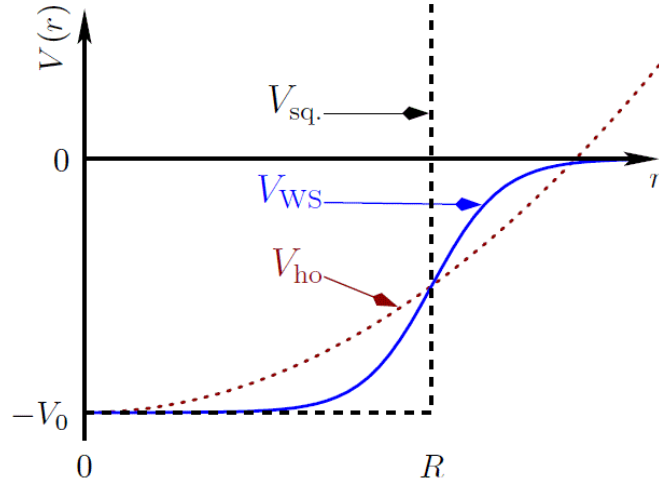
Figure 2.5: *Woods-Saxon, Harmonic Oscillator* and *Squared* potentials in comparison. Ref.[41].

Ignoring the spin, the single-nucleon wavefunctions $\phi(\vec{r})$ can be decomposed into a product of a radial wavefunctions $R_{nl}(r)$ and a spherical harmonics $Y_{lm_l}(\theta, \varphi)$, containing angular information, as

$$h_0\phi(\vec{r}) \equiv \phi_{nlm_l}(\vec{r}) = \frac{R_{nl}(r)}{r}Y_{lm_l}(\theta, \phi) \tag{2.9}$$

where n is the number of nodes of the radial wavefunction; l is the orbital angular momentum and m_l its projection onto the $z-$axis. Being normalized wavefunctions of $\vec{l^2}$ and l_z, one has

$$\begin{cases} \hat{l}^2\phi = \hbar^2 l(l+1)\phi \\ \hat{l}_z\phi = \hbar m_l\phi \end{cases} \tag{2.10}$$

In this way, radial wavefunctions are solutions of the Schrödinger equation:

$$\left(-\frac{\hbar^2}{2M_N}\frac{d^2}{dr^2} + \frac{\hbar^2}{2M_N r^2}l(l+1) + \frac{1}{2}M_N\omega^2 r^2\right)R_{nl}(r) = \epsilon R_{nl}(r) \tag{2.11}$$

with $n \in \mathbb{N}$ the radial quantum number of nodes as just said before, so:

$$R_{nl}(r) = \mathcal{N}_{nl}r^{l+1}\exp\left(-\frac{r^2}{2\mu^2}\right)L_n^{l+1/2}\left(\frac{r}{\mu}\right) \tag{2.12}$$

where $\mathcal{N}_{nl}$ is the normalisation factor coming from the normalisation condition $\int_0^\infty R_{nl}^2(r)\,dr = 1$ and $\mu = \sqrt{\frac{\hbar}{M_N\omega}}$ is the harmonic oscillator length while $L_n^{l+1/2}(\frac{r}{\mu})$ are the generalized Laguerre polynomials. Applying parity operator P on the space spanned by a single-nucleon coordinates (r, θ, ϕ) one obtains:

$$(r, \theta, \varphi) \xrightarrow{P} (r, \pi - \theta, \pi + \varphi), \tag{2.13}$$

$$P\phi_{nlm_l}(\vec{r}) = P\left(\frac{R_{nl}(r)}{r}Y_{lm_l}(\theta, \varphi)\right) = (-1)^l\phi_{nlm_l}(\vec{r}). \tag{2.14}$$

10

So the parity of single-nucleon wavefunction is positive (or negative) if l is even (or odd), and the eigen-energies corresponding to Eq.(2.11) are:

$$\epsilon = \hbar\omega\left(2n + l + \frac{3}{2}\right) = \hbar\omega\left(N + \frac{3}{2}\right) \tag{2.15}$$

whereas: $N \in \mathbb{N}$, $l = N, N - 2, ..., 0$, $n = \frac{N-l}{2}$. Therefore, energy levels can be described by a single quantum number, the principal quantum number N. Since $N = 2n + l$, if N is odd so it is also l, and the conventional notation in nuclear physics is $l = 0, 1, 2, 3, ... = s, p, d, f, ...$. This leads to a degeneracy of energy levels, given by the fermionic nature of nucleons and the isotropy of the harmonic oscillator. The total degeneracy of the Nth oscillator shell for identical nucleons is

$$\sum_{l=0 \text{ or } 1}^{N} 2(2l + 1) = (N + 1)(N + 2) \tag{2.16}$$

Unfortunately, the harmonic oscillator potential in Eq.(2.7) is insufficient to properly describe the number of nucleons corresponding to magic numbers. So Mayer and Jensen introduced a spin-orbit coupling term

$$U_{ls}(r) = f(r)(\vec{l} \cdot \vec{s}) \tag{2.17}$$

to Eq.(2.7), whereas $\vec{l}$, $\vec{s}$ are respectively the quantum angular momentum operator and the spin operator of a nucleon, while the radial function $f(r)$ can be evaluated as

$$f(r) = -V_{ls}\frac{\partial}{\partial r}V(r) \tag{2.18}$$

in which V_{ls} is a constant term and $V(r)$ is the mean field potential. In this way the spin-orbit term is peaked around the nuclear surface, because there is the greatest density change there. Given the full potential

$$U(r) = U_{HO}(r) + U_{ls}(r) = \frac{1}{2}M_N\omega^2 r^2 + f(r)(\vec{l} \cdot \vec{s}) \tag{2.19}$$

the Hamiltonian in spherical coordinates becomes

$$h_0 = -\frac{\hbar^2}{2M_N}\frac{d^2}{dr^2} + \frac{\hbar^2}{2M_N r^2}l(l + 1) + \frac{1}{2}M_N\omega^2 r^2 + f(r)(\vec{l} \cdot \vec{s}) \tag{2.20}$$

Adding the spin-orbit interaction the conserved quantum number now becomes the total angular momentum $\vec{j} = \vec{l} + \vec{s}$. So, the total single-nucleon wavefunctions are

$$\begin{aligned}
\phi_{nlsjm}(r) &= \frac{R_{nl}(r)}{r}\left[Y_l(\theta, \varphi) \otimes \chi_s\right]_m^j \\
&= \frac{R_{nl}(r)}{r}\sum_{m_l m_s}\langle lm_l, sm_s|\, jm\rangle Y_{lm_l}(\theta, \varphi)\chi_{sm_s}
\end{aligned} \tag{2.21}$$

in which, as usual, R_{nl} is the radial part, Y are the spherical harmonics while χ is the spinorial part, s is the intrinsic nucleon spin, $m_l = l_z$, $m_s = s_z$, $m = j_z$ are the projections on the z-axis, $\langle lm_l, sm_s|\, jm\rangle$ are the Clebsch-Gordan coefficients.

Only one nucleon can be in a specific configuration, as required by the Pauli principle: being a state labelled by (n, l, j, m_j), it is possible to distinguish orbits using the z-projection of j, generating $2j + 1$ magnetic degenerate substates. In absence of $\vec{l} \cdot \vec{s}$ interaction, states with $j = l \pm \frac{1}{2}$ are degenerate. By applying spin-orbit on a generic state $|\Phi\rangle$:

$$2\vec{l} \cdot \vec{s}|\Phi\rangle = \hbar^2[j(j + 1) - s(s + 1) - l(l + 1)]|\Phi\rangle \tag{2.22}$$

Now there can be: $j = l \pm \frac{1}{2}$

$$\begin{cases} j = l + 1/2 \Rightarrow 2\vec{l} \cdot \vec{s} |\Phi\rangle = l\hbar^2 |\Phi\rangle \\ j = l - 1/2 \Rightarrow 2\vec{l} \cdot \vec{s} |\Phi\rangle = -(l+1)\hbar^2 |\Phi\rangle \end{cases} \tag{2.23}$$

and the negative sign Eqs. (2.17, 2.18) gives the lower energy state for the state with $j = l + \frac{1}{2}$ with respect to that with $j = l - \frac{1}{2}$, splitting the energy degeneracies.

Again, one can also add a term proportional to $\vec{l} \cdot \vec{l}$: $U_{ll}(r) = g(r)(\vec{l} \cdot \vec{l})$, so that:

$$U(r) = U_{HO}(r) + U_{ls}(r) + U_{ll}(r) = \frac{1}{2} M_N \omega^2 r^2 + f(r)(\vec{l} \cdot \vec{s}) + g(r)(\vec{l} \cdot \vec{l}) \tag{2.24}$$

This last term acts on orbits by correcting the spacing between them:

$$\vec{l} \cdot \vec{l} |\Phi\rangle = \hbar^2 l(l+1) |\Phi\rangle \tag{2.25}$$

according with the angular momentum l.

In the right side of Fig.2.6, it is possible to appreciate the single-nucleon level structure, in particular how closed lying orbits (the shells), are separated by larger energy gaps. The existence of magic numbers emerges from the structure of shells and shell gaps. So, a proton (neutron) closed shell is formed if all orbits in a given shell are saturated by protons (neutrons). The number of protons (or neutrons) in each closed shell is determined by summing the occupation numbers of the individual orbitals that make up the shell.

Recalling the nuclear chart in Fig.1.3 it is possible to distinguish between closed-shell nuclei, such as $^{16}_{8}O_8$ or $^{40}_{20}Ca_{20}$, in which each shell is closed and open-shell nuclei, such as $^{17}_{8}O_9$, in which shells are partially occupied. The latter ones are also known as valence shells.
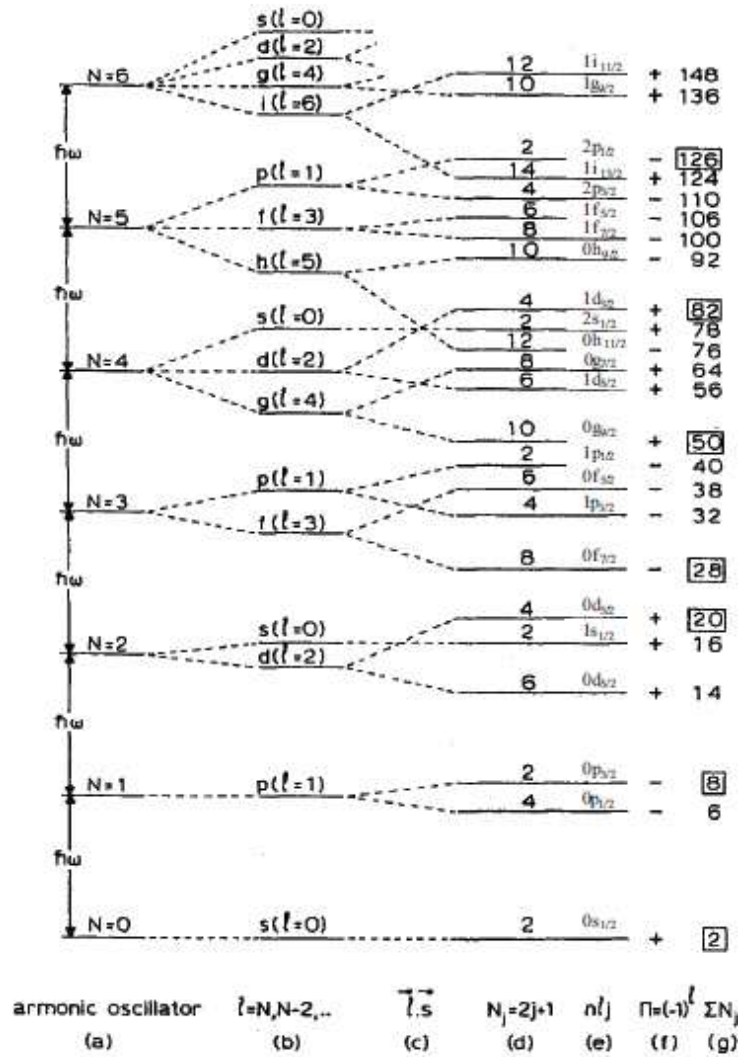
Figure 2.6: Sequence of single-nucleon states: **a**) HO potential; **b**) WS potential; **c**) ls splitting; **d**) number N of degenerate nucleons in each shell; **e** spectroscopic (n, l, j) notation of the single-nucleon; **f** shell parity $(-1)^l$; **g**) matching of the magic number in correspondence of shell closure. Refs.[13, 28].

However, nucleons can be excited to higher energy levels, typically into the next shell that is not fully occupied, leaving behind vacancies in the closed shell. These processes are known as particle-hole excitations, where the excited nucleon is the particle, and the vacated state is referred to as a hole.

2.2.2   The Interacting Shell Model

In the shell model description of heavy nuclei, it is a conventional approach to assume an inert closed-shell core, with only the degrees of freedom of the valence nucleons in the remaining shells treated explicitly. If all shells are taken into account, the approach is called *no-core* Shell model, but with growing masses, A, and therefore with growing degeneracy of the associated shell model orbitals, it quickly becomes computationally difficult to handle[1].

---

[1]At present only nuclei with mass $A \approx 20$ can be treated with this approach.

For many-nucleons systems, shell model calculations are typically limited to the valence shell above a presumably inert closed-shell core. Orbitals above this valence space (the so-called *excluded space*) are typically neglected. However, in some cases, such as calculations involving two main shells, cross-shell particle-hole excitations may be included.

In this thesis, we focused on the *sd*-shell consisting in the $0d_{\frac{5}{2}}$, $1s_{\frac{1}{2}}$ and $0d_{\frac{3}{2}}$ as valence orbitals, but during the analysis also the possibility of promoting nucleons from the lower *p*-shell and from *sd* to *fp* shell is considered to study negative-parity states. Being the nucleus a system of interacting fermions, the Hamiltonian should consist of nucleons kinetic energies and nucleon-nucleon interactions:

$$H = \sum_{i=1}^{A} K_i + \frac{1}{2} \sum_{i,j=1}^{A} V_{ij} \tag{2.26}$$

whereas the $\frac{1}{2}$ factor is to avoid double counting in the two-body interaction. Higher body terms are neglected in this stage. Then, introducing a single-particle potential $U(r)$, the Hamiltonian can be rewritten as

$$H = \sum_{i=1}^{A} [K_i + U(r_i)] + \frac{1}{2} \sum_{i,j=1}^{A} V_{ij} - \sum_{i=1}^{A} U(r_i) \tag{2.27}$$

so that the Schrödinger equation will be

$$H|\Phi\rangle = \left(\sum_i (K_i + U_i) + \sum_{i<j} V_{ij} - \sum_i U_i \right) |\Phi\rangle = E|\Phi\rangle \tag{2.28}$$

where $|\Phi\rangle$ encodes the many-body state and the auxiliary single-body potential U_i is added and subtracted to compare the perturbed Hamiltonian $H_{pert.} = \sum_{i<j} V_{ij} - \sum_i U_i$ with the unperturbed one $H_0 = \sum_i = (K_i + U_i)$. U_i is chosen so that $H_0 \ll H_1$ and the perturbative approach is allowed.

As just said before, facing the full problem is difficult; for this reason, one has to restrict the full Hilbert $\mathcal{H}$ space to a portion of it, the previous mentioned model space $\mathcal{M} \subset \mathcal{H}$, so that $\mathcal{H} = \mathcal{M} \cup (\mathcal{H} \setminus \mathcal{M})$[2]. In this subspace, one can take the state $|\Phi'\rangle$, and then consider the following Schrödinger equation:

$$\hat{H}_{\text{eff}}|\Phi'\rangle = E|\Phi'\rangle \tag{2.29}$$

in which $\hat{H}_{\text{eff}}$ is the effective Hamiltonian. The model space $\mathcal{M}$ is defined by an inert nucleus and a valence space. The inert nucleus, which represents the interacting vacuum of theory, consists of fully occupied orbitals, whose nucleons are considered "frozen" and unable to make transitions to other orbitals.

In contrast, nucleons outside the core are free to occupy various configurations within the valence space. Orbitals outside the valence space, called outer space, are excluded from occupation. The valence space should be chosen so as to strike a balance: it must be simple enough to allow tractable calculations, but rich enough to capture all relevant degrees of freedom. In $\mathcal{M}$, the Hamiltonian can be rewritten as

$$\hat{H}_{eff} = H_0 + H_{\text{residual}} = \sum_{i=1}^{A} h_0(i) + H_{\text{residual}} \tag{2.30}$$

---

[2]States belonging to $\mathcal{M}$ can be obtained by applying the projector $\hat{P}$: $|\Phi'\rangle = \hat{P}|\Phi\rangle$. Idem for states $|\Gamma\rangle \in (\mathcal{H} \setminus \mathcal{M})$, but with the projector $\hat{Q}$: $|\Gamma\rangle = \hat{Q}|\Phi\rangle$.

and $H_{residual}$ denotes the residual Hamiltonian. So the energy of the system, following the Eq.(2.29) can be divided in two contributions:

$$(H_0 + H_{residual})|\Phi\rangle = (E_0 + E_{residual})|\Phi\rangle \tag{2.31}$$

Then, following the same philosophy explained in the Eqs. (2.1-2.4), one builds a basis of eigenstates of single-nucleon Hamiltonians $|\phi_i\rangle$, each of which has an eigenenergy ϵ_i:

$$h_0(i)|\phi_i\rangle = \epsilon_i|\phi_i\rangle \tag{2.32}$$

So that the many-nucleons antisymmetric wavefunction can be constructed as the Slater determinant of the ϕ_i:

$$\psi_n^0 = \frac{1}{\sqrt{A!}} \det \begin{pmatrix} \phi_1(\vec{r_1}) & \cdots & \phi_1(\vec{r_A}) \\ \vdots & \ddots & \vdots \\ \phi_A(\vec{r_1}) & \cdots & \phi_A(\vec{r_A}) \end{pmatrix} \tag{2.33}$$

where n stands for the particular configuration of the many-nucleons state of the system and obeys the equation

$$H_0 |\psi_n^0\rangle = E_n^0 |\psi_n^0\rangle = \sum_{i=1}^{A} \epsilon_i |\psi_n^0\rangle. \tag{2.34}$$

The different configurations describe how the valence nucleons (the protons and neutrons outside the inert core) are distributed among the available orbitals in the model space. These configurations may also include particle-hole excitations. To represent them, the common notation is:

$$|\pi(\alpha_1^{m_1} \cdots \alpha_r^{m_r}) \otimes \nu(\beta_1^{n_1} \cdots \beta_s^{n_s})\rangle \tag{2.35}$$

where π = protons, ν = neutrons, α and β are the occupied valence orbits, while m and n specify the number of protons and neutrons. The number of configurations increases dramatically with the dimension of the valence space, for this reason one can build the true many-nucleons wavefunction summing over all the possible n configurations

$$|\Psi_p\rangle = \sum_n a_{pn} |\psi_n^0\rangle \text{ such that } \sum_n a_{pn}^2 = 1 \tag{2.36}$$

therefore the probability to be in the n configuration is given by $P_n = a_{pn}^2$. In this way, the Schrödinger equation can be rewritten as:

$$H|\Psi_p\rangle = E_p|\Psi_p\rangle = E_p \sum_{n=1}^{k} a_{pn}|\psi_n^0\rangle \iff \sum_{n=1}^{k} a_{pn}\langle\psi_l^0|H|\psi_n^0\rangle = E_p a_{lp} \tag{2.37}$$

in which both sides are multiplied by $\langle\psi_l^0|$ and the orthonormality condition $\langle\psi_l^0|\psi_k^0\rangle = \delta_{lk}$ holds. The Hamiltonian matrix element $H_{ln} = \langle\psi_l^0|H|\psi_n^0\rangle = \langle\psi_l^0|(H_0 + H_{residual})|\psi_n^0\rangle$ can be divided into a diagonal and an off-diagonal part, involving, respectively, the unperturbed part and the residual one: $H_{ln} = E_n^0 \delta_{ln} + \langle\psi_l^0|H_{residual}|\psi_n^0\rangle$. While the E_p value of the Eq.(2.37) using $\sum_n H_{ln}a_{np} = E_p a_{lp}$. In this way, the eigenvalue equation becomes a matrix equation $[H][A] = [E][A]$ that forms a secular equation for the E_p eigenvalues:

$$\begin{vmatrix} H_{11} - E_p & H_{12} & \dots H_{1n} \\ H_{21} & H_{22} - E_p & \dots H_{2n} \\ \vdots & \vdots & \vdots \\ H_{n1} & \dots & H_{nn} - E_p \end{vmatrix} = 0 \tag{2.38}$$

Having the energies E_p, it is possible to use

$$\sum_{n=1}^{k} E_n^0 \delta_{ln} a_{np} + \sum_{n=1}^{k} \langle \psi_l^0 | H_{residual} | \psi_n^0 \rangle a_{np} = E_p a_{lp} \tag{2.39}$$

to extract the coefficients a_{np}. Eventually, by using the orthonormalisation $\sum_n^k a_{np} a_{np'} = \delta_{pp'}$ in the previous equation, one gets

$$\sum_{l,n=1}^{k} a_{lp'} E_n^0 \delta_{ln} a_{np} + \sum_{l,n=1}^{k} a_{lp'} \langle \psi_l^0 | H_{residual} | \psi_n^0 \rangle a_{pn} = E_p \delta_{pp'} \tag{2.40}$$

that is again a matrix equation of the type $[A]^{-1}[H][A] = [E]$, indicating a transformation to a new basis that makes $[H]$ diagonal. Facing this problem in nuclear physics is usually computationally hard, because k rapidly increases the basis dimension. For this reason, it is fundamental to adopt the appropriate methods and calculation strategies.

2.2.3 Second Quantisation formalism

The aim of this subsection is to introduce the second quantisation formalism in order to rewrite what has been done till now, using occupation number formalism.
As usual, one has to define the fermionic operators $a_{\alpha_i}^\dagger$ and a_{α_i} which, respectively, create and annihilate a single-nucleon state $|\alpha\rangle = |n, l, m, j, \tau\rangle$:

$$\begin{aligned} |\alpha\rangle &= a_\alpha^\dagger |0\rangle, \\ |0\rangle &= a_\alpha |\vartheta\rangle. \end{aligned} \tag{2.41}$$

Closed shells are taken as vacuum states $|0\rangle$. These are Hermitian operators following the relations: $(a_\alpha)^\dagger = a_\alpha^\dagger$, $(a_\alpha) = (a_\alpha^\dagger)^\dagger$, and obeying to the anti-commutations rules:

$$\begin{cases} \{a_\alpha^\dagger, a_\theta\} = a_\alpha^\dagger a_\theta + a_\alpha a_\theta^\dagger = \delta_{\alpha\theta}, \\ \{a_\alpha^\dagger, a_\theta^\dagger\} = \{a_\alpha, a_\theta\} = 0. \end{cases} \tag{2.42}$$

The coordinate representation of the single-nucleon state α is $\langle \vec{r} | \alpha \rangle \equiv \phi_\alpha(\vec{r})$. Therefore, an antisymmetric $A-$ nucleon state is

$$|\alpha_1, \alpha_2, \ldots, \alpha_A\rangle = a_{\alpha_A}^\dagger a_{\alpha_{A-1}}^\dagger a_{\alpha_{A-2}}^\dagger \ldots a_{\alpha_2}^\dagger a_{\alpha_1}^\dagger |0\rangle. \tag{2.43}$$

H_0 and $H_{residual}$ in Eq.(2.31) are given respectively by a symmetric one-nucleon operator $\hat{O}$ and a two-nucleon operator $\hat{T}$:

$$\hat{O} = \sum_{i=1}^{A} \hat{O}(\vec{r}_i); \qquad \hat{T} = \sum_{i<j}^{A} \hat{T}(\vec{r}_i, \vec{r}_j) \tag{2.44}$$

$\hat{O}$ can be described by matrix elements between one-nucleon states:

$$\langle \alpha | \hat{O} | \beta \rangle = \int \phi_\alpha^*(\vec{r}) \hat{O}(\vec{r}_i) \phi_\beta(\vec{r}) d\vec{r} \tag{2.45}$$

while $\hat{T}$ is given by matrix elements between normalised and antisymmetric two-nucleon states:

$$\langle \alpha, \beta | \hat{T} | \gamma, \delta \rangle = \int \phi_\alpha^*(\vec{r}_1) \phi_\beta^*(\vec{r}_2) \hat{T}(\vec{r}_1, \vec{r}_2) \left(1 - \hat{P}_{12}\right) \phi_\gamma(\vec{r}_1) \phi_\delta(\vec{r}_2) d\vec{r}_1 d\vec{r}_2 \tag{2.46}$$

whereas $\hat{P}_{12}$ is an exchange operator. So, the one-nucleon and two-nucleon operators are written in a second-quantised formalism as

$$\hat{O} = \sum_{\alpha,\beta}\langle\alpha|\hat{O}|\beta\rangle a_\alpha^\dagger a_\beta, \quad and \quad \hat{T} = \tfrac{1}{4}\sum_{\alpha,\beta,\gamma,\delta}\langle\alpha,\beta|\hat{T}|\gamma,\delta\rangle a_\alpha^\dagger a_\beta^\dagger a_\gamma a_\delta, \tag{2.47}$$

where the $\frac{1}{4}$ factor to avoid a four-fold counting. Finally, the shell-model Hamiltonian can be written, in the second-quantisation formalism, as:

$$\hat{H} = \sum_{\alpha,\beta}\langle\alpha|\hat{O}|\beta\rangle a_\alpha^\dagger a_\beta + \frac{1}{4}\sum_{\alpha,\beta,\gamma,\delta}\langle\alpha,\beta|\hat{V}|\gamma\delta\rangle a_\alpha^\dagger a_\beta^\dagger a_\gamma a_\delta. \tag{2.48}$$

2.3 The Eigenvalue Problem

There are several numerical algorithms available for matrix diagonalisation. For example, Jacobi's method is suitable for small matrices (size $d \le 50$), Householder's method is typically used for medium-sized matrices ($50 \le d \le 200$), and Lanczos' method is preferred for large-scale problems ($d \ge 200$) and extremely large matrices. In this work, the Lanczos method [29] has been used because, as can be seen later, the matrix size will be large. After that, one has to calculate Eq.(2.40) using some code. In this thesis, the ANTOINE code by Caurier, Nowacki [14, 15] was used.

2.3.1 The Lanczos Method

The Lanczos algorithm, introduced in Ref. [29], is used to diagonalise the Hamiltonian matrix and thus obtain the energy eigenvalues of the nuclear states. Starting from a chosen pivot state, the method iteratively constructs an approximate eigenvector, allowing to identify specific states with a defined total angular momentum J and parity P, denoted by $|J^P\rangle$. This approach returns the energy of the lowest state with the specified quantum numbers.

The algorithm is particularly suitable for Shell Model calculations, where typically only a limited number of low-level eigenstates with specific total angular momentum and isospins are required. Furthermore, the Lanczos method is highly efficient in this context because the Hamiltonian matrices involved are sparse; the number of non-zero elements scales linearly with the matrix size, rather than quadratically [14]. Using this method, the Hamiltonian matrix is written in such a basis that it becomes tridiagonal. One has to take a random pivot $|1\rangle$, such that $|a_1\rangle = H|1\rangle$ is calculated and posed to be equal to:

$$|a_1\rangle = H_{11}|1\rangle + |2'\rangle \quad \text{with } \langle 1 \mid 2'\rangle = 0 \Longrightarrow H_{11} = \langle 1 \mid a_1\rangle = \langle 1|H|1\rangle \tag{2.49}$$

So, the other two matrix elements can be calculated:

$$|2\rangle = \frac{|2'\rangle}{\sqrt{\langle 2' \mid 2'\rangle}} \Longrightarrow H_{12} = \langle 1|H|2\rangle, \quad H_{22} = \langle 1|H|2\rangle \tag{2.50}$$

Iterating this algorithm n-times, the $|a_n\rangle$ vector can be defined:

$$|a_n\rangle = H|n\rangle = H_{n,n-1}|n-1\rangle + H_{n,n}|n\rangle + |n+1'\rangle, \tag{2.51}$$

Therefore, the Hamiltonian matrix has the form:

$$\begin{bmatrix} H_{11} & H_{12} & 0 & 0 & \cdots & 0 \\ H_{21} & H_{22} & H_{23} & 0 & \cdots & 0 \\ 0 & H_{32} & H_{33} & H_{34} & \cdots & 0 \\ \vdots & \vdots & \vdots & \vdots & \ddots & \vdots \\ 0 & 0 & 0 & 0 & H_{n,n-1} & H_{n,n} \end{bmatrix} \tag{2.52}$$

Importantly, the number of iterations required by the Lanczos method depends only weakly on the matrix size and instead scales approximately linearly with the number of non-zero elements in the matrix.

Convergence also depends on the number of eigenstates computed and the choice of the initial pivot state. These features make the Lanczos algorithm an ideal tool for efficient diagonalisation in the context of shell model studies.

To solve the problem, another step must be taken: the choice of the basis, which, in fact, is only a matter of convention. Basically, there are two main options: the $JT-$scheme and the $m-$scheme. The ANOTOINE code uses $m-$scheme, so here this scheme is described. In the $m-$scheme, the basis is given by Slater determinants built from single-nucleon states $|n, l, m, j, \tau\rangle$, characterised by the harmonic oscillator quantum numbers n, l, j, the magnetic quantum number m and the isospin τ. The Slater determinants are given by:

$$\Phi_{a_1,\ldots,a_A}(1,\ldots,A) = \frac{1}{\sqrt{A!}} \det \begin{pmatrix} \phi_{a_1}(1) & \cdots & \phi_{a_A}(1) \\ \vdots & \ddots & \vdots \\ \phi_{a_1}(A) & \cdots & \phi_{a_A}(A) \end{pmatrix} = a_{a_1}^\dagger \cdots a_{a_A}^\dagger |0\rangle \qquad (2.53)$$

In this scheme the basis of the many-body matrix elements H reduces to the two-particle matrix elements H with a phase and this is why $m-$scheme is good. In contrast, only j_z and τ_z are good quantum numbers. This means that the dimension of the Slater determinants will depend on the total degeneracy of neutrons and protons in their valence spaces $\Omega_n = \sum_{j_n}(2j_n + 1)$ and $\Omega_p = \sum_{j_p}(2j_p + 1)$. In particular, the dimension of the configuration space is proportional to the product of the binomial coefficients:

$$\binom{\Omega_p}{N_p}\binom{\Omega_n}{N_n}. \qquad (2.54)$$

whereas N_p and N_n are the numbers of active protons and neutrons in the model space. In this work, $_8^{16}O_8$ is treated as the inert core and $0d_{5/2}$, $1s_{1/2}$ and $0d_{3/2}$ as valence shells. Therefore, as an example, the dimension of the configuration space for $_{12}^{23}Mg_{11}$ is $\binom{12}{4}\binom{12}{3} = 108900$.

2.3.2 The ANTOINE Shell Model Code

Based on the ideas of the Glasgow group [50] the ANTOINE Shell Model Code, originally developed by E.Caurier and F.Nowacki [15], is a logical implementation of the Lanczos method in the $m-$scheme, representing the Slater determinant basis as a word of integers, where every bit of the word corresponds to a single-nucleon state $|n, l, m, j, \tau, \tau_z\rangle$[3]. Therefore, each bit has a value indicating if it is empty or occupied, labelled, respectively, by the values 0 and 1.

A two-body operator of the type $a_\alpha^\dagger a_\beta^\dagger a_\gamma a_\delta$ search the word with bits $\alpha, \beta, \gamma, \delta$ in the 0011 configuration and changes it to 1100 [4].

In the basis of the $m-$scheme, the full many-body state $|I\rangle$ is written as $|i, \alpha\rangle$, which separates the proton (i) and neutron (α) Slater determinants. Each state is characterised by a total $M = M_1 + M_2$, where M_1 and M_2 are the projections of the angular momentum for protons and neutrons, respectively. Given a fixed M, only combinations of M_1 and M_2 summing to M are

---

[3]τ and τ_z represent isospin number and its z-axis projection. These are deeply treated in the first part of Chapter 3.

[4]This, in fact, mimics the action of ladder operators in the second quantisation formalism: $a^\dagger$ "creates" an occupied bit, by flipping a 0 to a 1, the contrary for a that destroys an occupied bit to an empty one: from a 1 value bit to a 0.

allowed. For a proton state $|i\rangle$ with fixed M_1, the maximum neutron states M_2 and associated α can be determined.

A mapping array $R(i)$ is built so that full states are labelled $I = R(i) + \alpha$, with an analogous mapping for $|j, \beta\rangle$ states. The elements of the proton-proton ($\langle i|H|j\rangle$) and neutron-neutron ($\langle \alpha|H|\beta\rangle$) matrix are precomputed, so Lanczos iterations need only loop over α and i to access all non-zero elements. $\langle I|H|J\rangle$.

The elements of the proton-neutron matrix require more care. If $|I\rangle = |i, \alpha\rangle$, $|J\rangle = |j, \beta\rangle$, and the states differ by a one-body proton operator $a_q^\dagger a_r$ with $\Delta m = m' - m$, then the neutron Slater states must differ by $-\Delta m$ by using a one-body operator at position μ. To simplify this, an index array Q is defined so that $K = Q(s) + \mu$ labels the relevant matrix element $V(K)$. With precomputed $I = R(i) + \alpha$, $J = R(j) + \beta$, and $V(K)$, nonzero values $\langle I|H|J\rangle$ can be efficiently accessed and stored.
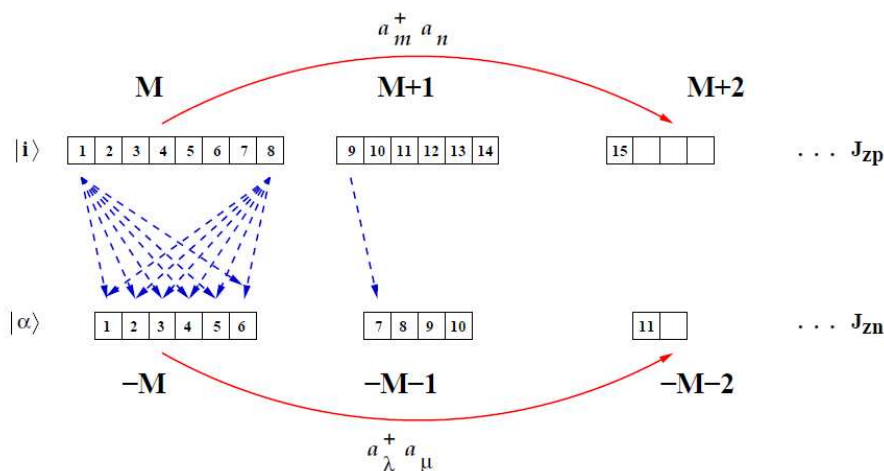
Figure 2.7: Schematic representation of the shell-model basis of the $m-$scheme. The shell-model basis is constructed as a product of two Slater determinants, one for protons $|i\rangle$ and one for neutrons $|\alpha\rangle$. Proton determinants are represented in the upper row and neutron determinants in the lower row, grouped into blocks with the same value of J_z. States with total $J_z = 0$ are formed by pairing proton and neutron determinants that have the same absolute value of M but opposite signs. A generic two-body proton–neutron operator, $a_m^\dagger a_n a_\lambda^\dagger a_\mu$, conserves the total M, so any increase of the proton M must be matched by a corresponding decrease in the neutron M, and vice versa. Refs.[14, 28]

.

A standard ANTOINE code input usually requires: a valence space made by the orbits occupable by the valence nucleons; the number of valence nucleons, specifying protons and neutrons; a suitable effective interaction; a set of initial states characterised by their parity and total angular momentum J^P.

2.3.3 Effective Interactions

A key step to make robust predictions and calculations is the choice of the effective interaction to implement in the ANTOINE code. In this thesis, two main interactions have been used: the USDA interaction[5] [12] to study positive-parity states in the sd-shell and the PSDPF interaction to investigate negative-parity intruder states.

The USDA has been used to make calculations for nuclei with an inert core corresponding to

---

[5]Proposed by Brown and Richter as an "evolution" of the Brown-Wildenthal USD interaction proposed in [11].

that of $^{16}_{8}O_8$, corresponding to the s and p shells and sd-shell as valence space. The PSDPF uses a core corresponding to $^{4}_{2}He_2$ and the $p - sd - fp$ orbits as model space. Following [12], the interaction is built starting from the effective Hamiltonian[6]:

$$H_{\text{eff}} = \sum_a \epsilon_a \hat{n}_a + \sum_{a \leq b, c \leq d} \sum_{JT} V_{JT}(ab; cd) \hat{T}_{JT}(ab; cd) \tag{2.55}$$

$$\hat{T}_{JT}(ab; cd) = \sum_{MT_z} \hat{A}^{\dagger}_{JMTT_z}(ab) \hat{A}_{JMTT_z}(cd) \tag{2.56}$$

This operator defines the two-body scalar density for a pair of nucleons.

To simplify notation, the effective Hamiltonian is expressed as a linear combination:

$$H_{\text{eff}} = \sum_i x_i \hat{O}_i$$

where each coefficient x_i may correspond to parameters such as ϵ_a or two-body matrix elements V_{JT}, and $\hat{O}_i$ represents either one-body or two-body operators ($\hat{n}$ and $\hat{T}$).

The Hamiltonian is thus completely determined by the parameter vector $\vec{x}$, and has eigenstates $|\phi_k\rangle$ with associated eigenvalues λ_k:

$$\lambda_k = \langle \phi_k | H_{\text{eff}} | \phi_k \rangle = \sum_i x_i \langle \phi_k | \hat{O}_i | \phi_k \rangle = \sum_i x_i \beta_i^k$$

where we define $\beta_i^k = \langle \phi_k | \hat{O}_i | \phi_k \rangle$.

To fit the Hamiltonian to the experimental data, the values of x_i are adjusted by minimising the chi-squared function:

$$\chi^2 = \sum_k \left(\frac{E_{\text{exp}}^k - \lambda_k}{\sigma_{\text{exp}}^k} \right)^2$$

Here, E_{exp}^k and σ_{exp}^k represent the experimental energy levels and their uncertainties, respectively. The dataset referenced in Ref. [21] includes 608 states across 77 nuclei in the sd-shell. The strength of this interaction lies in its proven ability to accurately reproduce experimental data, as demonstrated by numerous theoretical calculations reported in [12, 14].

---

[6]Using the second quantisation formalism introduced in Sec.2.1.3.

Chapter 3

Mirror Nuclei and Mirror Energy Differences

3.1 Isospin Formalism

Isospin symmetry, although approximate, plays a fundamental role in nuclear physics by exploiting the near equivalence of protons and neutrons, treating them as two charge states of a single particle: the nucleon. This is justified by their nearly identical masses: $m_p = 938.27$ MeV$/c^2$ and $m_n = 939.57$ MeV$/c^2$ and the approximate charge independence of nuclear forces, meaning that the interactions pp, nn and pn are similar, as already seen in Chapter 1.

This symmetry has long guided the formulation of nucleon-nucleon interactions and is incorporated into nuclear models like the shell model, where it simplifies calculations and allows nuclear states to be classified by isospin quantum numbers, an approach that also extends to baryons and mesons in particle physics. However, isospin symmetry is not exact. It is broken by electromagnetic interactions, small differences in the strong force, and the mass difference between protons and neutrons.

Although such effects are minor on the nuclear scale, they are crucial for understanding isospin-forbidden processes. To describe nucleons as a doublet, Heisenberg introduced isospin in analogy to what Pauli did with spin. The isospin space, or isospace, is an abstract space spanned by the vectors representing proton and neutron:

$$|p\rangle = \begin{pmatrix} 0 \\ 1 \end{pmatrix}, \quad |n\rangle = \begin{pmatrix} 1 \\ 0 \end{pmatrix}. \tag{3.1}$$

The isospin operator is a vector $\vec{\tau}$ defined by its components, defined as the projections along x, y, z axis in the isospace:

$$\tau_x = \frac{1}{2}\begin{pmatrix} 0 & 1 \\ 1 & 0 \end{pmatrix}, \quad \tau_y = \frac{1}{2}\begin{pmatrix} 0 & -i \\ i & 0 \end{pmatrix}, \quad \tau_z = \frac{1}{2}\begin{pmatrix} 1 & 0 \\ 0 & -1 \end{pmatrix} \tag{3.2}$$

These components obeys to the $SU(2)$ commutation relations $[\tau_x, \tau_y] = i\tau_z$, with the cyclicity property. Casimir operator[1] $\vec{\tau}^2$ commutes with the $SU(2)$ generators $[\vec{\tau}^2, \tau_i] = 0$, for $i = x, y, z$. The eigenvalues of the Casimir operator is $\tau(\tau + 1)$. Now, if τ_z acts on a proton or on a neutron

---

[1]It is an operator that commutes with all the elements of a Lie algebra. The commutators shows that isospin operators t_i, $i = x, y, z$ form a Lie algebra $\mathfrak{T}$ and $\vec{\tau}^2$ commutes with all the elements $\tau_i \in \mathfrak{T}$.

state, recalling the definition in Eq. (3.1):

$$\tau_z|p\rangle = \frac{1}{2}\begin{pmatrix} 1 & 0 \\ 0 & -1 \end{pmatrix}\begin{pmatrix} 1 \\ 0 \end{pmatrix} = -\frac{1}{2}|p\rangle, \quad \tau_z|n\rangle = \frac{1}{2}\begin{pmatrix} 1 & 0 \\ 0 & -1 \end{pmatrix}\begin{pmatrix} 1 \\ 0 \end{pmatrix} = \frac{1}{2}|n\rangle. \tag{3.3}$$

By using the τ_i operators, one can introduce other two ladder operators:

$$\tau_+ \equiv \tau_x + i\tau_y, \quad \tau_- \equiv \tau_x - i\tau_y, \tag{3.4}$$

which obey to the commutation relations in the following way:

$$[\tau_z, \tau_\pm] = \pm\tau_\pm, \quad [\tau_+, \tau_-] = 2\tau_z. \tag{3.5}$$

Applying these operator to a proton or a neutron state one transforms the state itself:

$$\tau_+|p\rangle = |n\rangle, \quad \tau_-|p\rangle = 0, \quad \tau_-|n\rangle = |p\rangle, \quad \tau_+|n\rangle = 0. \tag{3.6}$$

Starting from $\vec{\tau}$ and τ_z, the isospin operator and the related z-axis projection of a many-nucleons system can be defined as

$$\vec{T}_{\text{total}} = \sum_{i=1}^{A}\vec{\tau}_i, \quad T_z = \sum_{i=1}^{A}\tau_{z_i}, \tag{3.7}$$

in which A stands for the number of nucleons $N + Z$ in the nucleus. $\vec{T}$, T_z and $\vec{T}^2$ obeys to similar relations already seen for $\vec{\tau}$, τ_z and $\vec{\tau}^2$: commutation relation hold for $\vec{T}$, the eigenvalues of $\vec{T}^2$ Casimir operator is $T(T+1)$. Total many-nucleons isospin T depends on the number of nucleon A, in particular, if A is odd T is half-odd number while if A even, A is an integer.
As for $\vec{\tau}^2$, there are $(2T+1)$ eigenstates of $\vec{T}^2$ distinguished by their $z-$projection T_z and forming the so-called isospin (or isobaric) multiplet, with $T_z = -T, -T + 1, ..., T - 1, T$. In general, a $T = \frac{1}{2}$, $T = 1$, $T = \frac{3}{2}$, ... isospin multiplet forms, respectively, a doublet, a triplet, a quadruplet, etc... of states. Given a nucleus with N neutrons and Z protons, it will have a

$$T_z = \frac{N - Z}{2}, \tag{3.8}$$

while the total isospin is given by

$$T = |T_z|, |T_z| + 1, \dots, \frac{1}{2}A. \tag{3.9}$$

So, in general, ground states of nuclei have $T = T_z$ except for odd-odd nuclei.
Assuming a two-body nucleon-nucleon interaction and invoking *charge symmetry* ($V_{nn} = V_{pp}$) and *charge independence* (i.e., $V_{pp} = V_{nn} = V_{np}$ in the $T = 1$ channel[2]), a system of A nucleons described by an isospin-invariant Hamiltonian H_0 satisfies

$$[H_0, \vec{T}] = 0, \tag{3.10}$$

meaning that the total isospin $\vec{T}$ is conserved [3]. Thus, H_0 eigenstates can be labelled by their isospin quantum numbers T and T_z.
In these terms, the isospin formalism can be used to classify nuclear states. Introducing other

---

[2]Notice how this is a strong approximation.
[3]It can be noticed that charge operator $\mathcal{Q}$ can be defined in isospin terms as: $\mathcal{Q} = q\frac{1-2\tau_z}{2}$, hence if $[H_0, T_z] = 0 \implies [H_0, \mathcal{Q}] = 0$ and electric charge is conserved.

relevant quantum numbers $(\pi, J, A, ...)$ as α, then the previous Hamiltonian eigenstates can be represented as $|\alpha, T, T_z\rangle$ and one gets

$$T^2|\alpha, T, T_z\rangle = T(T+1)|\alpha, T, T_z\rangle,$$
$$T_z|\alpha, T, T_z\rangle = T_z|\alpha, T, T_z\rangle. \tag{3.11}$$

As a consequence states in the isobars, having same α and T quantum numbers but differing for their T_z are known as isobaric analogue states (IAS) and are degenerate in energy[4].

Recalling the principles of the spin formalism from which isospin draws inspiration, all member states of an isospin multiplet can be transformed by the total isospin raising and lowering operators

$$T_\pm \equiv T_x \pm iT_y = \sum_{i=1}^{A}[\tau_x(i) \pm i\tau_y(i)], \tag{3.12}$$

obtained by summing over single-nucleon operators defined in Eq.(3.6). Similarly, for Eq. (3.5),

$$[T_z, T_\pm] = \pm T_\pm, \quad [T_+, T_-] = 2T_z. \tag{3.13}$$

Acting with $T_\pm$ on a nuclear state $|\alpha, T, T_z\rangle$, one gets

$$T_\pm|\alpha, T, T_z\rangle = \sqrt{T(T+1) - T_z(T_z \pm 1)}|\alpha, T, T_z \pm 1\rangle. \tag{3.14}$$

As defined earlier, IAS in *mirror nuclei*[5] share the same energy levels scheme. Therefore, studying their excitation energy differences, known as Mirror Energy Differences (MED), provides insight into isospin-symmetry breaking components of the nuclear interaction allowing one to detect subtle structural changes as functions of total angular momentum J and excitation energy.

Differently from IAS, in a mirror pair, the number of *pp* interactions in one nucleus is equal to the number of *nn* interactions in the other of the doublet. Therefore, in a mirror pair charge symmetry is sufficient to provide isospin symmetry.

---

[4]Under the previous hypothesis, all this goes under the name of *isospin symmetry principle*.

[5]Recalling that these are pairs of nuclei with their numbers of protons and neutrons interchanged.
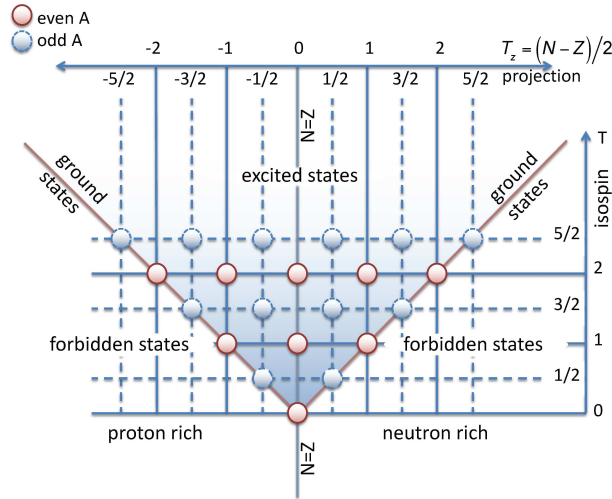
Figure 3.1: A schematic visualisation of the classification of nuclear states according to the total isospin quantum numbers T, T_z. Each circle represents a set of states, of given isospin, which are allowed by the Pauli principle. Note that the diagram assumes that the lowest-energy set of states in any nucleus have the lowest allowed value of isospin. This is usually, but not always, true, e.g., odd-odd $N = Z$ nuclei (equal and odd numbers of neutrons, N, and protons, Z). Picture taken from [4].

3.2   Energy Differences along Isobaric Multiplets

Following [3] here, the *Isobaric Multiplet Mass Equation* (IMME) is introduced by using the isospin formalism.

Isospin non-conserving interactions, primarily the Coulomb force, lift the degeneracy of IAS, typically lowering the binding energy (BE) of higher Z members of the multiplet, due to pp repulsion. The resulting energy difference is called *Coulomb Displacement Energy* (CDE) and for two IAS that differ by the exchange of k protons and neutrons the CDE quantifies this shift

$$CDE(T, T_z) = M_{T,T_z} - = M_{T,T_z+k} + k\Delta_{nH} \qquad (3.15)$$

whereas M is the atomic mass, Δ_{nH} is the neutron-Hydrogen atomic mass difference and T_z the isospin z-projection of the larger Z isobar.
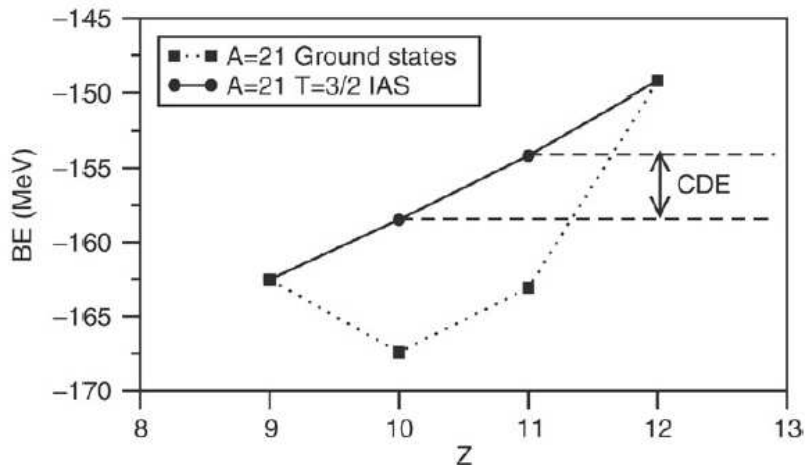
Figure 3.2: The experimental BE of the $A = 21$, $T_z = \pm 1/2, \pm 3/2$ nuclei, both for ground states and for $T = 3/2$ IAS. The CDE between the neighbouring members of the $T = 3/2$ quadruplet is indicated. It can also be noticed that ground states BE form the well-known Weizsäcker parabola. Ref.[3].

A classic application of the isospin quantum number in nuclear physics is the analysis of the mass (or BE) of IAS as a function of Z or T_z. This approach, first introduced by Wigner in 1957 [51], led to the formulation of the Isobaric Multiplet Mass Equation (IMME).

One can start from the eigenstates[6] $|\alpha, T, T_z\rangle$ of the charge-independent Hamiltonian. Hence, any charge-violating interaction H'_{CV}, which will spoil the degeneracy of the IAS energy, can be treated at the perturbative level, if the splitting is small with respect to the BE.

In the lowest-order approximation, the isospin symmetry turns out to be broken in a dynamical way[7][20]. In this manner, the Hamiltonian can be written as $H = H_{CI} + H'_{CV}$ and the total BE will become:

$$BE(\alpha, T, T_z) = \langle \alpha, T, T_z | H_{CI} + H'_{CV} | \alpha, T, T_z \rangle. \tag{3.16}$$

If charge-violating interactions emerge as a purely two-nucleons interaction, H'_{CV} can be written as a rank-2 tensor:

$$H'_{CV} = \sum_{k=0}^{2} H_{CV}^{(k)} \tag{3.17}$$

in which $k = 0, 1, 2$ are, respectively, the isoscalar, isovector and isotensor components of this interaction. Each one of these components can be related to the various NN-interactions as reported in [38]:

$$H_{CV}^{(0)} = \frac{V_{pp} + V_{nn} + V_{np}}{3} \tag{3.18}$$

$$H_{CV}^{(1)} = V_{pp} - V_{nn} \tag{3.19}$$

$$H_{CV}^{(2)} = V_{pp} + V_{nn} - 2V_{np} \tag{3.20}$$

These components are related to charge-symmetry and charge-independence. Moreover, $H_{CV}^{(1)}$ is invariant with respect to $SU(2)$ isospin group, whilst $H_{CV}^{(1)}$ and $H_{CV}^{(2)}$ are $SO(2) \subset SU(2)$ isospin

---

[6]Using the notation introduced in the last part of the previous section.

[7]In this context dynamical symmetry breaking of $SU(2)$ isospin symmetry arises from explicit physical interactions (e.g. Coulomb force or differences in nuclear forces $pp \neq np \neq nn$, instead in HEP this concept is emergent and non-perturbative (e.g. chiral symmetry breaking in QCD due to the vacuum structure of the theory).

group invariant. $H_{CV}^{(1)}$ shows that a non charge-symmetric nuclear interaction implies a non-zero isovector component. However, V_{pp} is the only term that contributes to the isovector term whose nature has a Coulomb origin. In a similar way, $H_{CV}^{(2)}$ is strongly related to charge-dependence of the NN interaction.

From what was seen previously, the total energy splitting of the isobaric multiplet is given by:

$$\Delta \text{BE}(\alpha, T, T_z) = \left\langle \alpha, T, T_z \left| \sum_{k=0}^{2} H_{\text{CV}}^{(k)} \right| \alpha, T, T_z \right\rangle. \tag{3.21}$$

By applying the Wigner-Eckart theorem, it is then possible to extract the T_z dependence of the energy splitting of the multiplet:

$$\Delta BE(\alpha, T, T_z) = \sum_{k=0}^{2} (-)^{T-T_z} \begin{pmatrix} T & k & T \\ -T_z & 0 & T_z \end{pmatrix} \langle \alpha, T \| H_{CV}^{(k)} \| \alpha, T \rangle \tag{3.22}$$

where the matrix elements with two bars denote the reduced matrix elements in the isospin space. The $3 - j$ Wigner symbols for the three k values assume analytic form, leading to the relation:

$$\Delta BE(\alpha, T, T_z) = \frac{1}{\sqrt{2T+1}} \times \left[M^{(0)} + \frac{T_z}{\sqrt{T(T+1)}} M^{(1)} + \frac{3T_z^2 - T(T+1)}{\sqrt{T(T+1)(2T+3)(2T-1)}} M^{(2)} \right] \tag{3.23}$$

whereas $M^{(k)} = \langle \alpha, T \| H_{CV}^{(k)} \| \alpha, T \rangle$ are independent of T_z but dependent on α and T, see Sec.[2.2] in [3].

Reordering terms, the IMME takes the form:

$$\Delta BE(\alpha, T, T_z) = a + bT_z + cT_z^2 \tag{3.24}$$

so, the binding energy splitting of an isobaric multiplet is quadratic in T_z and the IMME coefficients depend only on T and $M^{(k)}$. From Eq. (3.23) one can deduce that each coefficient brings information on different tensor components of the interaction.

The a coefficient is a mixture mostly dependent on the isoscalar component and a small isotensor one, while b and c are purely related, respectively, to the isovector and isotensor components. Therefore, the latter leads to information regarding the charge-symmetry and charge independence of NN attractive interaction.

The IMME holds for any isospin non-conserving interaction, not just the Coulomb force. Although its quadratic form remains intact, the coefficients can change depending on the interaction. Deviations from the quadratic form may occur due to higher-order perturbations, three-nucleons forces, or significant isospin mixing, (see Fig.3.3).
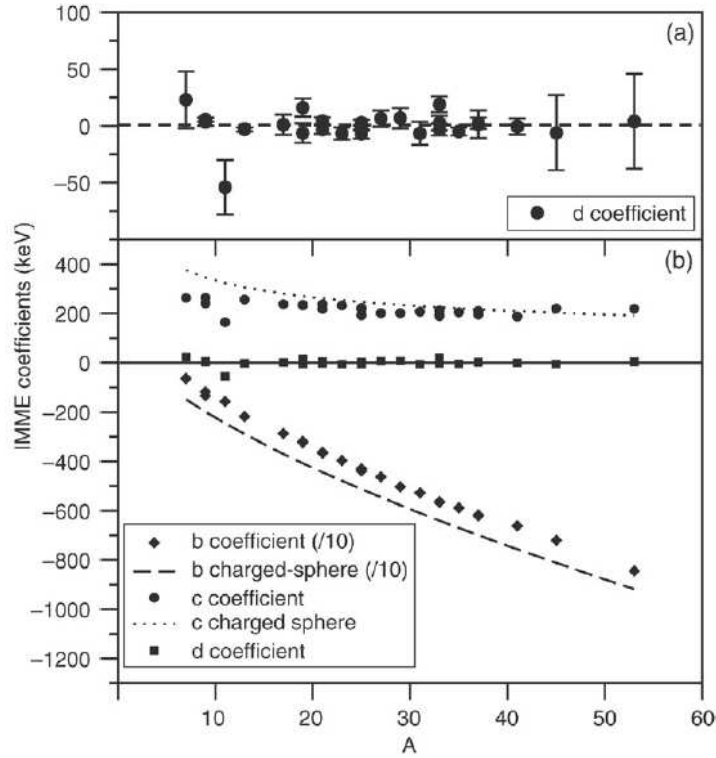
Figure 3.3: **a)** IMME coefficients related to a 'cubic IMME': $BE(T, T_z) = a + bT_z + cT_z^2 + dT_z^3$ obtained from fits to experimental $T = \frac{3}{2}$ quadruplets (from [10]. From this, it is possible to conclude that the nature of the IMME is quadratic; **b)** coefficients prediction using relations Eq.(3.26). Ref.[3].

An exhaustive knowledge of the charge-violating components of the interaction is crucial to reproduce IMME coefficients. Facing this problem directly, one can take as a first assumption that the major contribution of the energy splitting in IAS is due to the Coulomb interaction: treating the nucleus as a simply uniform charged sphere, its energy can be expressed as:

$$E_C = \frac{3e^2 Z(Z-1)}{5R_C} = \frac{3e^2}{5r_0 A^{\frac{1}{3}}} \left[\frac{A}{4}(A-2) + (1-A)T_z + T_z^2 \right]. \tag{3.25}$$

Therefore, the IMME coefficients can be rewritten as:

$$a = \frac{3e^2 A(A-2)}{20r_0 A^{\frac{1}{3}}}, \quad b = -\frac{3e^2(A-1)}{5r_0 A^{\frac{1}{3}}}, \quad c = \frac{3e^2}{5r_0 A^{\frac{1}{3}}}. \tag{3.26}$$

The predictions of coefficients b and c are reported in Fig. 3.3**b**.

3.2.1 Coulomb Displacement Energy

In more advanced calculations, a key quantity to reproduce is the Coulomb Displacement Energy (CDE), the difference in binding energy between two neighbouring members of an isobaric multiplet, as defined by Eq. (3.15).
This is directly tied to the IMME coefficients.

Specifically, for adjacent members[8]:

$$CDE(T, T_z) = -b - c(2T_z + 1) + \Delta_{nH} \tag{3.27}$$

---

[8]Recalling Eq. (3.15)

The CDE has been extensively studied, especially in the foundational works of Nolen and Schiffer in [35] and Auerbach in [1], who compared theoretical estimates with experimental data across many IAS. In the original Nolen-Schiffer analysis, the nuclear interaction was taken as charge-symmetric and charge-independent, implying that the IMME coefficients b and c arise solely from Coulomb forces. They evaluated Coulomb energy differences using independent particle models.

In this contest CDE was estimated by converting a neutron into a proton within the neutron rich nucleus of a multiplet, including contributions from direct Coulomb interaction, exchange effects and electromagnetic spin-orbit coupling.

These, however, undersestimated experimental values by about 7%, a discrepancy known as the *Nolen-Schiffer anomaly*, see the Sec.[2.3] in [3].

Further corrections, such as Coulomb distortion, isospin mixing and intrashell interactions, narrowed the gap but did not resolve it. Later studies introduced refinements like configuration mixing and core polarisation, yet the anomaly persisted.

Some works [33, 42] suggested that its origin lies in charge-symmetry breaking in the NN force, while others, like Duflo and Zuker in [17], showed that including neutron skin and quantum Coulomb effects could largely explain it, although accuracy below 100 keV remains challenging.

3.2.2 Mirror Energy Differences

For a pair of mirror nuclei, the Coulomb Energy Differences are referred as *Mirror Energy Differences* (MED). These are defined for each pair of mirror nuclei as the difference between the excitation energy as a function of J:

$$\text{MED}_{J,T} = E^*_{J,T,T_z=-|T_z|} - E^*_{J,T,T_z=|T_z|} \tag{3.28}$$

with the implicit assumption that the lowest isospin states[9] are taken into account. It is important to note that the energies of the two levels are normalised to the absolute binding energy of the ground states. Doing this, it is allowed to delete the bulk of the energy differences due to the Coulomb interaction and to study fine variations, otherwise hardly to appreciate. The previous equation can be put in another form, by using the IMME, e.g. for $T = \frac{1}{2}$ states in a pair of nuclei with $T_z = \pm\frac{1}{2}$:

$$\text{MED}_J = E^*_{J,T_z=-\frac{1}{2}} - E^*_{J,T_z=+\frac{1}{2}} = -\Delta b_J \tag{3.29}$$

and Δb_J defines the change in the b coefficient as a function of the spin J, in relation to the ground state.

As a result, MED not only reveals subtle changes in energy differences with increasing spin, but also allows us to disentangle charge-symmetry breaking effects (isovectorial terms) from those related to charge independence (isotensorial terms). If we can accurately account for all electromagnetic contributions to the MED, the remaining discrepancy with experimental data can be attributed to unknown charge-symmetry violating forces, such as those stemming from the nucleon–nucleon interaction.

In addition, MED offers valuable insight into how the nuclear structure evolves with total angular momentum.

In essence, MED serves as a tool that enhances our view of the underlying physics of excited mirror states, deepening our understanding of both charge-symmetry breaking and structural dynamics in nuclei.

---

[9]Those for which $T = |T_z|$.
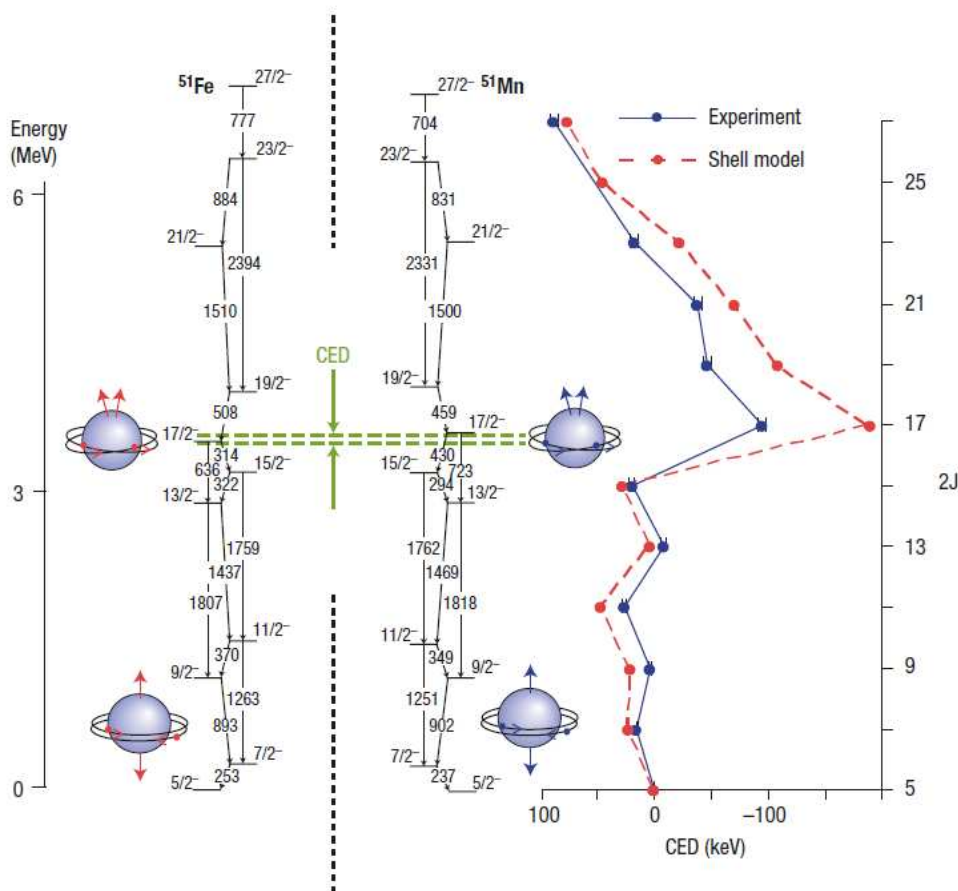
Figure 3.4: Coulomb energy differences (CEDs) for the pair of mirror nuclei ^{51}Fe (Z=26, N=25) and ^{51}Mn (Z=25, N=26).The left of the diagram shows a portion of the level schemes of the two nuclei. States are labelled by their angular momentum (J) and parity ($\pm$) quantum numbers. Gamma-decay energies in keV are also shown. On the right of the figure, the corresponding CEDs are indicated as a function of J. Ref.[46].

3.3 Origin of differences in excitation energy of analogue states

Assuming charge symmetry and charge independence of the nuclear force, excitation energy differences between IAS in mirror nuclei should stem purely from electromagnetic effect. The dominant contribution comes from the Coulomb interaction which acts only on protons and causes isospin dependence, contributing hundreds of MeV to nuclear masses and tens of MeV to the CDE. Minor contributions include the proton-neutron mass difference and other small electromagnetic terms.

When comparing excited states, large Coulomb contributions largely cancel out due to normalisation to the ground state. As reported in [3], this leads to MED and TED[10], for the shell $f_{\frac{7}{2}}$ of 100 keV and 200 keV respectively, whilst in the sd-shell, some MED values reach $200 - 300$ keV. However, these small differences act as sensitive probes of nuclear structure. If electromagnetic effects are well-modelled, the remaining deviations can signal isospin-breaking contributions from the nuclear interaction. These aspects are further explored in shell-model studies by Zuker et al. [17, 19, 30, 52].

---

[10]Triplet Energy Differences, defined as $\text{TED}_J = E^*_{J,T_z=-1} + E^*_{J,T_z=+1} - 2E^*_{J,T_z=0} = 2\Delta c_J$.

Due to these considerations, the Coulomb interaction Hamiltonian can be written as

$$H = V_{CM} + V_{cm} \tag{3.30}$$

whereas the two terms are: the monopole term V_{cm} that takes into account single-particle and bulk effect due to the spherical field, containing terms quadratic in $a_i^\dagger a_j$, and the multipole term V_{CM}, related to the rest of possible interactions, as correlations terms between nucleons belonging to the valence space. Furthermore, also the Isospin Non-Conserving (INC) nuclear contributions can be added. So, following the steps of [3], there are four different effects: the multipole and monopole Coulomb field contributions, the single-particle corrections contribution and the INC interaction contributions.

3.3.1 The Coulomb multipole term

The multipole Coulomb term V_{CM}, arises from the Coulomb contribution to the effective two-body interaction between valence nucleons. Its dependence on the angular momentum J reflects the alignment of the spins of pairs of nucleons with rotational angular momentum.
To better understand this effect, consider two identical nucleons (protons in this case), occupying the same shell, such as $f_{\frac{7}{2}}$, initially coupled to the total angular momentum $J = 0$. One way to change nuclear energy is to break this pair and recouple the nucleons with a different total J. When a pair aligns to a higher J, the Coulomb energy decreases. In particular, when the pair reaches the maximum alignment allowed by the shell (i.e. $J = 2j - 1$, that is, $J = 6$ in $f_{\frac{7}{2}}$) the Coulomb repulsion is minimised due to the maximal spatial separation among the two protons; see Fig. 3.5.
Since the Coulomb interaction is repulsive, such a spin alignment lowers the excitation energy of the nuclear state. Along a rotational band, each successive pair alignment alters the regular energy spacing of the band.
Assuming isospin symmetry, this alignment effect will occur similarly in both mirror nuclei, but the Coulomb contribution will only appear in the nucleus where protons align. In the mirror partner, neutron alignment does not produce the Coulomb effect. Therefore, analysing the Mirror Energy Differences between rotational states in mirror nuclei can reveal which type of nucleon is aligning. A positive shift in the MED typically signals neutron alignment in the proton-rich nucleus, whereas a negative shift indicates proton alignment in the neutron-rich mirror partner.
Thus, the multipole Coulomb term reflects the energetic preference for aligning nucleon pairs rather than simply increasing the rotational frequency to reach higher excited states.
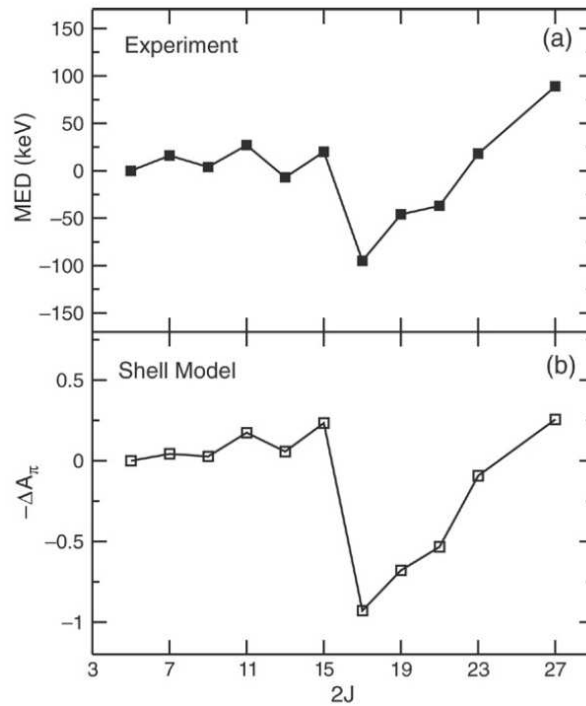
Figure 3.6: MED and alignment for the mirror $^{51}Fe - ^{51}Mn$ as a function of the angular momentum J. It can be notice the correlation between the experimental MED and the "quasi-alignment" calculated in the shell model framework, as a function of J. See Sec.[4.1.1] in [3].
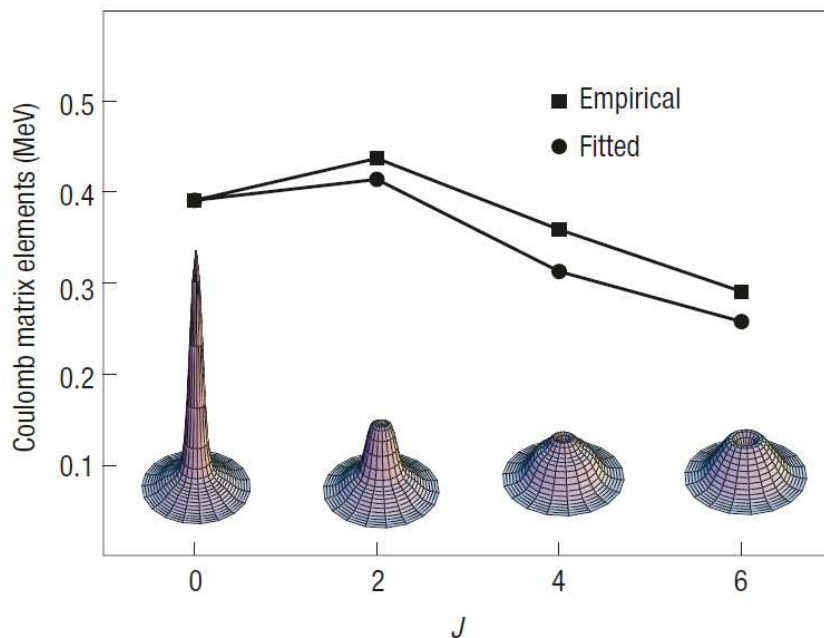
Figure 3.5: Calculation of the probability distribution for the relative distance between two identical particles in the shell $f_{\frac{7}{2}}$ as a function of their coupled angular momentum. The centre of these plots corresponds to a zero separation. Refs. [46, 47].

3.3.2 The Coulomb monopole term

In addition to the multipole term that accounts for the Coulomb interaction among protons belonging to the valence shell, to better reproduce mirror energy differences, it is necessary to take into account a monopole correction term V_{cm}. This term derives from the fact that the nuclear radius changes along the rotational band in relation to its angular momentum J.

As mentioned previously, aligning a pair of nucleons to higher spin can, in some cases, be energetically more favourable than simply increasing the rotational frequency to reach higher energy levels. For example, in nuclei within the $f_{\frac{7}{2}}$ shell, the occupation of valence orbitals other than $f_{\frac{7}{2}}$, which play a key role in generating collective low-lying states, tends to decrease along the yrast line. Since the nuclear radius depends on the occupation of these orbitals, this leads to a change in the nuclear size.

In the calculation of MED, the term V_{cm} accounts for this effect. It can be estimated by considering the Coulomb energy of a uniformly charged radius R_C:

$$E_C = \frac{3}{5}\frac{Z(Z-1)e^2}{R_C}. \tag{3.31}$$

The difference between the energy of the ground states of $T_z = \frac{\pm n}{2}$ mirror nuclei, $Z_>$ and $Z_<$, such that $Z_> = Z_< + n$, then the Coulomb energy difference of the ground state is:

$$\Delta E_C = E_C(Z_>) - E_C(Z_<) \simeq \frac{3}{5}\frac{n(2Z_> - n)e^2}{R_C}. \tag{3.32}$$

Its contribution is on the order of tens of MeV. When computing the Mirror Energy Differences (MED) for each state with spin J, viewed as a function of angular momentum, these values must be normalised to the MED of the ground state. By doing so, the monopole term ΔE_C in effectively cancels out. However, a small residual contribution remains, which can be attributed to changes in the charge radius as the angular momentum increases. This leads to the following result:

$$\Delta_M(V_{Cr}(J)) = \Delta E_C(J) - \Delta E_C(0) = \frac{3}{5}n(2Z - n)e^2 \left(\frac{1}{R_C(J)} - \frac{1}{R_C(0)}\right)$$
$$= \frac{3}{5}n(2Z - n)e^2 \left(\frac{R_C(0) - R_C(J)}{R_C^2}\right) = \frac{3}{5}n(2Z - n)e^2 \frac{\Delta R(J)}{R_C^2} \tag{3.33}$$

whereas $\Delta R(J) = R_C(J) - R_C(g.s.)$, following [18, 30, 52] this is equal for both nuclei, only Z changes. A general rule can be formulated regarding the variation of the charge radius as a function of angular momentum: orbitals with lower angular momentum are associated with larger radii, resulting in reduced Coulomb repulsion; in contrast, orbitals with higher angular momentum are more spatially confined, leading to stronger Coulomb effects. In the case of the fp-shell, for instance, the p orbital extends further than the f orbital. As protons are promoted from the p to the f orbital, an increase in Coulomb repulsion is observed. At high angular momentum, where nucleons predominantly occupy the $f_{\frac{7}{2}}$ orbital, the monopole Coulomb contribution becomes more significant compared to lower-spin sates, where the $p_{\frac{3}{2}}$ orbital still contributes notably to the wave function.

In practical terms, one can estimate variations in the charge radius by tracking changes in orbital occupation numbers along the yrast line[11]. For mirror nuclei, assuming equal charge radii, the

---

[11]Yrast states are the lowest energy states with a given angular momentum J. Plotting them in a Energy-vs-Angular Momentum graph, they will dispose along the *yrast line*.
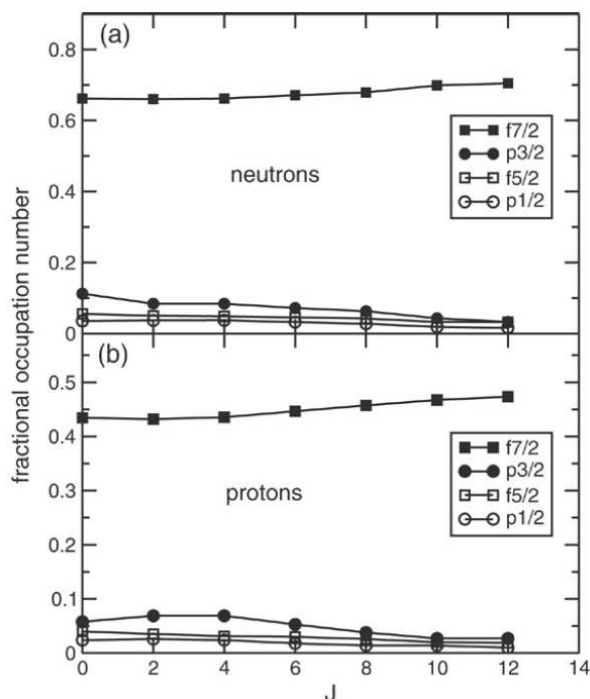
Figure 3.7: The shell model prediction of the fractional occupation number for ^{50}Cr for neutrons and protons in the fp space. From [3].

radial Coulomb contribution is obtained by averaging the occupation numbers of protons and neutrons:

$$\Delta_M(V_{Cr}) = n\alpha_r \left(\frac{m_\pi(J_{g,s}) + m_\nu(J_{g,s})}{2} - \frac{m_\pi(J) + m_\nu(J)}{2} \right), \qquad (3.34)$$

in which n is the $Z - N$ difference in the two nuclei, α_r is a parameter, that can be deduced from the single-nucleon energy, while $m_{\pi,\nu}$ encoded the information regarding occupation numbers of p-orbit in fp-shell in the wave-function for protons and neutrons with the angular momentum J. In the case of fp-shell analysis conducted in [3], this parameter is based on experimental values and is valued around 200 keV.

In the present work, this parameter is evaluated in the same way; however, as it will be shown in the next chapter, its value ranges between $50 - 200$ keV, depending on the occupation numbers and aiming for the best agreement with experimental data through a systematic study of the sd-shell. Sometimes along this work, the monopole term V_{cm} is written in the form V_{Cr} underlying its radial dependence.

3.3.3 Single-Particle Energies corrections

The next contributions one has to take into account concern the single-particle energy corrections, both for protons and neutrons, which receive different contributions from their interaction with the electromagnetic field. In particular, there are two main effects:

1. Interaction of protons in the valence space with the monopole electromagnetic field generated by the core. This contribution affects only protons. In the harmonic oscillator approximation, their energy is proportional to the square of the orbital momentum l. The expression for the protons single-particle energy splitting has been calculated by Duflo and

33

Zuker in [18]:

$$E_{ll} = \frac{-4.5 Z_{\text{cs}}^{\frac{13}{12}} \left[2l(l+1) - N(N+3)\right]}{A^{\frac{1}{3}} \left(N + \frac{3}{2}\right)} \text{ keV}, \tag{3.35}$$

in which N is the principal quantum number, l the orbital momentum and Z_{cs} is the closed shell above which the this effect acts;

2. The contribution due to the Relativistic Electromagnetic Spin-Orbit force (EMSO), that affects both protons and neutrons. Analogously to the atomic case, this interaction is caused by the Larmor precession of nucleons in the nuclear electric field due to their intrinsic magnetic momenta μ_s and by the Thomas precession of protons due to their charge and orbital magnetic moment μ_l. This contribution is different for protons and neutrons, so it provides a fine correction to the final calculus of the MED. The EMSO potential can be written in the form [3, 26, 35]:

$$V_{ls} = (g_s - g_l)\frac{1}{2m_N^2 c^2} \left(\frac{1}{r}\frac{dV_C}{dr}\right) \vec{l} \cdot \vec{s} \tag{3.36}$$

whereas m_N is the nucleon mass g_s and g_l are the gyromagnetic factors[12], coming from the expressions of Larmor and Thomas precessions, respectively linked to μ_s and μ_l. Then, assuming the potential V_C is that of a uniformly charged sphere of radius R_C, the previous expression accounting for the perturbation of the single-nucleon energies caused by the EMSO force is:

$$E_{1s} \simeq (g_s - g_l)\frac{1}{2m_N^2 c^2}\left(-\frac{Ze^2}{R_C^3}\right)\left\langle \vec{l} \cdot \vec{s}\right\rangle. \tag{3.37}$$

This contribution has a different sign depending on whether it is the orbit of a proton or a neutron and also depends on the spin-orbit coupling: $\vec{l} \cdot \vec{s} = \frac{l}{2}$ if $j = l + s$, while $\vec{l} \cdot \vec{s} = -\frac{l+1}{2}$ if $j = l - s$. By doing further approximations, one reaches the values reported in the following Table (3.1):

	π	π	ν	ν
	$j = l + \frac{1}{2}$	$j = l - \frac{1}{2}$	$j = l + \frac{1}{2}$	$j = l - \frac{1}{2}$
E_{ls}	$-42\frac{Z}{A}l$ keV	$42\frac{Z}{A}(l+1)$ keV	$35\frac{Z}{A}l$ keV	$-35\frac{Z}{A}(l+1)$ keV

Table 3.1: Approximate values of the energy shifts produced by the EMSO potential obtained from Eq. (3.37).

To better understand how this effect contributes to the excitation energy, consider the example of a nucleus in which a proton is excited from the $d_{\frac{3}{2}}$ shell to the $f_{\frac{7}{2}}$ shell. This configuration results in a lower excitation than in the mirror nucleus, where the same excitation involves a neutron. According to Table (3.1), for protons, the spin–orbit potential raises the $d_{\frac{3}{2}}$ shell by 63 keV and lowers the $f_{\frac{7}{2}}$ shell by 63 keV, increasing the gap by $\Delta E - 126$ keV, where ΔE is the unperturbed energy difference. For neutrons, the $d_{\frac{3}{2}}$ shell is lowered and the $f_{\frac{7}{2}}$ is raised by 52.5 keV, increasing the gap by $\Delta E - 105$ keV. Thus, the proton excitation requires 231 keV less energy than the neutron excitation, highlighting the significant contribution of the electromagnetic spin-orbit interaction to MED.

---

[12]For protons $g_s^\pi = 5.586$, $g_l^\pi = 1$, while for neutrons $g_s^\pi = -3.828$, $g_s^\pi = 0$.
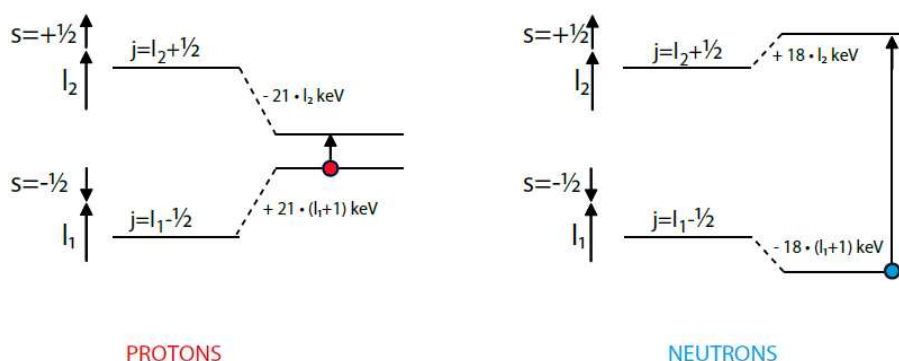
Figure 3.8: Increasing and decreasing of neighbouring orbits, caused by different $l - s$ alignment due to the V_{ls}. Refs. [45, 49].

3.3.4 Isospin Non-Conserving Nuclear Interactions

Assuming isospin symmetry, the difference between the experimental MED and its theoretical prediction, which accounts for all known Coulomb corrections, should be minimal. However, this is not always the case. Such discrepancies suggest that Isospin Non-Conserving (INC) nuclear interactions may play a significant role. For instance, in many mirror nuclei within the fp-shell, the observed MED cannot be fully explained by electromagnetic effects alone [2].

The most logical approach to account for INC effects would involve constructing an effective potential that includes an isospin non-conserving term. However, this is a challenging task. Consequently, it is often more practical to develop phenomenological models based on experimental observations. A model developed by Zuker et al. [52] aimed to estimate the contribution of INC nuclear interactions to MED in the $f_{\frac{7}{2}}$ shell, specifically studying the mirror pair $^{42}Ti - ^{42}Ca$. The results show that electromagnetic effects alone cannot fully account for the experimental MED values. For example, a significant discrepancy of around 100 keV is observed at the $J^\pi = 2^+$ state.

	$J = 0$	$J = 2$	$J = 4$	$J = 6$
Coulomb Contribution V_C(keV)	81.60	24.60	6.40	-11.40
$MED\left[^{42}\text{Ti} - {}^{42}\text{Ca}\right] - V_C$(keV)	5.38	92.55	4.57	-47.95

Table 3.2: MED in $^{42}Ti - ^{42}Ca$, from [52].

To address this, an ansatz was proposed: assuming a 100 keV difference in the matrix elements between the proton and neutron pairs in the $f_{\frac{7}{2}}$ shell coupled to $J = 2$. This approach successfully reproduced MED values in other fp-shell nuclei with different mass numbers (e.g., $A = 47, 49, 50, 51$). Later, Kaneko et al. [27] suggested an alternative parametrisation using a 100 keV difference for the matrix elements $J = 0$. Further studies confirmed that the relevant INC effect lies in the difference between the matrix elements in $J = 2$ and $J = 0$, rather than in their absolute values.

Eventually, this approach was extended beyond the $f_{\frac{7}{2}}$ shell to all orbitals of the fp-shell, and even to the sd-shell, proving successful in explaining MED in cases such as the pair $^{23}Mg - ^{23}Na$, as exposed in [7].

The physical origin of INC term suggests that it may arise from the breaking of the charge symmetry in the NN interaction. Using known proton-proton and neutron-neutron scattering lengths, corrected to exclude electromagnetic contributions, the predicted INC matrix elements are:

$$V_B^{J=0} \approx 11 \, \text{keV} \quad V_B^{J=2,4,6} = 0 \, \text{keV} \tag{3.38}$$

However, these values disagree (both in sign and magnitude) with those found in prior models [2], implying that unaccounted electromagnetic effects may be influencing the INC interaction. It is important to note that, while in nuclei with mass number $A = 40 \div 55$ the $f_{\frac{7}{2}}$ shell dominates the wave functions, in the sd-shell nuclei, all three orbitals play a significant role. Therefore, an isospin-breaking term V_B must be considered for each orbital. For the sake of simplicity, the same value, set to -70 keV for positive parity states and -100 keV for negative parity states, will be applied uniformly to all orbitals within a given major shell.
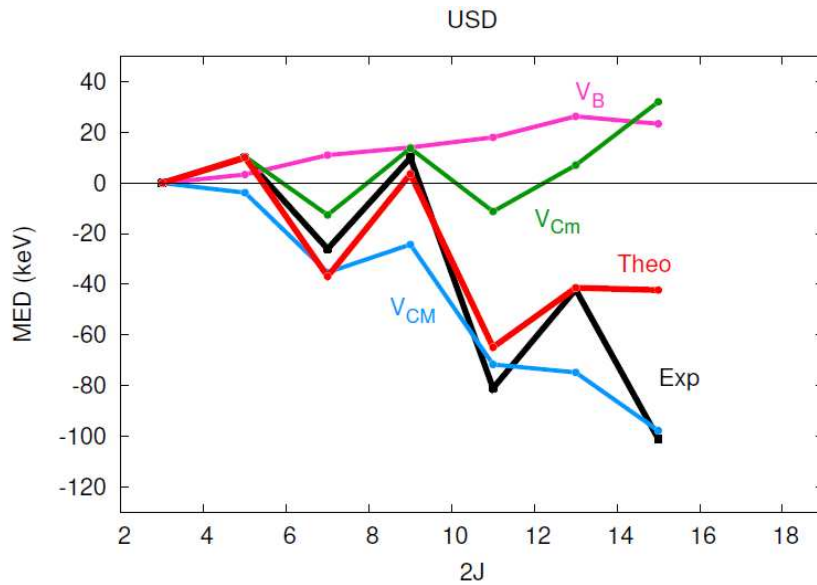
Figure 3.9: Example of experimental and theoretical MED in mirror nuclei $^{23}Mg - {}^{23}Na$ obtained with the USD interaction. The isospin symmetry breaking (ISB) part V_B, the radial contribution V_{Cm} and the multipole term V_{CM} are enlightened. Ref.[8].

In the next chapters, all these techniques will be applied to mirror nuclei belonging to the sd-shell, with masses $A = 19 - 35$ in order to confirm the validity of this theoretical approach and verify the robustness of the current approach to nuclear physics far from stability.

Chapter 4

Study of medium-mass mirror nuclei

This chapter is the core of this work and is dedicated to the application of all the shell model theoretical notions developed in the last years to the medium-mass nuclei. More specifically, here the systematic study of MED of nuclei belonging to sd-shell with mass range $A = 19 - 35$ will be treated; see Fig. 4.1. Following a systematic approach, all mirror nuclei pairs listed in the tables (A.1-A.4) will be analysed in the same way.
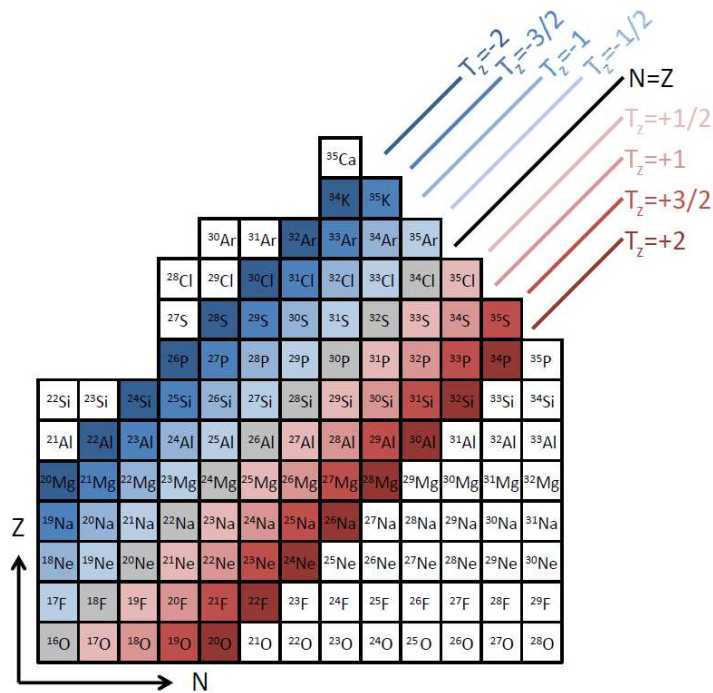
Figure 4.1: A particular of the Segré chart with the sd-shell mirror nuclei studied in this work. In evidence the isospin T_z component. Picture adapted from [49]. All the nuclei shown are already been discovered [16].

Positive parity states were studied using the USDA effective interaction [12]: this allows multi-particle excitations, using the $^{16}_{8}O_8$ as the core and the $sd-$shell as a valence space, so the orbits $d_{\frac{3}{2}}$, $s_{\frac{1}{2}}$, $d_{\frac{5}{2}}$. For the negative parity states, which are intruder states, due to the fact that their parity is not the natural one inside the $sd-$shell, the PSDPF was used as an effective interaction

[9]. The PSDPF uses $^4_2He_2$ as the core, and the valence space is now extended from the $p-$shell to the $fp-$shell, to allow for the promotion of a nucleon from the $p-$shell to the $sd-$shell and from the $sd-$shell to the $fp-$shell.

MED comparisons have been made using the following relations:

$$MED^J_{exp} = E_J(Z_>) - E_J(Z_<) \tag{4.1}$$

$$MED^J_{Th.} = \Delta\langle V_{CM} \rangle + \Delta\langle V_{cm} \rangle + \Delta\langle E_{ll} \rangle + \Delta\langle E_{ls} \rangle + \Delta\langle V_B \rangle \tag{4.2}$$

Calculations have been performed using the shell model code ANTOINE, in the context of the interacting shell model, taking into account the yrast states[1]. Only pairs of mirror nuclei with at least two known experimental states[2] were considered. The experimental states selected for analysis have been taken from the NNDC database [16], using the Evaluated Nuclear Structure Data File (ENSDF) and the Experimental Unevaluated Nuclear Data List (XUNDL) to compare the theoretical prediction with the newest available experimental data. The objective of this study is not to perform a best-fit procedure but rather to conduct a systematic analysis of the MED of the nuclei within the sd-shell. To do this, it is fundamental to fix the parameters described in the previous chapter.

Regarding the isospin-symmetry breaking term Sec.[3.3.4], the strength that accounts for $J = 0$ couplings in the $T = 1$ channels is set to -70 keV for the study of positive parity states and to -100 keV for negative parity states. The different choice for the parameters has been adopted after a brief analysis done at the beginning of this work, in which it emerged how negative states MED improved fixing $\alpha_{VB} = -100$ keV.

Concerning the radial term, since the $s_{\frac{1}{2}}$ orbit is the lowest in angular momentum, it has a greater radius as reported in [6] and its occupation characterises the radial term in the sd-shell. For the parameter α_r, defined in Sect. [3.3.2] Eq.(3.34), the values have been set equal to 200 keV for the isobars with $A \leq 27$, due to the low occupations $s_{\frac{1}{2}}$, and to 50 keV for those masses $29 \leq A \leq 35$, in which the total occupation $m_{s_{\frac{1}{2}}} = m_\pi + m_\nu > 1$ with at least one nucleon in the orbit $s_{\frac{1}{2}}$.

4.1 Positive parity states

An examination of the MED associated with states of positive parity is presented here; after that, a general analysis that compares all the results will be performed. Only states with natural parity in the sd-shell will be analysed. Recall that:

- the **core** is $^{16}_8O_8$;

- the **valence space** is the sd-shell, spanned by the orbits $(1d_{\frac{5}{2}}, 2s_{\frac{1}{2}}, 1d_{\frac{3}{2}})$.

Structure of the following paragraphs For each couple of mirror nuclei will be reported a table containing the experimental data and the results of the theoretical calculations, the reference of the figures referring to the data reported in the tables, and a comment on the analysis done. This will be done for either positive- and negative-parity states analysis.

---

[1]With a few minor exceptions, which will be clarified later.

[2]The ground states plus an yrast excited state above it.

4.1.1   Mirror nuclei with $T = \frac{1}{2}$

The net difference $|N - Z| = 1$, so in a mirror pair there is a nucleus with an excess of a proton and the other one has an excess of a neutron.

A=19   In the mirror pair ^{19}Ne and ^{19}F, as can be seen from the Tab.4.1, the theory captures the shape and trend of the MED, but slightly overpredicts its magnitude, from ≈ 7 keV for the lower spin state to ≈ 30 keV for the higher one. These discrepancies are not large, suggesting that the relevant physical ingredients are mostly included. From the theoretical contributions, see Fig.4.2, it can be observed that the radial contribution increases with the spin due to the decrease in the occupation of the $s_{\frac{1}{2}}$ orbit, which has a larger radius, while the Coulomb multipole term decreases due to angular momentum alignment. In this case, it is possible to affirm that the nucleons couples involved in the alignment are pp in ^{19}Ne and nn in ^{19}F. The ISB term provides a modest correction as well as the single-particle corrections term.

J^π	$E_{exp}{}^{19}$Ne	$E_{exp}{}^{19}$F	E_{th}	MED_{exp}	MED_{th}	ΔV_{CM}	ΔE_{ll+ls}	ΔV_{Cr}	ΔV_B
$1/2^+$	0	0	0	0	0	0	0	0	0
$5/2^+$	238	197	47	41	48	-0.05	-8	62	-6
$9/2^+$	2795	2780	2521	15	32	-52	-6	63	27
$13/2^+$	4635	4648	4440	-13	16	-93	-30	111	27

Table 4.1: Experimental data and theoretical calculations for the ^{19}Ne and ^{19}F. The table is structured in the following way: total angular momenta and the parity of the states; the experimental excitation energy E_{exp} [16]; the calculated energy E_{th}; the experimental and theoretical MED; the Coulomb multipole term ΔV_{CM}, the single-particle corrections term ΔE_{ll+ls}, the radial term ΔV_{Cr} and contributions from the isospin-breaking term ΔV_B. All energies are given in keV.

A=21   Even in the mirrors ^{21}Na and ^{21}Ne, theoretical MED overestimates the experimental data, see Tab.4.2, especially in the high-spin regime $J \geq \frac{9}{2}$. The same happens for the radial term, due to the increasing occupation of orbitals with larger spin having smaller radii. In fact, to reach higher spin, it is convenient to decrease the occupation of $s_{\frac{1}{2}}$, in favour of orbits with higher J. This is also reflected in the values of the ΔE_{ll+ls} term. The trend change from $\frac{7}{2}^+$ to $\frac{9}{2}^+$ is mainly due to the increase in the radial and isospin-breaking contributions. Observing Fig.4.3, it can be seen that the V_B term is crucial in these calculations because it is the only term that gives negative contributions to the theoretical MED. A positive MED value is also predicted at $\frac{13}{2}^+$.

J^π	$E_{exp^{21}\text{Na}}$	$E_{exp^{21}\text{Ne}}$	E_{th}	MED_{exp}	MED_{th}	ΔV_{CM}	$\Delta E_{\text{ll+ls}}$	ΔV_{Cr}	ΔV_B
$3/2^+$	0	0	0	0	0	0	0	0	0
$5/2^+$	332	351	299	-19	3	-7	2	14	-5
$7/2^+$	1716	1746	1776	-30	-6	3	6	-1	-14
$9/2^+$	2829	2867	2801	-38	5	-12	14	16	-13
$11/2^+$	4419	4433	4374	-14	41	3	13	44	-20
$13/2^+$	\	6448	6230	\	67	31	19	51	-34

Table 4.2: Experimental energies [16] and theoretical calculations for the ^{21}Na and ^{21}Ne. Idem as in Tab.4.1.

A=23   In the mirror couple of ^{23}Mg and ^{23}Na, the typical staggering behaviour, see Fig.4.4, is captured by the theoretical calculations. The theory systematically underestimates negative MED while overestimates positive ones, with a difference of about 50 keV for states with $J > \frac{11}{2}$. Moving towards higher spin, observing the data reported in Tab.4.3, the alignment of angular momenta enhances the multipole Coulomb term, the ll and ls contributions, increasing spatial overlaps and Coulomb repulsion (clearly observable by the red line). The increase in the V_{CM} term reflects the increase in magnitude in higher spin states, whereas the trend of the radial monopole term tells how the occupancy of the $s_{\frac{1}{2}}$ orbit varies with J, balancing the negative terms for large J. In conclusion, it is possible to affirm that the theory well describes this case.

J^π	$E_{exp^{23}\text{Mg}}$	$E_{exp^{23}\text{Na}}$	E_{th}	MED_{exp}	MED_{th}	ΔV_{CM}	$\Delta E_{\text{ll+ls}}$	ΔV_{Cr}	ΔV_B
$3/2^+$	0	0	0	0	0	0	0	0	0
$5/2^+$	451	440	447	11	20	1	3	12	4
$7/2^+$	2052	2076	2185	-24	-23	-20	-6	-12	15
$9/2^+$	2715	2704	2828	11	31	-10	8	16	17
$11/2^+$	5454	5534	5527	-81	-54	-47	-25	-8	25
$13/2^+$	6195	6235	6321	-41	-14	-59	-7	18	34
$15/2^+$	8938	9040	8921	-102	-24	-70	-28	45	29

Table 4.3: Experimental energies [16] and theoretical calculations for the ^{23}Mg and ^{23}Na. Idem as in Tab.4.1.

A=25   The experimental MED of the ^{25}Al and ^{25}Mg mirror pair are very small, see Tab.4.4. reaching nearly +20 keV at $J^\pi = \frac{9}{2}^+$. However, theoretical values describe in good agreement the trend of the data. From the contributions panel in the Fig.4.5, it can be seen how the calculations systematically underestimate the experimental data, but the marginal difference confirms the validity of the theory. Moreover, two positive MED are predicted at $\frac{11}{2}^+$ and $\frac{13}{2}^+$.

J^π	$E_{exp^{25}Al}$	$E_{exp^{25}Mg}$	E_{th}	MED_{exp}	MED_{th}	ΔV_{CM}	ΔE_{ll+ls}	ΔV_{Cr}	ΔV_B
$5/2^+$	0	0	0	0	0	0	0	0	0
$7/2^+$	1613	1612	1739	1	-12	21	8	-24	-17
$9/2^+$	3424	3405	3515	19	3	31	13	-13	-27
$11/2^+$	\	5252	5079	\	18	27	10	-9	-10
$13/2^+$	\	5461	5529	\	148	124	43	27	-45

Table 4.4: Experimental energies [16] and theoretical calculations for the ^{25}Al and ^{25}Mg. Idem as in Tab.4.1.

A=27   In this case of the mirror nuclei ^{27}Si and ^{27}Al, as can be seen from the Tab.4.5, the experimental MED decreases sharply with increasing spin, reaching approximately -95 keV at $J^\pi = \frac{9}{2}^+$. The theoretical calculation reproduces the qualitative behaviour but significantly underestimates the magnitude, particularly at $J^\pi = \frac{9}{2}^+$, where the discrepancy exceeds 80 keV. The radial correction is strongly attractive and shows the largest variation, especially negative for $J^\pi = \frac{7}{2}^+$ and $J^\pi = \frac{9}{2}^+$, reflecting the high occupancy of the $s_{\frac{1}{2}}$ orbit. This highlights its critical role in shaping the downward trend of the MED visible from the Fig.4.6. The ΔE_{ll+ls} term increases moderately with spin and contributes decisively to the overall trend, together with the isospin-breaking contribution.

J^π	$E_{exp^{27}Si}$	$E_{exp^{27}Al}$	E_{th}	MED_{exp}	MED_{th}	ΔV_{CM}	ΔE_{ll+ls}	ΔV_{Cr}	ΔV_B
$5/2^+$	0	0	0	0	0	0	0	0	0
$7/2^+$	2164	2212	2304	-48	-69	15	-7	-78	1
$9/2^+$	2910	3004	3036	-94	-10	-6	34	-49	11
$11/2^+$	4447	4510	4478	-63	39	-17	31	9	16

Table 4.5: Experimental energies [16] and theoretical calculations for the ^{27}Si and ^{27}Al. Idem as in Tab.4.1.

A=29   In the case of mirrors ^{29}P and ^{29}Si, MED values are large, see Tab.4.6, oscillating between +100 and -100 keV. Theoretical predictions, as can be seen from Fig.4.7, qualitatively follow the trend of the experimental data, but with some discrepancies that increase with spin. From the contributions panel, one can notice that all the terms present a typical staggering trend, in particular the ΔE_{ll+ls} term. The radial and isospin-breaking terms are fundamental to reproduce well the experimental data, especially at higher spins, in which they contribute to lowering the values of V_{CM} and ΔE_{ll+ls}. A positive MED is also predicted at $\frac{11}{2}^+$.

A=31   The experimental MED of the couple ^{31}S and ^{31}P, show a strong, staggering trend with large negative values developing at higher spin, see Tab.4.7. The curve starts slightly negative at $\frac{1}{2}^+$, oscillates around zero, and then falls below -100 keV at $\frac{11}{2}^+$. The theoretical prediction in this case fails a little: up to the state $\frac{7}{2}^+$ the trend is not well reproduced, while it becomes aligned with experimental data, even if it overestimates them, at higher spin, in particular at $\frac{11}{2}^+$ where the shift is about 80 keV; see Fig.4.8. The terms V_{CM} and ΔE_{ll+ls} show a marked spin dependence, which becomes significantly negative at $\frac{7}{2}^+$ and beyond, reaching below -30 keV. The monopole radial term vary smoothly but characterises both the first part, in which the experimental trend is not reproduced, and the second part, in which the trend is captured, but

J^π	$E_{exp^{29}P}$	$E_{exp^{29}Si}$	E_{th}	MED_{exp}	MED_{th}	ΔV_{CM}	ΔE_{ll+ls}	ΔV_{Cr}	ΔV_B
$1/2^+$	0	0	0	0	0	0	0	0	0
$3/2^+$	1384	1273	1252	110	81	23	46	14	-2
$5/2^+$	1954	2028	2062	-74	-29	7	-1	-17	-18
$7/2^+$	4081	4080	4219	1	68	17	56	-4	-1
$9/2^+$	4642	4741	4593	-99	-14	13	6	-11	-21
$11/2^+$	\	7139	7049	\	74	60	44	-3	-27

Table 4.6: Experimental energies [16] and theoretical calculations for the ^{29}P and ^{29}Si. Idem as in Tab.4.1.

with the aforementioned shift. Fundamental is the V_B contribution, which is always positive, modelling the overall theoretical MED, underlying how the ISB contributions become decisive at higher spin states.

J^π	$E_{exp^{31}S}$	$E_{exp^{31}P}$	E_{th}	MED_{exp}	MED_{th}	ΔV_{CM}	ΔE_{ll+ls}	ΔV_{Cr}	ΔV_B
$1/2^+$	0	0	0	0	0	0	0	0	0
$3/2^+$	1249	1266	1104	-17	18	-10	-6	19	15
$5/2^+$	2234	2234	2342	1	-19	-28	-21	-5	35
$7/2^+$	3350	3415	3437	-65	-28	-29	-32	11	22
$9/2^+$	5301	5343	5316	-42	17	-8	0	7	17
$11/2^+$	6343	6453	6683	-111	-42	-37	-32	-8	35
$13/2^+$	9154	9177	9309	-23	-39	-61	-7	-16	44

Table 4.7: Experimental energies [16] and theoretical calculations for the ^{31}S and ^{31}P. Idem as in Tab.4.1.

A=33 For the ^{33}Cl and ^{33}S mirror pair, both the experiment and the theory agree on the trend; see the Tab.4.8 and the Fig.4.9. MED rises from $\frac{3}{2}^+$ to a peak at $\frac{5}{2}^+ \approx 20$ keV, then drops at $\frac{7}{2}^+$. The theoretical curve closely matches both the magnitude and shape of the experimental MED, especially at low spin. This suggests that the theoretical framework captures the dominant contributions well at low spin but fails when increasing spin, principally due to the sharp negative values of V_B and E_{ll+ls}. Furthermore, a positive MED is predicted at $\frac{9}{2}^+$.

J^π	$E_{exp^{33}Cl}$	$E_{exp^{33}S}$	E_{th}	MED_{exp}	MED_{th}	ΔV_{CM}	ΔE_{ll+ls}	ΔV_{Cr}	ΔV_B
$3/2^+$	0	0	0	0	0	0	0	0	0
$5/2^+$	1986	1967	1913	19	21	-11	4	22	6
$7/2^+$	2975	2969	2991	6	-37	33	-36	12	-46
$9/2^+$	\	4049	4194	\	8	6	1	7	-6

Table 4.8: Experimental energies [16] and theoretical calculations for the ^{33}Cl and ^{33}S. Idem as in Tab.4.1.

A=35 Regarding the mirrors ^{35}Ar and ^{35}Cl, the behaviour observed, see the Tab.4.9, shows that the theory underestimates the experimental MED, while preserving the trend. From the contribution panel, see Fig.4.10, it becomes evident that the Coulomb multipole term and the isospin-breaking term manifest opposite behaviour, as well as the monopole term and single-particle corrections. Nevertheless, the calculations follow the correct experimental trend. In addition, a negative MED is predicted at $\frac{9}{2}^+$.

J^π	$E_{exp^{35}\text{Ar}}$	$E_{exp^{35}\text{Cl}}$	E_{th}	MED_{exp}	MED_{th}	ΔV_{CM}	ΔE_{ll+ls}	ΔV_{Cr}	ΔV_B
$3/2^+$	0	0	0	0	0	0	0	0	0
$5/2^+$	1751	1763	1598	-12	-3	-8	-15	13	7
$7/2^+$	2603	2646	2776	-43	-13	-33	-12	-1	33
$9/2^+$	\	3944	4093	\	-13	-8	-16	5	6

Table 4.9: Experimental energies [16] and theoretical calculations for the ^{35}Ar and ^{35}Cl. Idem as in Tab.4.1.

4.1.2 Comment on $T = \frac{1}{2}$

The analysis of mirror energy differences in odd A, $T = 1/2$ mirror nuclei across the sd-shell ($A = 19$–35) reveals a complex but interpretable behaviour driven by evolution of the nuclear structure with the spin. Because of their even-odd nature, these nuclei are particularly sensitive to single-particle effects, resulting in MED trends that vary more than in even-even systems. In many cases a general increase in MED magnitude with spin is observed. Theoretical shell-model calculations generally reproduce the qualitative MED behaviour. Quantitative agreement is often within 20–50 keV, but discrepancies up to $\sim 100\,\text{keV}$ occur, especially in $A = 25, 29, 31$. Overall, while the model captures the major mechanisms shaping MED across this mass range, the data also expose specific nuclei and spin regions where further refinement of valence space is necessary.
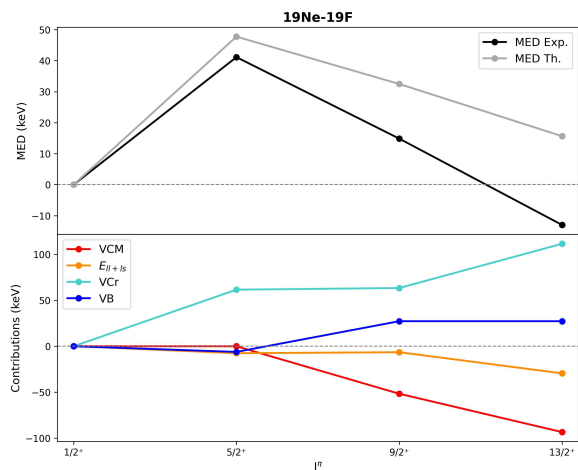

Figure 4.2: **Top panel:** the experimental MED values and theoretical predictions for the ^{19}Ne and ^{19}F mirror pair. **Bottom panel:** the different contributions to the theoretical prediction.

Figure 4.3: **Top panel:** the experimental MED values and theoretical predictions for the ^{21}Na and ^{21}Ne mirror pair. **Bottom panel:** the different contributions to the theoretical prediction.

Figure 4.4: **Top panel:** the experimental MED values and theoretical predictions for the ^{23}Mg and ^{23}Na mirror pair. **Bottom panel:** the different contributions to the theoretical prediction.

Figure 4.5: **Top panel:** the experimental MED values and theoretical predictions for the ^{25}Al and ^{25}Mg mirror pair. **Bottom panel:** the different contributions to the theoretical prediction.

Figure 4.6: **Top panel:** the experimental MED values and theoretical predictions for the ^{27}Si and ^{27}Al mirror pair. **Bottom panel:** the different contributions to the theoretical prediction.

Figure 4.7: **Top panel:** the experimental MED values and theoretical predictions for the ^{29}P and ^{29}Si mirror pair. **Bottom panel:** the different contributions to the theoretical prediction.
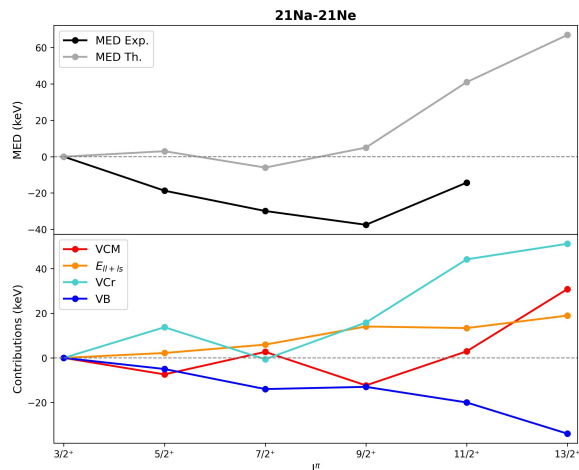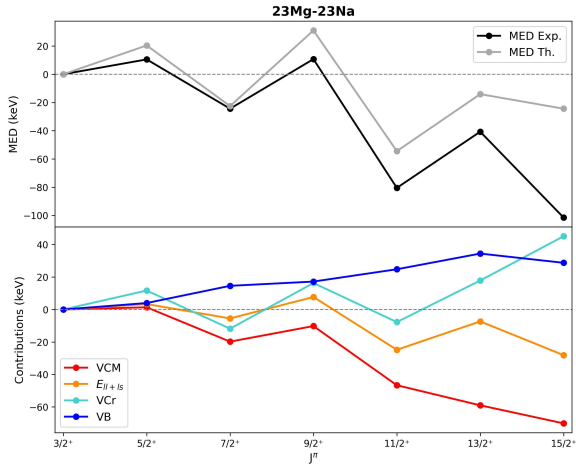
Figure 4.8: **Top panel:** the experimental MED values and theoretical predictions for the ^{31}S and ^{31}P mirror pair. **Bottom panel:** the different contributions to the theoretical prediction.

Figure 4.9: **Top panel:** the experimental MED values and theoretical predictions for the ^{33}Cl and ^{33}S mirror pair. **Bottom panel:** the different contributions to the theoretical prediction.
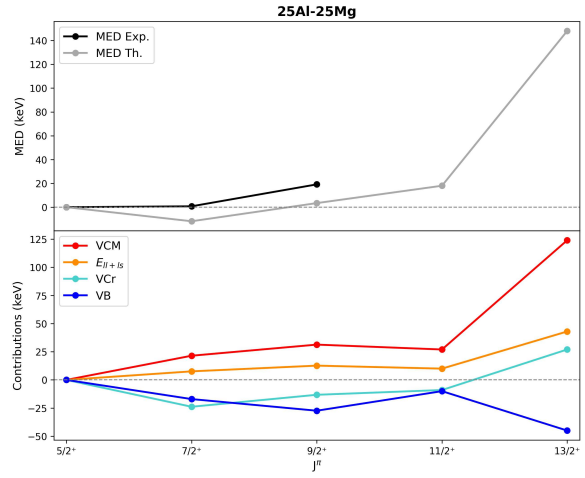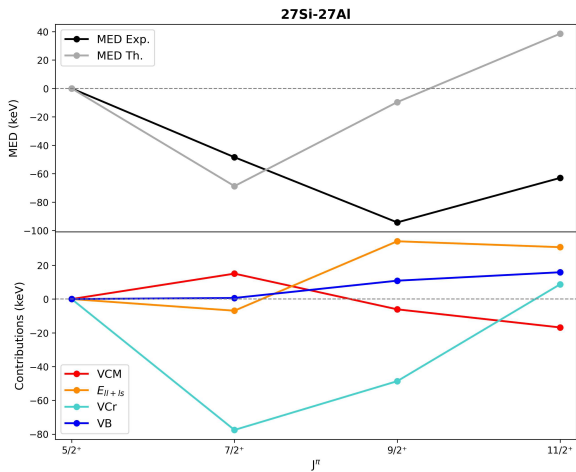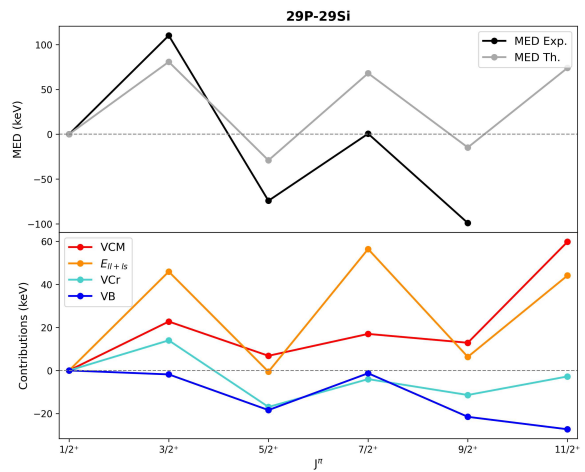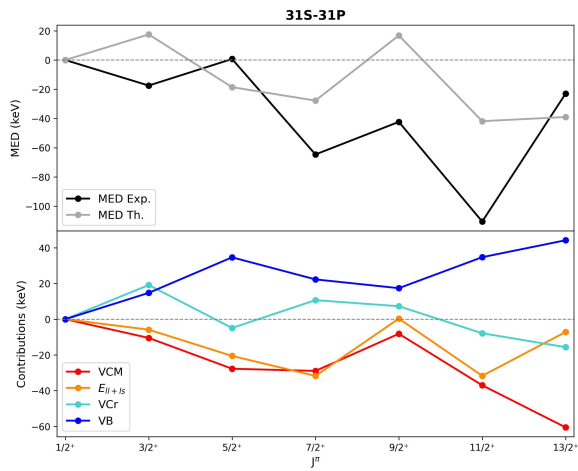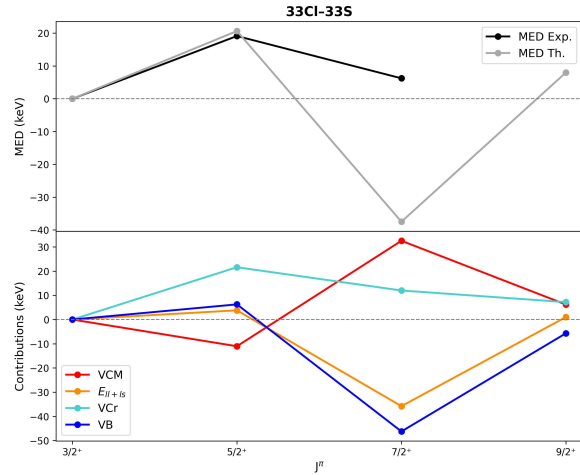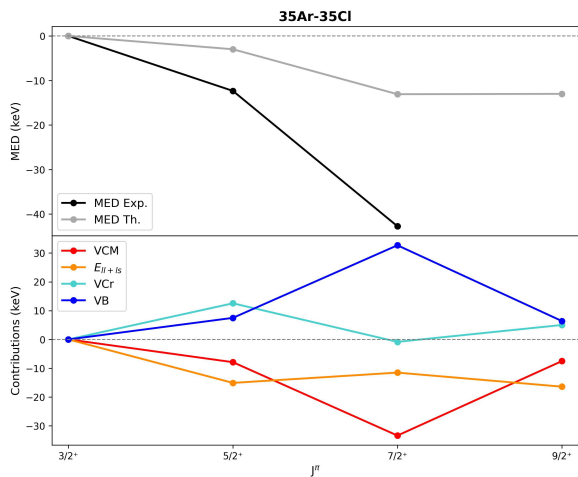

Figure 4.10: **Top panel:** the experimental MED values and theoretical predictions for the ^{35}Ar and ^{35}Cl mirror pair are displayed. **Bottom panel:** the different contributions to the theoretical prediction.

4.1.3   Mirror nuclei with $T = 1$

Now the net difference $|N - Z| = 2$, so in a mirror pair there is a nucleus with an excess of two protons and the other one has an excess of two neutrons. As a consequence, see the Tab. A.2, there are even-even and odd-odd nuclei. This different nature of the nuclei may influence the different contributions involved in the MED calculations.

A=20   Observing the Fig.4.11 of the mirrors ^{20}Na and ^{20}F, the theoretical calculations capture the experimental trend, with a growing discrepancy in magnitude with increasing spin. This increment can be principally related to the radial term, that is the dominant contribution caused by a decreasing $s_{\frac{1}{2}}$ orbit occupation, as one can see from the contributions; see Tab.4.10. The multipole, the isospin-breaking and the single-particle correction terms modulate the trend, but do not dominate. The increase in magnitude of the Coulomb multipole term can be related to the breaking of a pp couple in ^{20}Na and a pair of neutrons in ^{20}F. A positive MED value is predicted at 5^+.

J^π	$E_{exp\,^{20}\mathrm{Na}}$	$E_{exp\,^{20}\mathrm{F}}$	$\mathrm{E_{th}}$	$\mathrm{MED_{exp}}$	$\mathrm{MED_{th}}$	ΔV_{CM}	$\Delta E_{\mathrm{ll+ls}}$	ΔV_{Cr}	ΔV_B
2^+	0	0	0	0	0	0	0	0	0
3^+	596	656	580	−60	−52	−9	20	−67	4
4^+	802	823	814	−21	25	−28	5	52	−4
5^+	\\	1824	1740	\\	30	−18	17	46	−15

Table 4.10: Experimental data and theoretical calculations for the ^{20}Na and ^{20}F. Idem as in Tab.4.1.

A=22   In this case the theoretical curve of the ^{22}Mg and ^{22}Ne mirror couple, exposed in Fig.4.12, follows the experimental trend only for the lower spin states, then at higher spin it systematically overestimates the data. From the contributions reported in Tab.4.11, it can be seen that this behaviour is closely linked to that of the radial part, especially at higher spin, due to the decreasing occupancy of the $s_{\frac{1}{2}}$ orbit from $2^+ \to 6^+$. The only ever negative term is that of the Coulomb multipole.

J^π	$E_{exp\,^{22}\mathrm{Mg}}$	$E_{exp\,^{22}\mathrm{Ne}}$	$\mathrm{E_{th}}$	$\mathrm{MED_{exp}}$	$\mathrm{MED_{th}}$	ΔV_{CM}	$\Delta E_{\mathrm{ll+ls}}$	ΔV_{Cr}	ΔV_B
0^+	0	0	0	0	0	0	0	0	0
2^+	1247	1275	1309	−28	−34	−11	−5	−27	9
4^+	3308	3357	3323	−49	−19	−10	−6	−8	5
6^+	6254	6311	6266	−57	14	−35	6	28	15

Table 4.11: Experimental data and theoretical calculations for the ^{22}Mg and ^{22}Ne. Idem as in Tab.4.1.

A=24   In the ^{24}Al and ^{24}Na mirror nuclei, there are two states to examine and a theoretical prediction for a third state at 6^+. As can be seen from Tab.4.12, the theoretical calculations for the state 5^+ are in line with the experimental results. By observing the Fig.4.13, unlike the two previous pairs, the MED are now positive and from the contributions panel it is possible to see how all the terms give positive values to MED. The prediction of 6^+ negative MED value is driven by the behaviour of the radial term at higher spin, highlighting a larger $s_{\frac{1}{2}}$ occupation.

J^π	$E_{exp^{24}\text{Al}}$	$E_{exp^{24}\text{Na}}$	E_{th}	MED_{exp}	MED_{th}	ΔV_{CM}	ΔE_{ll+ls}	ΔV_{Cr}	ΔV_B
4^+	0	0	0	0	0	0	0	0	0
5^+	1539	1514	1557	25	35	9	8	13	6
6^+	3875	\	3929	\	-2	29	18	-48	-1

Table 4.12: Experimental data and theoretical calculations for the ^{24}Al and ^{24}Na. Idem as in Tab.4.1.

A=26 The mirror couple case ^{26}Si$-^{26}$Mg is more complex, as can be seen in Fig.4.14. The experimental data are well reproduced by the model for the states 2$^+$ and 4+. The model fails for the states 3+ and 5+, see Tab.4.13, in particular in the first case, in which the experimental MED value is negative while the theoretical value is positive, with a difference of $\approx$ 230 keV. Unlike the previous cases, MED have a larger magnitude. From the contributions panel, clearly emerges how the multipole term plus the single-particle corrections term dominate, but it can also be noticed how the V_B and V_{Cr} terms modulate the final MED values. Furthermore, the behaviour of V_B and V_{Cr} terms is the same for lower spin , then they tend to behave in the opposite way. Another fact that can be observed is that from the state 2$^+$ on, V_B and ΔE_{ll+ls} manifest the same trend, similarly to what happens for V_{CM} and V_{Cr} from the state 3$^+$. In addition, a positive MED value is predicted at 6$^+$.

J^π	$E_{exp^{26}\text{Si}}$	$E_{exp^{26}\text{Mg}}$	E_{th}	MED_{exp}	MED_{th}	ΔV_{CM}	ΔE_{ll+ls}	ΔV_{Cr}	ΔV_B
0^+	0	0	0	0	0	0	0	0	0
2^+	1797	1809	1938	-11	5	42	15	-19	-33
3^+	3758	3942	3898	-184	42	-28	68	-13	15
4^+	4446	4319	4402	127	118	109	41	6	-39
5^+	7198	6978	7058	220	49	0	78	-25	-4
6^+	\	8201	8120	\	81	88	49	-14	-30

Table 4.13: Experimental data and theoretical calculations for the ^{26}Si and ^{26}Mg. Idem as in Tab.4.1.

A=28 Regarding the mirror couple ^{28}P and ^{28}Al, the theoretical model fails in trend prediction, as shown in Fig.4.15. This is mainly due to the Coulomb multipole term and the single-particle corrections, observe the Tab.4.14, which dominate over the isospin-breaking and radial terms. The latter vary around the null value, reflecting a small occupancy in the $s_{\frac{1}{2}}$ orbit and so a nearly constant radius. As in the ^{26}Si$-^{26}$Mg case, MED present a large magnitude.

J^π	$E_{exp^{28}\text{P}}$	$E_{exp^{28}\text{Al}}$	E_{th}	MED_{exp}	MED_{th}	ΔV_{CM}	ΔE_{ll+ls}	ΔV_{Cr}	ΔV_B
3^+	0	0	0	0	0	0	0	0	0
4^+	2216	2272	2118	-56	26	16	12	3	-5
5^+	2483	2582	2480	-99	110	43	95	-9	-19

Table 4.14: Experimental data and theoretical calculations for the ^{28}P and ^{28}Al. Idem as in Tab.4.1.

A=30 Observing the upper panel of the ^{30}S and ^{30}Si couple in Fig.4.16, one can see how the theoretical model follows the experimental data. It can be noticed, from the contributions in

Tab.4.15, how the isospin-breaking term plays a crucial role in determining the final theoretical MED, especially for lower spin states, where the V_{Cr} and ΔE_{ll+ls} terms are quasi-negligible. Then, for higher spin the radial contribution becomes relevant, due to a larger $s_{\frac{1}{2}}$ orbit occupancy, together with the Coulomb multipole term, bringing the MED to negative values. The discrepancy at high spin states is captured by the shift of ≈ 100 keV among the experimental and theoretical trend.

J^π	$E_{exp^{30}S}$	$E_{exp^{30}Si}$	E_{th}	MED_{exp}	MED_{th}	ΔV_{CM}	ΔE_{ll+ls}	ΔV_{Cr}	ΔV_B
0^+	0	0	0	0	0	0	0	0	0
2^+	2210	2235	2295	-25	2	-26	2	0.4	26
3^+	4688	4831	4863	-143	-34	-33	-1	-23	24
4^+	5132	5279	5315	-147	-28	-25	-7	-10	14

Table 4.15: Experimental data and theoretical calculations for the ^{30}S and ^{30}Si. Idem as in Tab.4.1.

A=32 In contrast to the previous case, for the mirror pair ^{32}Cl and ^{32}P the model fails at the 2^+ spin states, while reproduces very well states at higher spin, as is evident from Fig.4.17. The calculations, reported in Tab.4.16 fail in the estimation values at 2^+ state: this mainly comes from the V_{CM}, ΔE_{ll+ls} and V_{Cr} terms. Then, in the higher spin states $(3^+, 5^+)$ the behaviour of the single-particle corrections on one side and that of the radial and isospin-breaking terms is reversed. This case shows an interesting interplay of contributions. The crossing trend of the different terms reproduces the non-monotonic shape of MED, being the difference between the model and the observations is smaller than 5 keV. Moreover, at 4+ a negative value MED is predicted by calculations.

J^π	$E_{exp^{32}Cl}$	$E_{exp^{32}P}$	E_{th}	MED_{exp}	MED_{th}	ΔV_{CM}	ΔE_{ll+ls}	ΔV_{Cr}	ΔV_B
1^+	0	0	0	0	0	0	0	0	0
2^+	90	78	177	12	-16	-2	-5	-11	2
3^+	1737	1755	1832	-18	-18	-21	-27	10	20
4^+	\	3149	3219	\	-17	-26	-33	24	18
5^+	4757	4743	4741	14	11	5	23	-17	-0,4

Table 4.16: Experimental data and theoretical calculations for the ^{32}Cl and ^{32}P. Idem as in Tab.4.1.

A=34 In the mirror couple ^{34}Ar and ^{34}S, as shown in Fig.4.18 the model captures the full experimental MED trend. It is interesting to notice from Tab.4.17 how the radial and ISB terms have the opposite behaviour to the others. The interplay of the various contributions is essential for achieving the alignment between the experimental and theoretical trends.

J^π	$E_{exp^{34}Ar}$	$E_{exp^{34}S}$	E_{th}	MED_{exp}	MED_{th}	ΔV_{CM}	ΔE_{ll+ls}	ΔV_{Cr}	ΔV_B
0^+	0	0	0	0	0	0	0	0	0
2^+	2091	2128	2106	-36	-13	-25	-18	14	16
4^+	4644	4689	4807	-45	-11	-4	-21	11	4

Table 4.17: Experimental data and theoretical calculations for the ^{34}Ar and ^{34}S. Idem as in Tab.4.1.

4.1.4 Comment on $T = 1$

For $T = 1$ positive-parity states in the sd-shell, the shell model generally reproduces the qualitative MED trends, with the radial term and Coulomb multipole providing the main contributions and isospin-breaking terms giving smaller adjustments. The agreement is good in lighter and heavier systems ($A = 20, 24, 30$–34), but in mid-shell nuclei ($A = 22, 26, 28$) the model shows larger deviations, sometimes even predicting the wrong sign. Overall, the essential physics is well captured, though limitations appear where cross-shell mixing and configuration dependence are strongest.
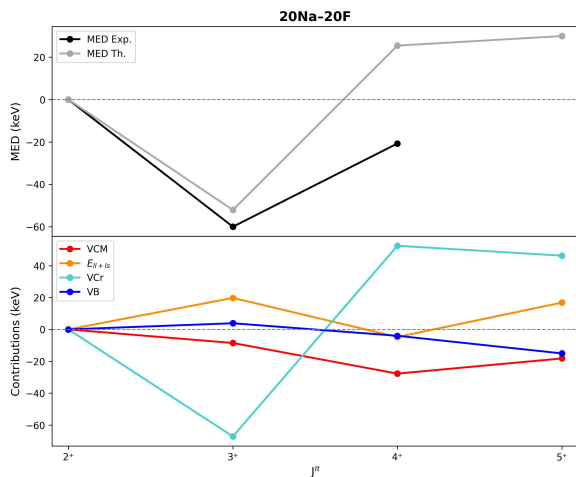

Figure 4.11: **Top panel:** the experimental MED values and theoretical predictions for the ^{20}Na and ^{20}F mirror pair. **Bottom panel:** the different contributions to the theoretical prediction.
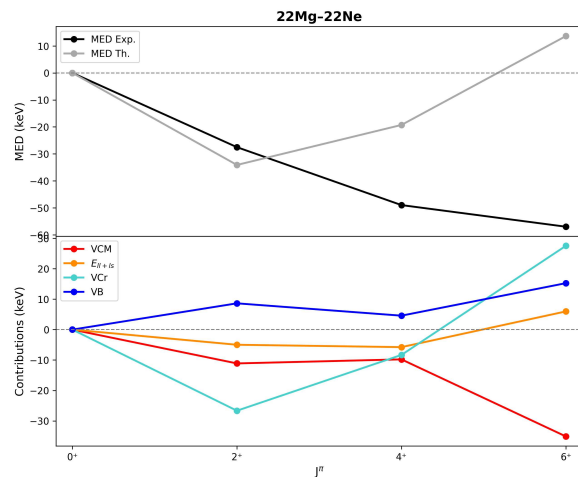

Figure 4.12: **Top panel:** the experimental MED values and theoretical predictions for the ^{22}Mg and ^{22}Ne mirror pair. **Bottom panel:** the different contributions to the theoretical prediction.

Figure 4.13: **Top panel:** the experimental MED values and theoretical predictions for the ^{24}Al and ^{24}Na mirror pair. **Bottom panel:** the different contributions to the theoretical prediction.

Figure 4.14: **Top panel:** the experimental MED values and theoretical predictions for the ^{26}Si and ^{26}Mg mirror pair. **Bottom panel:** the different contributions to the theoretical prediction.
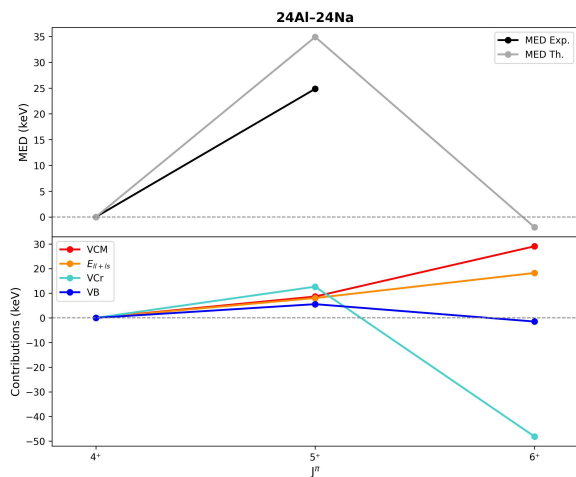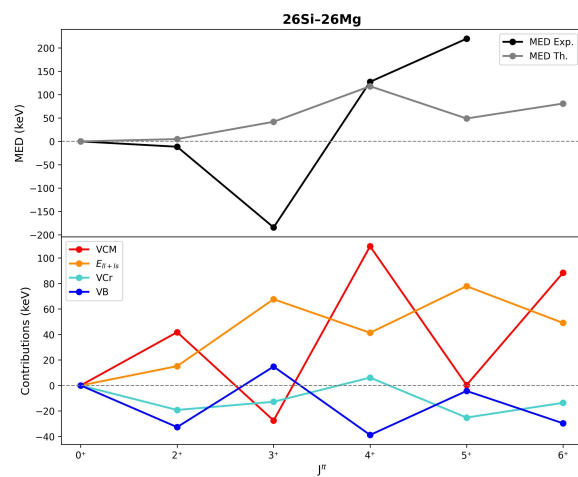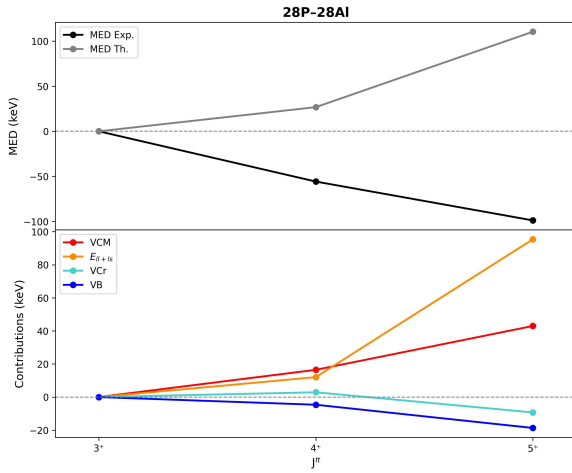
Figure 4.15: **Top panel:** the experimental MED values and theoretical predictions for the ^{28}P and ^{28}Al mirror pair. **Bottom panel:** the different contributions to the theoretical prediction.

Figure 4.16: **Top panel:** the experimental MED values and theoretical predictions for the ^{30}S and ^{30}Si mirror pair. **Bottom panel:** the different contributions to the theoretical prediction.

Figure 4.17: **Top panel:** the experimental MED values and theoretical predictions for the ^{32}Cl and ^{32}P mirror pair. **Bottom panel:** the different contributions to the theoretical prediction.
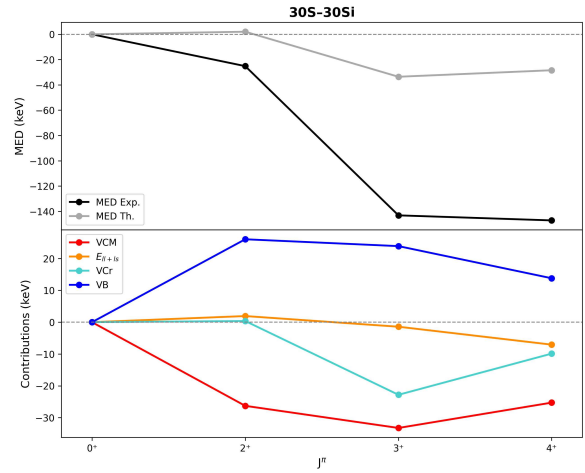

Figure 4.18: **Top panel:** the experimental MED values and theoretical predictions for the ^{34}Ar and ^{34}S mirror pair. **Bottom panel:** the different contributions to the theoretical prediction.
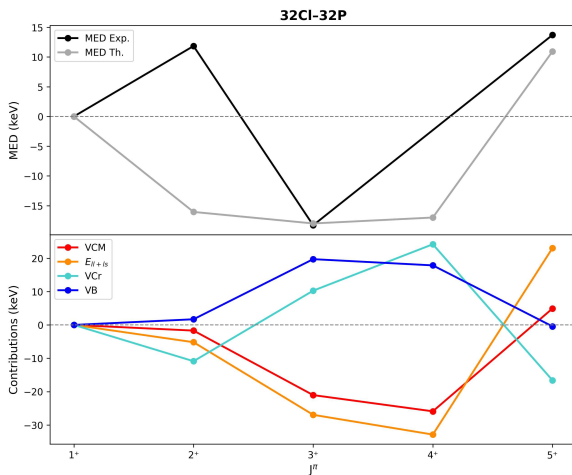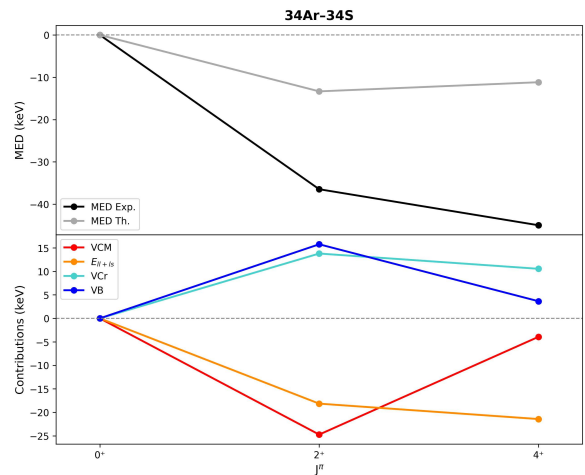
4.1.5   Mirror nuclei with $T = \frac{3}{2}$

In this context, the net difference $N - Z = 3$ indicates that within a mirror pair, one nucleus exhibits an excess of three protons, while the other one has an excess of three neutrons, as illustrated in Table (A.3). Moreover, this characteristic renders the analysed nuclei particularly significant due to their association with the driplines.

A=21   As one can see from the Fig.4.19, the theoretical calculations regarding the couple ^{21}Mg $-^{21}$F, reproduce the trend of the experimental data, but with a light underestimation at $\frac{9}{2}^+$. The total MED contributions, see the Tab.4.18, are mainly driven by the multipole term, whereas the isospin-breaking one tends to the opposite direction, towards positive values (≈ 40 keV). The radial term, as long as the single-particle corrections are quasi-negligible. The small values of V_{Cr} suggest a little occupation of the $s_{\frac{1}{2}}$ orbit. The term V_{CM} is characterised by the realignment of a couple of protons in ^{21}Mg and a couple of neutrons in ^{21}F.

J^π	$E_{exp^{21}\mathrm{Mg}}$	$E_{exp^{21}\mathrm{F}}$	E_{th}	MED_{exp}	MED_{th}	ΔV_{CM}	ΔE_{ll+ls}	ΔV_{Cr}	ΔV_B
$5/2^+$	0	0	0	0	0	0	0	0	0
$9/2^+$	1672	1755	1730	-83	-34	-75	-2	-4	47

Table 4.18: Experimental data and theoretical calculations for the ^{21}Mg and ^{21}F. Idem as in Tab.4.1.

A=23   For the mirror pair ^{23}Al and ^{23}Ne, the adopted method finely reproduces the data with a discrepancy between the theory and the observations of about 5 keV, see Fig.4.20. What is interesting is the comparison of the various contributions, reported in the Tab.4.19, with respect the the previous case. Now, the main term is the radial one, whereas V_B, V_{CM}, and ΔE_{ll+ls} tend to cancel the effect of each other. The greater V_{Cr} value reflects a larger occupancy in the $s_{\frac{1}{2}}$. The result is the excellent match between theory and experiment, underlying how all the terms are crucial to furnish a correct result.

J^π	$E_{exp^{23}\mathrm{Al}}$	$E_{exp^{23}\mathrm{Ne}}$	E_{th}	MED_{exp}	MED_{th}	ΔV_{CM}	ΔE_{ll+ls}	ΔV_{Cr}	ΔV_B
$5/2^+$	0	0	0	0	0	0	0	0	0
$7/2^+$	1619	1702	1817	-83	-88	17	6	-93	-18

Table 4.19: Experimental data and theoretical calculations for the ^{23}Al and ^{23}Ne. Idem as in Tab.4.1.

A=25   For what concerns the ^{25}Si and ^{25}Na mirrors, as is apparent from the Fig.4.21, the theoretical MED does not follow the experimental behaviour: it actually turns positive for $\frac{9}{2}^+$ (≈ 20 keV), deviating from the experimental data (≈ -55 keV). This poor agreement with experiment, both in sign and magnitude, is caused by the dominant Coulomb multipole and single-particle correction terms. The calculation fails to capture the correct pattern, as reported in the Tab.4.20.

J^π	$E_{exp^{25}\mathrm{Si}}$	$E_{exp^{25}\mathrm{Na}}$	E_{th}	$\mathrm{MED_{exp}}$	$\mathrm{MED_{th}}$	ΔV_{CM}	$\Delta E_{\mathrm{ll+ls}}$	ΔV_{Cr}	ΔV_B
$5/2^+$	0	0	0	0	0	0	0	0	0
$9/2^+$	2365	2419	2522	-54	24	32	28	-26	-10

Table 4.20: Experimental data and theoretical calculations for the ^{25}Si and ^{25}Na. Idem as in Tab.4.1.

A=27   In the case of the mirror nuclei ^{27}Mg and ^{27}P, as shown in the Fig.4.22, the theoretical calculations reproduce correctly the experimental trend, but there is mismatch going towards higher spin states $\frac{5}{2}^+$ of about 120 keV. In this case, the MED$_{th}$ values present a greater magnitude in comparison to the previous cases. The theoretical estimation, as can be seen from the Tab.4.21, is strongly influenced by the multipole and single-particle correction terms for higher spin states, while the radial term is fundamental for the $\frac{3}{2}^+$ state giving a positive contribution of ≈ 130 keV and together with the isospin-breaking term low the MED value at $\frac{5}{2}^+$. The large difference in the V_{Cr} term from $\frac{3}{2}^+$ to $\frac{5}{2}^+$ underlines the increasing occupancy in the $s_{\frac{1}{2}}$ orbit. Finally, two positive MED are predicted for the excited states at $\frac{7}{2}^+$ and $\frac{9}{2}^+$.

J^π	$E_{exp^{27}\mathrm{Mg}}$	$E_{exp^{27}\mathrm{P}}$	E_{th}	$\mathrm{MED_{exp}}$	$\mathrm{MED_{th}}$	ΔV_{CM}	$\Delta E_{\mathrm{ll+ls}}$	ΔV_{Cr}	ΔV_B
$1/2^+$	0	0	0	0	0	0	0	0	0
$3/2^+$	1120	985	971	135	177	28	33	131	-15
$5/2^+$	1569	1699	1661	-130	8	52	83	-92	-34
$7/2^+$	\	3110	3030	\	112	70	132	-60	-31
$9/2^+$	\	4399	4019	\	75	119	54	-50	-49

Table 4.21: Experimental data and theoretical calculations for the ^{27}Mg and ^{27}P. Idem as in Tab.4.1.

A=29   For the couple ^{29}S and ^{29}Al, the theoretical calculations, as is evident from the Fig.4.23, are in line with the observed data. From the contributions reported in the Tab.4.22, only the isospin-breaking and the multipole terms are decisive to determine the final theoretical calculations for lower spin states, while the radial term and the ΔE_{ll+ls} contribution have a very limited role. In conclusion, a positive and a negative MED values are calculated respectively for the excited states $\frac{9}{2}^+$ and $\frac{11}{2}^+$.

J^π	$E_{exp^{29}\mathrm{S}}$	$E_{exp^{29}\mathrm{Al}}$	E_{th}	$\mathrm{MED_{exp}}$	$\mathrm{MED_{th}}$	ΔV_{CM}	$\Delta E_{\mathrm{ll+ls}}$	ΔV_{Cr}	ΔV_B
$5/2^+$	0	0	0	0	0	0	0	0	0
$7/2^+$	1727	1754	1853	-27	-10	-28	-7	-2	27
$9/2^+$	\	3578	3542	\	17	-42	14	6	38
$11/2^+$	\	5855	5856	\	-24	-39	75	-74	14

Table 4.22: Experimental data and theoretical calculations for the ^{29}S and ^{29}Al. Idem as in Tab.4.1.

A=31   In the case of the mirror pair ^{31}Cl and ^{31}Si, the theoretical trend describes well the experimental data, as can be seen from the Fig.4.24 and almost all the contributions follows the same behaviour, see Tab.4.23. The small discrepancy can be imputed to the Coulomb multipole contribution, which reduces the final result. Moreover, a negative MED value is predicted at $\frac{7}{2}^+$, characterised by the V_{Cr} term.

J^π	$E_{exp^{31}Cl}$	$E_{exp^{31}Si}$	E_{th}	MED_{exp}	MED_{th}	ΔV_{CM}	ΔE_{ll+ls}	ΔV_{Cr}	ΔV_B
$3/2^+$	0	0	0	0	0	0	0	0	0
$5/2^+$	1728	1695	1603	33	49	-11	24	16	19
$7/2^+$	\	3874	3894	\	-77	-1	-27	-42	-7

Table 4.23: Experimental data and theoretical calculations for the ^{31}Cl and ^{31}Si. Idem as in Tab.4.1.

A=33 Regarding the mirror couple ^{33}Ar and ^{33}P, the staggering experimental trend is not followed by the theoretical model, with a sensitive difference in magnitude (≈ 60 keV) in the $\frac{3}{2}^+$ state. As can be seen from the lower panel in the Fig.4.25, the isospin-breaking and the radial terms are positive, this tends to deviate from a correct prediction in the $\frac{3}{2}^+$ state. Then, the interplay between the different terms allows to bring the theoretical estimate closer to the experimental evidence for the $\frac{5}{2}^+$ state, see Tab.4.24 for the numerical results.

J^π	$E_{exp^{33}Ar}$	$E_{exp^{33}P}$	E_{th}	MED_{exp}	MED_{th}	ΔV_{CM}	ΔE_{ll+ls}	ΔV_{Cr}	ΔV_B
$1/2^+$	0	0	0	0	0	0	0	0	0
$3/2^+$	1359	1432	1441	-73	-10	-32	-42	45	18
$5/2^+$	1798	1848	2027	-50	-23	-49	-15	-7	48

Table 4.24: Experimental data and theoretical calculations for the ^{33}Ar and ^{33}P. Idem as in Tab.4.1.

4.1.6 Comment on $T = \frac{3}{2}$

The MED systematics for $T = 3/2$ mirrors are generally smoother and more regular than in the $T = 1/2$ case. Experimental trends typically show monotonic variations with spin, such as the clear decrease in $A = 21$ and $A = 23$, or modest increases in $A = 31$, and these are largely well reproduced by theory. The main drivers are the Coulomb multipole and spin–orbit corrections, with the radial term becoming important in nuclei with significant $s_{1/2}$ occupation (e.g., $A = 23$, $A = 27$). Deviations remain moderate, usually within a few tens of keV, though certain cases (e.g., $A = 25$) show failure in both sign and magnitude. Overall, the theory is consistent, capturing the balance of the different contributions, with discrepancies highlighting sensitivity to changeling of nuclear structures for higher spin states.
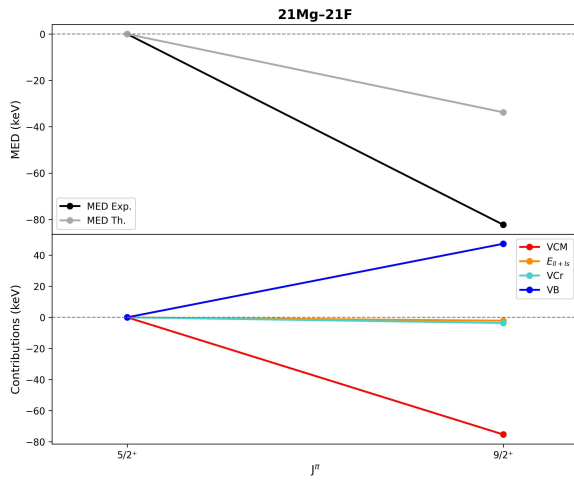
Figure 4.19: **Top panel:** the experimental MED values and theoretical predictions for the ^{21}Mg and ^{21}F mirror pair. **Bottom panel:** the different contributions to the theoretical prediction.
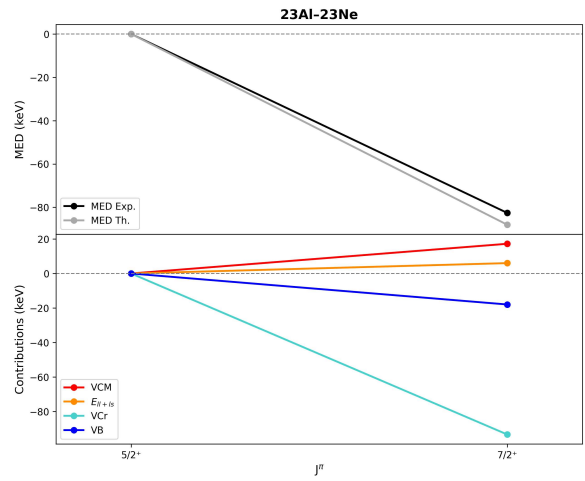

Figure 4.20: **Top panel:** the experimental MED values and theoretical predictions for the ^{23}Al and ^{23}Ne mirror pair. **Bottom panel:** the different contributions to the theoretical prediction.
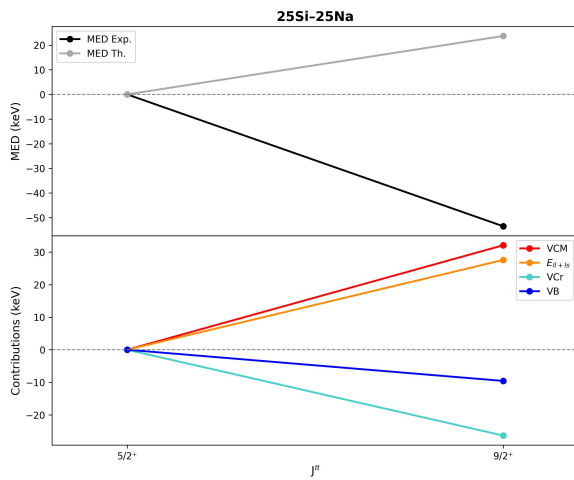

Figure 4.21: **Top panel:** the experimental MED values and theoretical predictions for the ^{25}Si and ^{25}Na mirror pair. **Bottom panel:** the different contributions to the theoretical prediction.
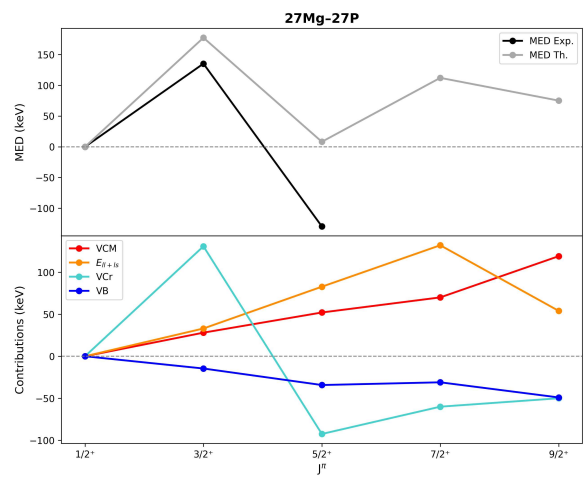

Figure 4.22: **Top panel:** the experimental MED values and theoretical predictions for the ^{27}Mg and ^{27}P mirror pair. **Bottom panel:** the different contributions to the theoretical prediction.
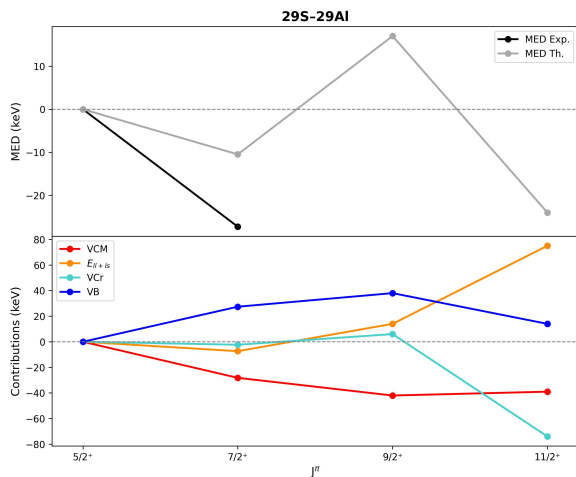
Figure 4.23: **Top panel:** the experimental MED values and theoretical predictions for the ^{29}S and ^{29}Al mirror pair. **Bottom panel:** the different contributions to the theoretical prediction.
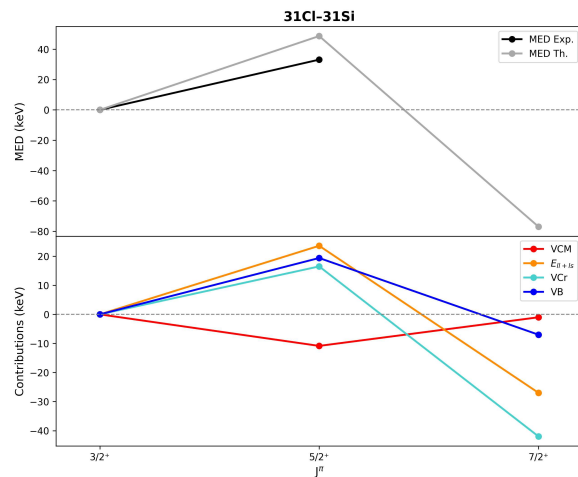

Figure 4.24: **Top panel:** the experimental MED values and theoretical predictions for the ^{31}Cl and ^{31}Si mirror pair. **Bottom panel:** the different contributions to the theoretical prediction.
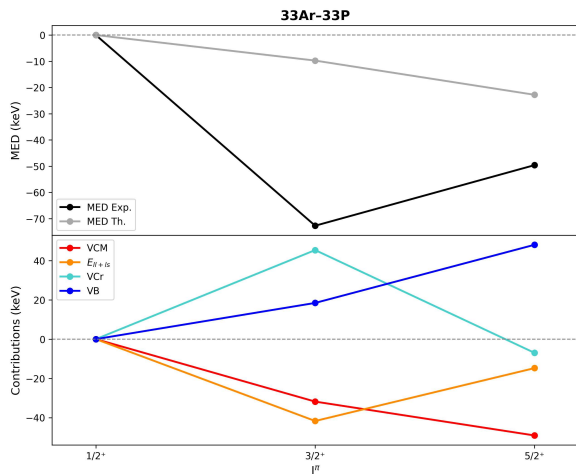

Figure 4.25: **Top panel:** the experimental MED values and theoretical predictions for the ^{33}Ar and ^{33}P mirror pair. **Bottom panel:** the different contributions to the theoretical prediction.

4.1.7   Mirror nuclei with $T = 2$

In this case, the overall disparity between protons and neutrons is $|N-Z| = 4$, so in a mirror pair there is a nucleus with an excess of four protons and the other has an excess of four neutrons. This sharp difference in the $N - Z$ number makes the proton-rich nuclei very unstable and difficult to analyse experimentally due to their short life, this is the cause of the poverty of available data in this dripline region.

A=24   Observing the Tab.4.25 of the ^{24}Si and ^{24}Ne mirror couple, the theoretical calculations correctly reproduce the trend of the experimental data, with a little difference at 2^+. As can be noted from the contributions panel in the Fig.4.26, it is clear how the radial (due to a strong $s_{\frac{1}{2}}$ occupancy) and isospin-term are decisive for a negative result, while the positive V_{CM} and ΔE_{ll+ls} terms are the cause of the failure in magnitude estimation. Furthermore, a positive MED value is predicted at 4^+.

J^π	$E_{exp}{}^{24}\text{Si}$	$E_{exp}{}^{24}\text{Ne}$	E_{th}	MED_{exp}	MED_{th}	ΔV_{CM}	$\Delta E_{\text{ll+ls}}$	ΔV_{Cr}	ΔV_B
0^+	0	0	0	0	0	0	0	0	0
2^+	1872	1982	2181	-110	-54	33	39	-106	-19
4^+	\	3963	4060	\	45	70	-5	23	-43

Table 4.25: Experimental data and theoretical calculations for the ^{24}Si and ^{24}Ne. Idem as in Tab.4.1.

A=28   As reported by the Tab.4.26 of the mirror nuclei ^{28}S and ^{28}Mg, the calculations present an overestimation of (≈ 40 keV) in the state 4^+. This can be seen from the lower panel in the Fig.4.27. The Coulomb multipole and single-particle correction terms tend to increase with spin, while the radial term has an opposite trend at higher spin, caused by a rising $s_{\frac{1}{2}}$ orbit occupation. The isospin-breaking term, being negative, mitigates the difference in the final results. In addition, a positive higher MED value is predicted at 6^+.

J^π	$E_{exp}{}^{28}\text{S}$	$E_{exp}{}^{28}\text{Mg}$	E_{th}	MED_{exp}	MED_{th}	ΔV_{CM}	$\Delta E_{\text{ll+ls}}$	ΔV_{Cr}	ΔV_B
0^+	0	0	0	0	0	0	0	0	0
2^+	1507	1474	1527	33	42	14	10	27	-10
4^+	4040	4021	4200	19	60	47	22	11	-20
6^+	\	7931	7955	\	127	59	68	9	-9

Table 4.26: Experimental data and theoretical calculations for the ^{28}S and ^{28}Mg. Idem as in Tab.4.1.

A=32   In the case of the ^{32}Ar and ^{32}Si couple, the theory correctly predicts the sign and general scale, as is clear from the data in the Tab.4.27. The panels in the Fig.4.28 confirm the return of negative MED after the inversion behaviour at $A = 28$. A negative MED value is predicted at 4^+, characterised by the radial term.

J^π	$E_{exp}{}^{32}\text{Ar}$	$E_{exp}{}^{32}\text{Si}$	E_{th}	MED_{exp}	MED_{th}	ΔV_{CM}	$\Delta E_{\text{ll+ls}}$	ΔV_{Cr}	ΔV_B
0^+	0	0	0	0	0	0	0	0	0
2^+	1867	1941	2136	-74	-57	-38	-14	-37	32
4^+	\	5881	6091	\	-160	-54	83	-219	30

Table 4.27: Experimental data and theoretical calculations for the ^{32}Ar and ^{32}Si. Idem as in Tab.4.1.

A=34   Regarding the mirrors ^{34}K and ^{34}P, calculations correctly predict the sign and general scale, see the Tab.4.28. This pattern confirms the persistence of negative MED for lower spin states in proton-rich $T = 2$ nuclei. As can be seen from the Fig.4.29, in this case all the

contributions are negative, capturing the right final trend. Moreover, a negative MED value is predicted at 3^+.

J^π	$E_{exp^{34}\mathrm{K}}$	$E_{exp^{34}\mathrm{P}}$	$\mathrm{E_{th}}$	$\mathrm{MED_{exp}}$	$\mathrm{MED_{th}}$	ΔV_{CM}	$\Delta E_{\mathrm{ll+ls}}$	ΔV_{Cr}	ΔV_B
1^+	0	0	0	0	0	0	0	0	0
2^+	401	429	280	-28	-20	-4	-10	-5	-1
3^+	\	2676	2713	\	-23	-17	-80	77	-3

Table 4.28: Experimental data and theoretical calculations for the ^{34}K and ^{34}P. Idem as in Tab.4.1.

4.1.8   Comment on $T = 2$

For $T = 2$ mirror nuclei, the MED behaviour is more systematic. Experimental MED vary smoothly with spin, and the shell model reproduces both trend and magnitude reasonably well, with typical deviations of 10–50 keV. Failures mainly occur in $A = 24$, where theory underestimates experiment at higher spin. In summary, the model is effective for $T = 2$ mirrors, with good predictive power except in the analysed cases.
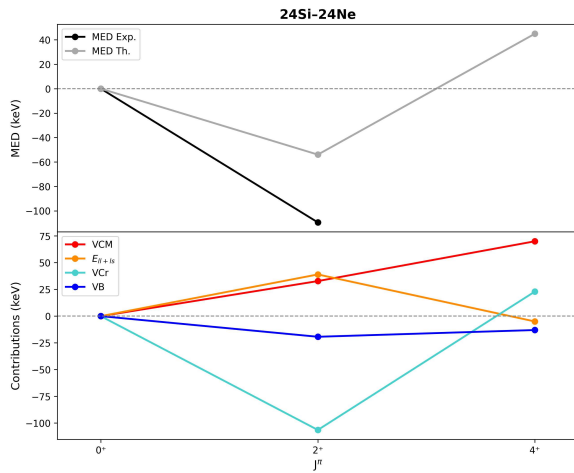
Figure 4.26: **Top panel:** the experimental MED values and theoretical predictions for the ^{24}Si and ^{24}Ne mirror pair. **Bottom panel:** the different contributions to the theoretical prediction.
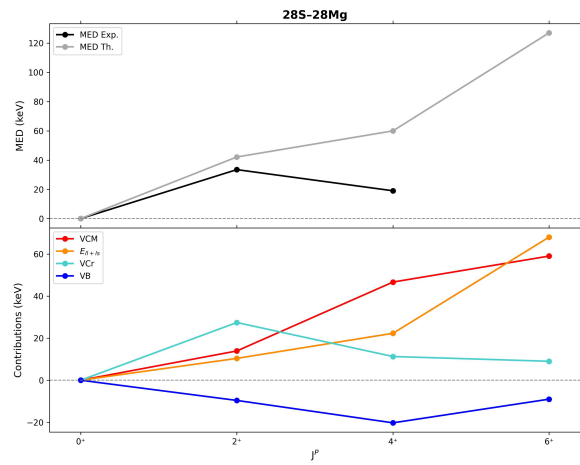

Figure 4.27: **Top panel:** the experimental MED values and theoretical predictions for the ^{28}S and ^{28}Mg mirror pair. **Bottom panel:** the different contributions to the theoretical prediction.
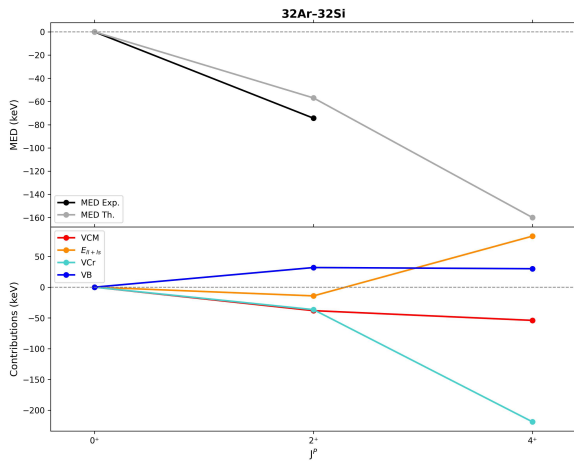

Figure 4.28: **Top panel:** the experimental MED values and theoretical predictions for the ^{32}Ar and ^{32}Si mirror pair. **Bottom panel:** the different contributions to the theoretical prediction.
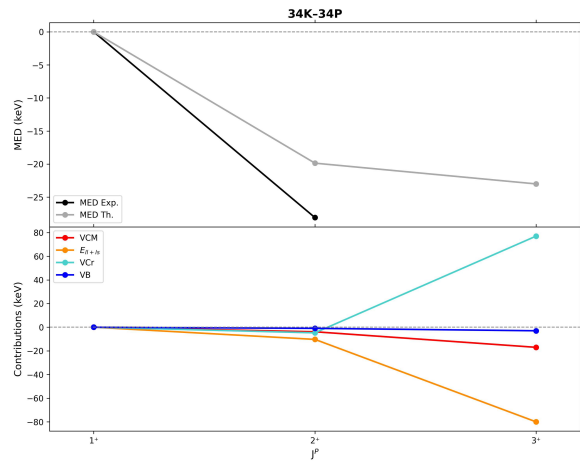

Figure 4.29: **Top panel:** the experimental MED values and theoretical predictions for the ^{34}K and ^{34}P mirror pair. **Bottom panel:** the different contributions to the theoretical prediction.

4.2 Final comment on Positive parity states

Across the sd-shell, MED in mirror nuclei with $T = \frac{1}{2}, 1, \frac{3}{2}, 2$ are largely explained by the interplay of Coulomb monopole and multipole terms, spin–orbit corrections, and isospin-breaking contributions. The theory reproduces the main trends: staggering or not monotonic spin-sensitive behaviour in odd-A, $T = \frac{1}{2}$ mirrors; good agreement in lighter and heavier $T = 1$ systems but failures in mid-shell nuclei; smooth, accurately reproduced patterns in $T = \frac{3}{2}$ mirrors; and systematic, accurate reproduction in $T = 2$ cases. Discrepancies are typically tens of keV but can reach about 100 keV at higher spin or in mid-shell masses. The main limitation is the restricted valence space of the effective interaction, which constrains the treatment of cross-shell excitations, especially at higher spins.

4.3 Negative parity states

Following the same approach used for positive parity states, a detailed overview of the MED for negative parity yrast states is provided here, followed by a general comparison of the results. As said, only states with the unnatural negative parity in the sd-shell will be analysed. Recall that the effective interaction used is the PSDPF [9], in order to permit particle promotions from lower to higher shells (cross shell excitations), having in this way negative parity states. Hence, in this part:

- the **core** is $^{4}_{2}He_{2}$;

- the **valence space** given by the p-shell, the sd-shell and the fp-shell, spanned by the orbits $(1p_{\frac{1}{2}}, 1d_{\frac{5}{2}}, 2s_{\frac{1}{2}}, 1d_{\frac{3}{2}}, 1f_{\frac{7}{2}}, 2p_{\frac{3}{2}}, 1f_{\frac{5}{2}}, 2p_{\frac{1}{2}})$.

Since the negative parity states are intruder states, the lowest yrast state is not the ground state[3] of the analysed nucleus. To account for this, the collected experimental energies were normalised by setting the lowest negative parity yrast state to zero and rescaling those with increasing J. In the following tables, those normalised experimental MED are reported as $\text{MED}^{Norm.}_{exp}$.

4.3.1 Mirror nuclei with $T = \frac{1}{2}$

The net difference $|N - Z| = 1$, so in a mirror pair there is a nucleus with an excess of a proton and the other one has an excess of a neutron; see the Tab. A.2[4].

A=19 Regarding the mirror couple ^{19}Ne$-^{19}$F, as can be seen from Fig.4.30, the theoretical calculations reproduce the trend of the experimental data quite faithfully, with an erroneous prevision in the sign of the state $\frac{7}{2}^{-}$ only. The results of the model, reported in the Tab.4.29, highlight the role of the radial term in the final MED overestimation. This is due to the decreasing in the $s_{\frac{1}{2}}$ orbit occupation. Finally, it is possible to conclude, despite the light discrepancy of about ≈ 20 keV, that the model works fine.

---

[3]In the sd-shell, the ground states obviously have positive parity.
[4]The states studied for both parities, positive and negative, are shown in bold.

J^π	$E_{exp^{19}Ne}$	$E_{exp^{19}F}$	E_{th}	MED_{exp}	$MED_{exp}^{Norm.}$	MED_{th}	ΔV_{CM}	ΔE_{ll+ls}	ΔV_{Cr}	ΔV_B
$1/2^-$	275	110	47	165	0	0	0	0	0	0
$5/2^-$	1508	1346	1590	162	-3	-3	-1	0.3	0.2	-2
$7/2^-$	4142	3999	4343	143	-22	2	-34	-24	46	15
$9/2^-$	4200	4033	4110	167	2	27	-12	-8	47	-0.4
$13/2^-$	8428	8288	8167	140	-25	-2	-72	-25	63	32

Table 4.29: Experimental data and theoretical calculations for the ^{19}Ne and ^{19}F. The table is structured in the following way: total angular momenta and the parity of the states; the experimental excitation energy E_{exp} [16]; the calculated energy E_{th}; the experimental and the normalised experimental MED; the theoretical MED; the Coulomb multipole term ΔV_{CM}, the single-particle corrections term ΔE_{ll+ls}, the radial term ΔV_{Cr} and the isospin-breaking term ΔV_B. All energies are given in keV.

A=21   In the ^{21}Na and ^{21}Ne case is very interesting, the theoretical calculations can reproduce the correct trend of the experimental data. The theoretical predictions overestimate the observed data, as shown in the Tab.4.30, but this difference becomes smaller moving towards higher spin states. By comparing the two panels in the Fig.4.31, one can see how the Coulomb multipole and single-particle correction terms dominate and have a staggering trend. This suggests that the configuration at these spins is particularly sensitive to proton-neutron asymmetries in the Coulomb field and the multipolar term. The isospin-breaking term oscillates and tends to moderate the MED values, being opposite in values with respect to the multipole term. The radial term is negligible, underlining a constant radial structure. A negative MED value is predicted at $\frac{9}{2}^-$.

J^π	$E_{exp^{21}Na}$	$E_{exp^{21}Ne}$	E_{th}	MED_{exp}	$MED_{exp}^{Norm.}$	MED_{th}	ΔV_{CM}	ΔE_{ll+ls}	ΔV_{Cr}	ΔV_B
$1/2^-$	2798	2789	2447	9	0	0	0	0	0	0
$3/2^-$	3679	3664	3326	15	6	42	29	23	-1	-8
$5/2^-$	3862	3884	3636	-22	-31	-9	-21	-3	-1	16
$7/2^-$	5815	5818	4652	-3	-12	-10	-24	17	-1	-3
$9/2^-$	\	6033	5546	\	\	-10	-31	2	-2	20

Table 4.30: Experimental data and theoretical calculations for the ^{21}Na and ^{21}Ne. Idem as in Tab.4.29.

A=23   For the mirrors ^{23}Mg–^{23}Na, the theoretical prediction correctly follows the experimental data, with a little trend discrepancy in the state $\frac{3}{2}^-$ as can be seen from Fig.4.32. As reported in the Tab.4.31, the principal contribution to the calculations is due to the multipole and single-particle correction terms, whose magnitude increases with angular momentum. This indicates a structural change evolving with J. The nearly null values of V_{Cr} confirm the small $s_{\frac{1}{2}}$ orbit occupation. The term V_B shows its largest amplitude at $\frac{7}{2}^-$, consistent with a shell evolution involving fp orbitals that are more spatially extended, increasing sensitivity to spin-orbit and multipole Coulomb effects.

J^π	$E_{exp^{23}\mathrm{Mg}}$	$E_{exp^{23}\mathrm{Na}}$	E_{th}	$\mathrm{MED_{exp}}$	$\mathrm{MED}_{exp}^{Norm.}$	$\mathrm{MED_{th}}$	ΔV_{CM}	ΔE_{ll+ls}	ΔV_{Cr}	ΔV_B
$1/2^-$	2771	2641	1929	131	0	0	0	0	0	0
$3/2^-$	3794	3678	3170	116	-15	-10	-8	-8	-0.02	6
$5/2^-$	3972	3848	3204	124	-7	-21	-11	-8	-1	-1
$7/2^-$	6129	6042	5502	87	-43	-61	-46	-31	-1	18
$9/2^-$	6448	6354	5659	93	-37	-68	-41	-27	-6	5

Table 4.31: Experimental data and theoretical calculations for the ^{23}Mg and ^{23}Na. Idem as in Tab.4.29.

A=25 In the case of ^{25}Al and ^{25}Mg, the experimental MED shows a strong positive value ≈ 75 keV at $\frac{7}{2}^-$, while the theoretical prediction is opposite ≈ -100 keV suggesting a clear discordance between the model and the data; see Fig.4.33. The only contributions that characterise the theoretical results obtained are the multipole and single-particle correction terms, as reported in the Tab.4.32. The almost null values of the isospin-breaking and radial terms imply that the core Coulomb field and radial corrections are not driving this discrepancy.

J^π	$E_{exp^{25}\mathrm{Al}}$	$E_{exp^{25}\mathrm{Mg}}$	E_{th}	$\mathrm{MED_{exp}}$	$\mathrm{MED}_{exp}^{Norm.}$	$\mathrm{MED_{th}}$	ΔV_{CM}	ΔE_{ll+ls}	ΔV_{Cr}	ΔV_B
$3/2^-$	3062	3413	3767	-351	0	0	0	0	0	0
$7/2^-$	3696	3971	3946	-275	76	-99	-57	-41	-0.1	-0.004

Table 4.32: Experimental data and theoretical calculations for the ^{25}Al and ^{25}Mg. Idem as in Tab.4.29.

A=27 As can be noted from the Fig.4.34, the theoretical prediction for the mirrors ^{27}Si $-$ ^{27}Al systematically underestimates the experimental data. The experimental MED shows a clear monotonic decrease with spin, reaching very large negative values ($\approx$ -240 keV) at $\frac{9}{2}^-$. The theoretical curve captures the initial states from $\frac{1}{2}^-$ to $\frac{5}{2}^-$, then fails to reproduce the strong decrease observed at higher spin $\frac{7}{2}^-$ and $\frac{9}{2}^-$; see contributions reported in the Tab.4.33.

J^π	$E_{exp^{27}\mathrm{Si}}$	$E_{exp^{27}\mathrm{Al}}$	E_{th}	$\mathrm{MED_{exp}}$	$\mathrm{MED}_{exp}^{Norm.}$	$\mathrm{MED_{th}}$	ΔV_{CM}	ΔE_{ll+ls}	ΔV_{Cr}	ΔV_B
$1/2^-$	4138	4055	2155	83	0	0	0	0	0	0
$3/2^-$	5227	5156	3221	71	-12	-10	-12	-7	-4	12
$5/2^-$	5501	5438	3713	62	-21	-2	2	2	-5	-1
$7/2^-$	6389	6477	5710	-88	-172	-31	-32	-15	-4	21
$9/2^-$	7070	7227	6434	-157	-241	-5	-5	0.1	-3	3

Table 4.33: Experimental data and theoretical calculations for the ^{27}Si and ^{27}Al. Idem as in Tab.4.29.

A=31 In the ^{31}S and ^{31}P case, as suggested by the data reported in the Tab.4.34, the staggering behaviour of the experimental data is correctly reproduced by the model, despite a modest shift in the state $\frac{11}{2}^-$. As one can see from the contributions graph in the Fig.4.35, the multipole Coulomb term is modulated by the isospin-breaking term only, which increases with spin. The radial term is again negligible. This case is interesting because of the strong MED values and the interplay of cross-shell interaction from sd to fp shells.

J^π	$E_{exp^{31}S}$	$E_{exp^{31}P}$	E_{th}	MED_{exp}	$MED_{exp}^{Norm.}$	MED_{th}	ΔV_{CM}	ΔE_{ll+ls}	ΔV_{Cr}	ΔV_B
$7/2^-$	4450	4431	5659	19	0	0	0	0	0	0
$9/2^-$	6376	6501	7090	-126	-145	-157	-101	-59	-6	8
$11/2^-$	6833	6668	7836	165	146	-60	-62	-23	-4	28
$13/2^-$	8461	8705	9193	-244	-263	-316	-226	-122	-3	35

Table 4.34: Experimental data and theoretical calculations for the ^{31}S and ^{31}P. Idem as in Tab.4.29.

A=35 For the couple ^{35}Ar$-^{35}$Cl, the monotonic trend of the observed data is faithfully repro-duced by the model, except for the higher spin state at $\frac{13}{2}^-$, in which the overestimation is more evident (≈ 320 keV of difference), see the Fig.4.36. By looking at the Tab.4.35, ΔE_{ll+ls} and V_{CM} are the dominant terms, which explains most of the total MED. The other two contributions do not affect the final theoretical MED predictions.

J^π	$E_{exp^{35}Ar}$	$E_{exp^{35}Cl}$	E_{th}	MED_{exp}	$MED_{exp}^{Norm.}$	MED_{th}	ΔV_{CM}	ΔE_{ll+ls}	ΔV_{Cr}	ΔV_B
$7/2^-$	3197	3163	4307	34	0	0	0	0	0	0
$9/2^-$	4359	4348	5358	11	-23	-73	-33	-35	11	-17
$11/2^-$	5384	5407	6383	-23	-57	-96	-21	-67	13	-19
$13/2^-$	5766	6087	6675	-322	-356	-624	-399	-254	0.3	29

Table 4.35: Experimental data and theoretical calculations for the ^{35}Ar and ^{35}Cl. Idem as in Tab.4.29.

4.3.2 Comment on $T = \frac{1}{2}$

The analysis shows regular behaviour as for positive-parity states, reflecting the intruder nature of these excitations and the role of cross-shell mixing with the fp-shell. In lighter systems such as $A = 19$ and $A = 21$, the theoretical calculations reproduce the experimental MED trends reasonably well, with only modest discrepancies (on the order of 20–30 keV) and occasional sign mismatches in individual states. At $A = 23$ the model still follows the general evolution with spin, although contributions from multipole and single-particle terms dominate and highlight the sensitivity of these states to structural changes. Larger inconsistencies emerge at mid-shell: in $A = 25$ the theory fails, predicting opposite sign compared to experiment at the $7/2^-$ state, while for $A = 27$ it underestimates the steep experimental decrease of MED with spin. In heavier nuclei ($A = 31, 35$) the agreement improves again in capturing the staggering or monotonic trends, though deviations at high spin can reach several hundred keV. Overall, the results confirm that the shell model with cross-shell excitations captures the qualitative MED behaviour, but its quantitative reliability decreases at higher spins and in mid-shell nuclei.
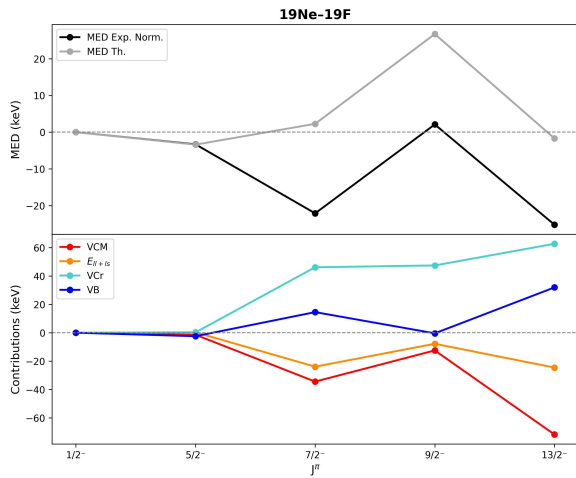
Figure 4.30: **Top panel:** the experimental MED values and theoretical predictions for the ^{19}Ne and ^{19}F mirror pair. **Bottom panel:** the different contributions to the theoretical prediction.
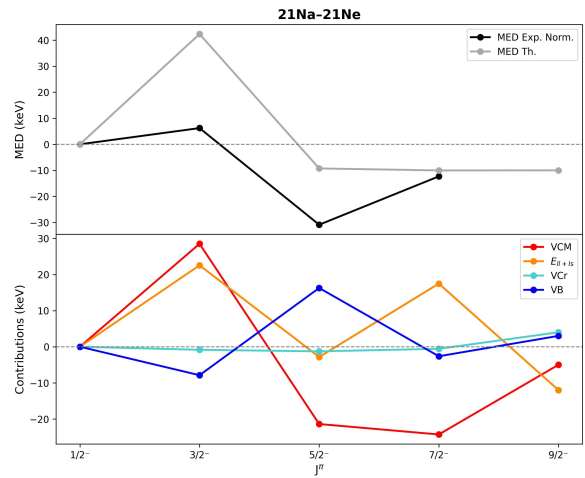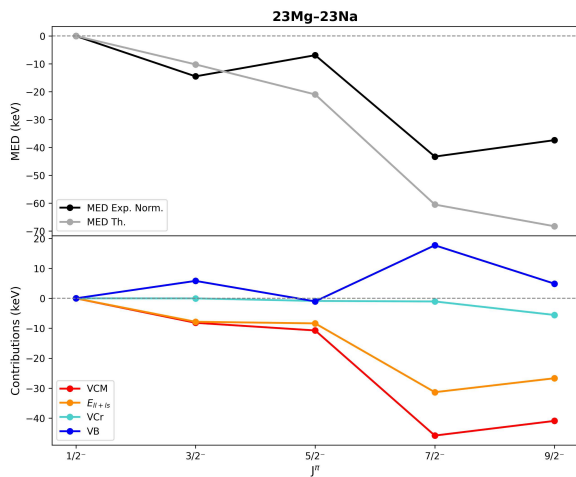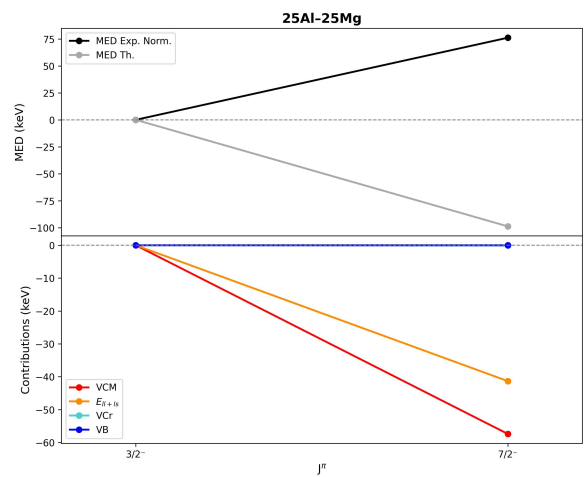

Figure 4.31: **Top panel:** the experimental MED values and theoretical predictions for the ^{21}Na and ^{21}Ne mirror pair. **Bottom panel:** the different contributions to the theoretical prediction.

Figure 4.32: **Top panel:** the experimental MED values and theoretical predictions for the ^{23}Mg and ^{23}Na mirror pair. **Bottom panel:** the different contributions to the theoretical prediction.

Figure 4.33: **Top panel:** the experimental MED values and theoretical predictions for the ^{25}Al and ^{25}Mg mirror pair. **Bottom panel:** the different contributions to the theoretical prediction.
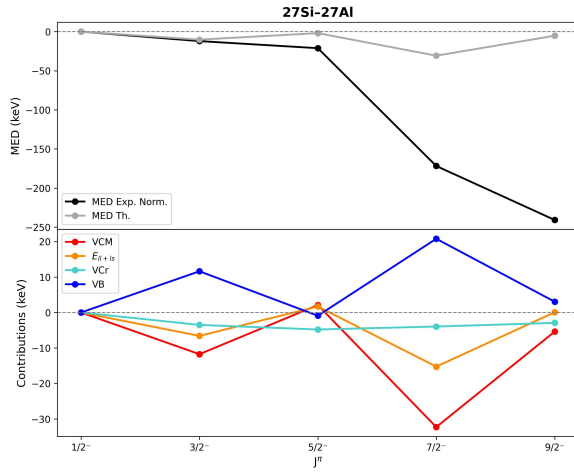
Figure 4.34: **Top panel:** the experimental MED values and theoretical predictions for the ^{27}Si and ^{27}Al mirror pair. **Bottom panel:** the different contributions to the theoretical prediction.
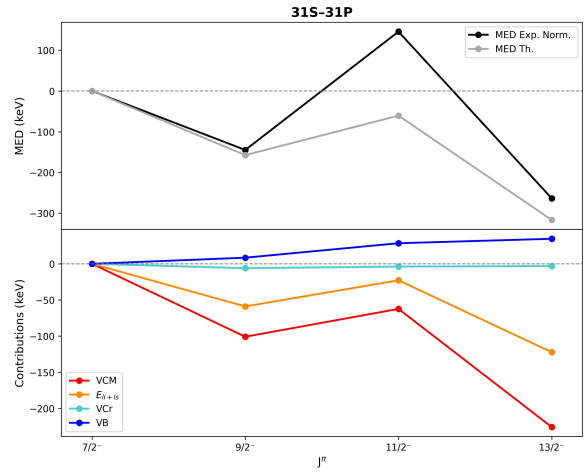

Figure 4.35: **Top panel:** the experimental MED values and theoretical predictions for the ^{31}S and ^{31}P mirror pair. **Bottom panel:** the different contributions to the theoretical prediction.
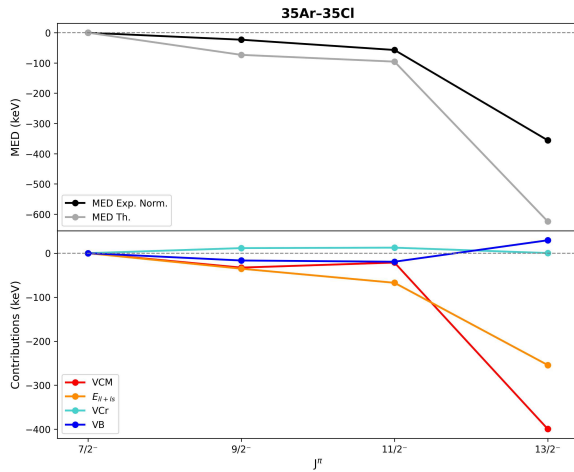

Figure 4.36: **Top panel:** the experimental MED values and theoretical predictions for the ^{35}Ar and ^{35}Cl mirror pair. **Bottom panel:** the different contributions to the theoretical prediction.

4.3.3 Mirror nuclei with $T = 1$

In this case, the absolute difference $N - Z = 2$, indicating that within a mirror pair, one nucleus has two extra protons, while the other one has an excess of contains two additional neutrons; see the Tab. A.2.

A=20 The ^{20}Na$-^{20}$F case is well reproduced by the theoretical model, as shown in the Fig.4.37. The main contributions, as reported in the Tab.4.36, are given by the positive values of the Coulomb multipole and single-particle corrections terms and the isospin-breaking negative term, which is the cause of the theoretical systematic underestimate. As already seen in the in the previous cases, the radial term is negligible. A positive MED value is calculated at 4^-.

J^π	$E_{exp^{20}\text{Na}}$	$E_{exp^{20}\text{F}}$	E_{th}	MED_{exp}	$\text{MED}_{exp}^{Norm.}$	MED_{th}	ΔV_{CM}	ΔE_{ll+ls}	ΔV_{Cr}	ΔV_B
1^-	\	984	1338	\	0	0	0	0	0	0
2^-	1346	1309	1394	37	37	25	15	17	0	-7
3^-	1992	1971	1822	21	21	18	15	15	2	-13
4^-	\	2968	3115	\	\	13	17	15	2	-20

Table 4.36: Experimental data and theoretical calculations for the ^{20}Na and ^{20}F. Idem as in Tab.4.29.

A=26 For mirrors ^{26}Si and ^{26}Mg, as illustrated in Fig.4.38, the magnitude of the MED returns to be large, as in heavier $T = \frac{1}{2}$ isobars. Looking at the Tab.4.37, the theoretical calculations capture the trend of the experimental data, but with an overestimation of ≈ 300 keV. This mismatch is due to the multipole and single-particle corrections terms, which are strongly negative. The isospin-breaking term is the only one that compensates a bit, but not enough to bridge the gap. In addition, two negative values MED are predicted at 4^- and 6^-.

J^π	$E_{exp^{26}\text{Si}}$	$E_{exp^{26}\text{Mg}}$	E_{th}	MED_{exp}	$\text{MED}_{exp}^{Norm.}$	MED_{th}	ΔV_{CM}	ΔE_{ll+ls}	ΔV_{Cr}	ΔV_B
3^-	6787	6876	6062	-89	0	0	0	0	0	0
4^-	\	7283	7510	\	\	-586	-535	-194	23	119
5^-	7522	7950	8015	-428	-339	-650	-578	-214	19	123
6^-	\	9169	9183	\	\	-700	-605	-230	18	118

Table 4.37: Experimental data and theoretical calculations for the ^{26}Si and ^{26}Mg. Idem as in Tab.4.29.

A=32 As can be seen from the Tab.4.38 of the pair ^{32}Cl $- ^{32}$P, the theoretical predictions present a monotonic negative trend, differently from the experimental data, which are negative in the state 4^-, but not in the spin state 3^-. This difference can be seen from the panels in the Fig.4.39, and its origin lies in the multipole and single-particle corrections terms, while V_B and V_{Cr} are negligible, being smaller even by a couple of orders of magnitude. Two other negative MED values are calculated for the excited states 5^- and 6^-.

J^π	$E_{exp^{32}Cl}$	$E_{exp^{32}P}$	E_{th}	MED_{exp}	$MED_{exp}^{Norm.}$	MED_{th}	ΔV_{CM}	ΔE_{ll+ls}	ΔV_{Cr}	ΔV_B
2^-	2932	3264	3218	-332	0	0	0	0	0	0
3^-	3164	3319	3638	-155	177	-187	-123	-75	3	8
4^-	3055	3445	3762	-391	-58	-228	-153	-84	-3	11
5^-	\	4275	4414	\	\	-263	-176	-117	10	20
6^-	\	5862	6082	\	\	-287	-191	-112	-5	21

Table 4.38: Experimental data and theoretical calculations for the ^{32}Cl and ^{32}P. Idem as in Tab.4.29.

A=34 From a synoptic comparison between the Fig.4.40 and the Fig.4.38 emerges how the mirror couple ^{34}Ar$-^{34}$S case is very similar to the $A = 26$ previously analysed. So, there is a systematic overestimation of ≈ 130 keV of the model with respect to the observed data reported in the Tab.4.39. This comes again from the sharp difference in magnitude between the multipole and single-particle terms and the V_B and V_{Cr} terms, which are positive. Moreover, a negative MED value is predicted at 6^-.

J^π	$E_{exp^{34}Ar}$	$E_{exp^{34}S}$	E_{th}	MED_{exp}	$MED_{exp}^{Norm.}$	MED_{th}	ΔV_{CM}	ΔE_{ll+ls}	ΔV_{Cr}	ΔV_B
3^-	4513	4624	5622	-111	0	0	0	0	0	0
5^-	5307	5691	6298	-384	-272	-404	-260	-182	1	36
6^-	\	7791	8220	\	\	-375	-275	-167	23	44

Table 4.39: Experimental data and theoretical calculations for the ^{34}Ar and ^{34}S. Idem as in Tab.4.29.

4.3.4 Comment on $T = 1$

The MED analysis highlights a systematic but not fully consistent behaviour of the shell-model predictions. In the lightest case ($A = 20$), the experimental trend is well reproduced, with positive contributions from Coulomb multipole and single-particle terms partially compensated by the negative isospin-breaking correction, leading to a slight theoretical underestimate. At $A = 26$ and $A = 34$, the MED magnitudes become much larger and the model consistently overestimates the experiment, by about 300 keV and 130 keV, respectively. In both cases, the discrepancy originates from the dominance of strongly negative Coulomb multipole and single-particle corrections, which are insufficiently balanced by the positive ISB and radial terms. At $A = 32$, theory predicts a smooth monotonic decrease of MED with spin, in contrast to the experimental pattern that alternates sign between states; here again, the failure arises from the multipole and single-particle components, while V_B and V_{Cr} are negligible. Overall, the calculations capture some qualitative aspects of the MED evolution but tend to exaggerate the absolute magnitudes or even predict the wrong sign, particularly at mid- and high-mass numbers, reflecting the limitations of the effective interaction in treating cross-shell excitations and the fine balance among Coulomb and ISB terms.
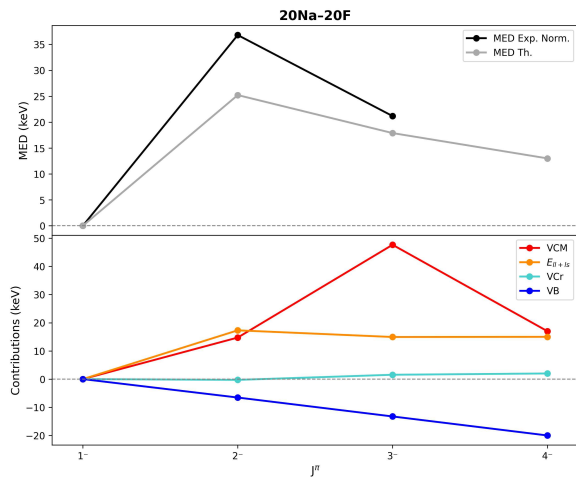
Figure 4.37: **Top panel:** the experimental MED values and theoretical predictions for the ^{20}Na and ^{20}F mirror pair. **Bottom panel:** the different contributions to the theoretical prediction.
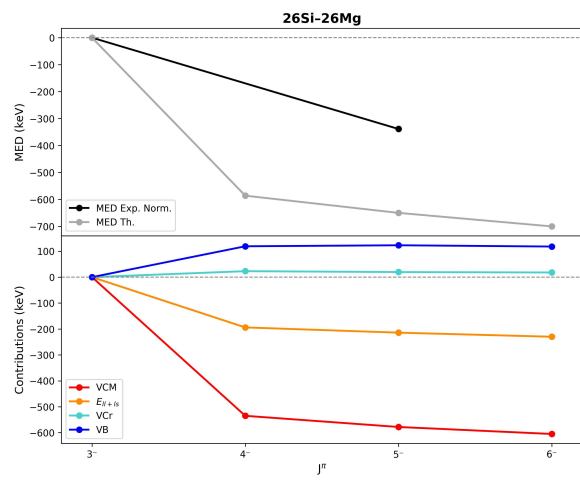

Figure 4.38: **Top panel:** the experimental MED values and theoretical predictions for the ^{26}Si and ^{26}Mg mirror pair. **Bottom panel:** the different contributions to the theoretical prediction.
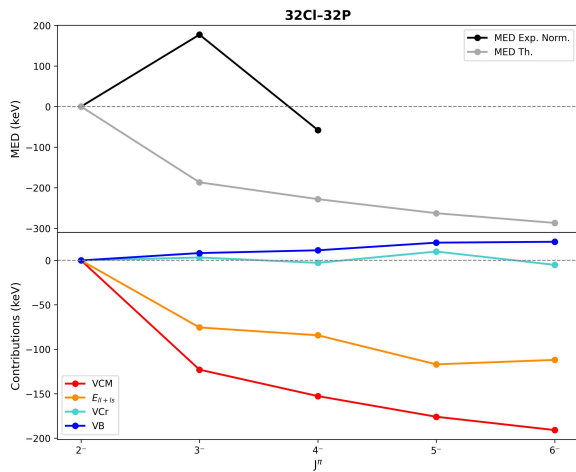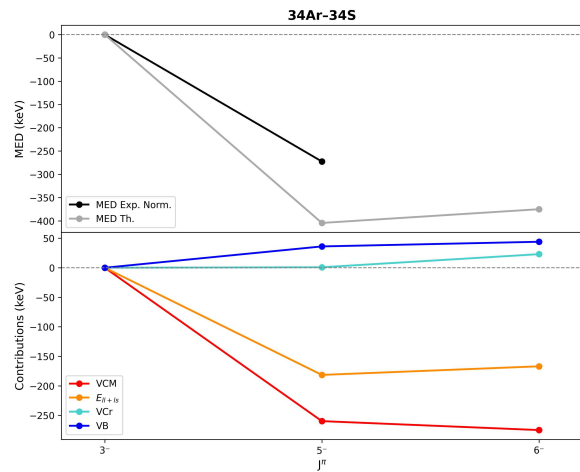

Figure 4.39: **Top panel:** the experimental MED values and theoretical predictions for the ^{32}Cl and ^{32}P mirror pair. **Bottom panel:** the different contributions to the theoretical prediction.

Figure 4.40: **Top panel:** the experimental MED values and theoretical predictions for the ^{34}Ar and ^{34}S mirror pair. **Bottom panel:** the different contributions to the theoretical prediction.

4.3.5 Mirror nuclei with $T = \frac{3}{2}$

Here the net difference $|N - Z| = 3$, so in a mirror pair there are a nucleus with an excess of three protons and the other one has an excess of three neutrons; see Tab. A.3. Furthermore, this means that the analysed nuclei have a strong interest, belonging to the driplines.

A=21 The ^{21}Mg and ^{21}F is the last mirror couple examined. As can be noticed from the Fig.4.41, the prediction of the model is good. The small differences come from the multipole and single-particle terms, which well reproduce the behaviour of experimental data reported in the Tab(4.40). The deviation from can be attributed to the positive isospin-breaking term. In addition, a negative MED value is calculated at $\frac{9}{2}^{-}$.

J^{π}	$E_{exp^{21}\text{Mg}}$	$E_{exp^{21}\text{F}}$	E_{th}	MED_{exp}	$\text{MED}_{\text{exp}}^{Norm.}$	MED_{th}	ΔV_{CM}	$\Delta E_{\text{ll+ls}}$	ΔV_{Cr}	ΔV_B
$1/2^-$	1081	1101	672	-20	0	0	0	0	0	0
$3/2^-$	1989	2040	1844	-51	-31	-22	-25	-15	-3	21
$5/2^-$	2048	2068	1856	-20	0	-17	-9	-7	-5	3
$9/2^-$	\	4055	3741	\	\	-9	-5	-12	4	3

Table 4.40: Experimental data and theoretical calculations for the ^{21}Mg and ^{21}F. Idem as in Tab.4.29.
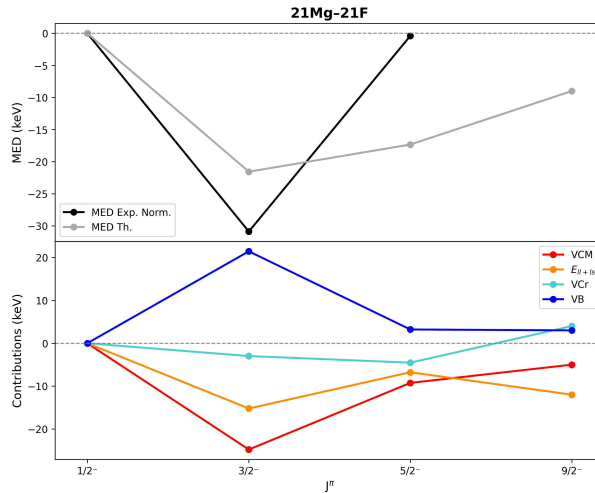

Figure 4.41: **Top panel:** the experimental MED values and theoretical predictions for the ^{21}Mg and ^{21}F mirror pair. **Bottom panel:** the different contributions to the theoretical prediction.

4.4 Final comment on Negative parity states

The analysis of negative-parity MED in the *sd*-shell for $T = \frac{1}{2}$, 1, $\frac{3}{2}$ mirror nuclei highlights both shared features and important differences in the theoretical description. In the $T = \frac{1}{2}$ systems ($A = 19$–35), lighter nuclei ($A = 19, 21$) are well described, with discrepancies of only a few tens of keV, while mid-shell cases such as $A = 25$ and $A = 27$ expose clear failures, including wrong signs and underestimated slopes.

In heavier systems ($A = 31, 35$), the agreement improves again in reproducing staggering or monotonic trends, though deviations at high spin may reach several hundred keV. This reflects the strong influence of cross-shell mixing with the fp-shell and the limits of the restricted valence space at higher spin. In the $T = 1$ mirrors ($A = 20, 26, 32, 34$), the picture is somewhat more

systematic: the $A = 20$ case is well reproduced, but at higher masses the model consistently overestimates the MED magnitude (by 130–300 keV), driven by the dominance of strongly negative Coulomb multipole and single-particle contributions not adequately balanced by the isospin-breaking and radial terms. At $A = 32$, the theory also misses the alternating sign seen in the experimental data, instead predicting a monotonic decrease. These failures point to the limitations of the effective interaction in handling cross-shell excitations and the delicate balance among Coulomb and ISB contributions. The $T = \frac{3}{2}$ case with $A = 21$, shows the best overall agreement: the theoretical MED closely follow experiment, with only small deviations arising from the interplay of multipole and single-particle terms, while the isospin-breaking correction accounts for residual differences.

A common feature are the small values of the radial term, reflecting a nearly constant evolution occupancy of the $f_{\frac{7}{2}}$ orbit and the lower importance of the $s_{\frac{1}{2}}$. In conclusion, while the shell model with cross-shell excitations qualitatively captures the main features of negative-parity MED across all isospins, its quantitative accuracy varies: it is strongest for light or high-isospin systems, but diminishes in mid-shell and high-spin states, where the restricted valence space and insufficient treatment of cross-shell correlations lead to overestimation or incorrect sign of MED values.

4.5 MED results overview

The global comparison of positive- and negative-parity MED in the sd-shell reveals both common patterns and marked differences, strongly connected to the adopted model spaces and the role of cross-shell excitations.

For states of positive parity within the sd-shell valence space, examined using the effective USDA interaction [12], the systematics of the MED are mainly driven by Coulomb monopole and multipole contributions, spin–orbit corrections, and isospin-breaking terms. Radial effects are also present but generally remain modest in comparison.

Theoretical predictions generally succeed in reproducing qualitative behaviours. They capture the staggering or irregular spin dependence in odd-A, $T = \frac{1}{2}$ nuclei, and show good agreement in $T = 1$ systems, except at mid-shell where deviations in sign or magnitude can occur. In addition, they consistently reproduce the smooth trends observed in the $T = \frac{3}{2}$ nuclei and the almost systematic behaviour characteristic of $T = 2$.

Quantitatively, discrepancies generally remain within a few tens of keV, although they may extend to ~ 100 keV at higher spin or in mid-shell nuclei. The principal limitation is rooted in the constrained valence space, which restricts the depiction of cross-shell admixtures and becomes increasingly significant with increased angular momentum and excitation energy.

Negative parity states, studied with the PSDPF interaction [9] in the sd-shell and allow the excitation of only one nucleon from the p shell or to the fp shell, that facilitates p-sd-fp cross-shell mixing, exemplify the intruder nature of these excitations and exhibit a higher sensitivity to proton-neutron asymmetry and shell evolution. The latter comes from the fact that cross-shell excitations directly depend on how the shell gaps evolve with isospin and angular momentum, whereas positive-parity states confined to the sd-shell are comparatively less affected.

Within $T = \frac{1}{2}$ systems, lighter nuclei ($A = 19, 21$) are accurately reproduced, whereas mid-shell nuclei ($A = 25, 27$) demonstrate evident discrepancies, such as incorrect signs and underestimated slopes.

In contrast, heavier nuclei ($A = 31, 35$) exhibit an improved correspondence with trend reproduction, although with significant deviations at high spin.

For $T = 1$, the observed behaviour presents greater uniformity: the lightest case ($A = 20$) is satisfactorily described, but at $A = 26, 32, 34$, the theoretical model consistently overestimates MED magnitudes or fails to capture alternating signs. This is primarily attributed to overly strong Coulomb multipole and single-particle corrections that are insufficiently counterbalanced by ISB contributions.

The $T = \frac{3}{2}$ example ($A = 21$) achieves the highest level of agreement, displaying only minor residual differences.

In all instances involving negative parity, the radial terms are nearly negligible, indicating the limited influence of $s_{1/2}$ occupancy within these intruder configurations, while highlighting the increasing importance of the $f_{7/2}$ orbit as cross-shell excitations become more relevant.

In conclusion, both positive- and negative-parity MED analyses highlight the capability of the shell model to reproduce global qualitative features, but quantitative precision depends on isospin, parity, and mass region. Positive-parity states benefit from more robust interactions within the sd valence space, while negative-parity states expose the fragility of the model under strong cross-shell mixing, particularly at mid-shell and high spin.

Since no best fit has been performed, the only two free parameters available, namely the radial and the isospin-breaking ones, are insufficient to improve the analysis for high-spin states, where there is competition between excitation energies and promotion of nucleons from the core.

The common thread in both cases is the limitation of effective interactions: the restricted model space and the approximate treatment of cross-shell correlations systematically emerge as the main source of discrepancies, either as overestimation, wrong slopes, or incorrect MED sign.

The USDA allows multiparticle excitation within the *sd*-shell only, cutting over lower and higher orbits, while the PSDPF has a large valence space but permits only single-particle excitation. This underlines the need for refined effective interactions that better incorporate cross-shell dynamics. However, it should be considered that the lack of suitable effective interactions in this field is also due to the ease with which computational complexity grows with increasing valence spaces and the number of nucleons that can be excited.

Chapter 5

Conclusions and future directions

Isospin symmetry is a cornerstone of nuclear structure theory. In the limit where only the strong nuclear interaction is considered, it requires that the excitation energy spectra of mirror nuclei be identical. The inclusion of the Coulomb interaction, which acts exclusively among protons, induces a breaking of this symmetry.

In this context, the study of Mirror Energy Differences, defined as the excitation energy differences between analogue states in mirror nuclei, provides a sensitive probe of the underlying shell-model structure. In particular, within the sd-shell, MED analyses offer direct insights into the interplay between Coulomb effects, configuration mixing, and possible isospin-nonconserving components of the effective nuclear interaction.

This work has presented, for the first time within this framework, a systematic analysis Mirror Energy Differences of 29 pairs of light and medium-mass nuclei ($A = 19$–35) belonging to the sd-shell. By exploiting the sensitivity of MED to subtle structural effects, we have shown how these observables act as a magnifying lens for the microscopic properties of excited states, bringing to light key features of nuclear structure such as nucleon–nucleon pairing correlations and the mechanisms driving structural evolution with angular momentum and nuclear radius.

A distinctive element of this study is the simultaneous treatment of both natural-parity positive states within the sd-shell and negative-parity intruder states, the latter arising from cross-shell excitations either from the p to the sd shell or from the sd to the fp shell. The analysis was carried out using the full set of available experimental data, covering nuclei with isospin values of up to $T = 2$ for positive parity and up to $T = 3/2$ for negative parity, beyond which the scarcity of observed states, prevents a systematic approach.

The theoretical framework, originally developed for fp-shell nuclei, proves to be generally robust in the sd region, successfully reproducing the main experimental trends. Deviations, particularly for high-spin states, highlight the intrinsic limitations of the effective interaction, most notably the restricted model space. This truncation effectively imposes a cut-off on the system's degrees of freedom, reducing the fraction of the wave function associated with orbitals outside the valence space. Such effects become crucial in describing MED at high angular momentum, where competition with core excitations emerges. This observation represents a distinctive feature of sd-shell nuclei, as systematic fp-shell analyses have not revealed comparable behaviour, probably due to the larger valence space and the dominance of the $f_{7/2}$ orbital in fp-shell wave functions, see [2, 3].

From a quantitative perspective, the present study also indicates that the single-particle energy corrections in the sd-shell are significantly larger than those reported in fp-shell investigations, marking another important structural difference between the two mass regions.

Furthermore, by adopting recently refined radial and isospin-breaking parameters, the present calculations not only reproduce known experimental trends but also enable predictions of MED for states yet unobserved experimentally.

These results pave the way for several natural extensions. In particular, the mass range under investigation can be extended both toward the sd-shell closure at $A = 40$ and toward lighter nuclei ($A = 17$–18), employing effective interactions other than USDA or PSDPF. A further line of development is the systematic study of Triplet Energy Differences (TED) across $A = 18$–38, thus testing not only charge symmetry (as done with MED) but also charge independence of the nuclear force.

In addition, the accuracy of the calculations presented here suggests that MED can be exploited not only to interpret known spectra, but also to extrapolate the excitation spectrum of mirror partners that remain experimentally inaccessible. In fact, as observed in this study, the theoretical trends generally reproduce the experimental behaviour, thus allowing one to hypothesise or even partially reconstruct the level scheme of unknown mirrors. This aspect is particularly relevant for nuclei of astrophysical interest produced in the rp-process, many of which are located near the proton dripline, where their intrinsic instability makes γ-decay competitive with proton emission. In this context, the investigation of mirror nuclei represents a promising direction, especially considering the role of sd-shell nuclei in nuclear astrophysics, both in explosive stellar environments such as novae and supernovae and in the nucleosynthesis processes (rp-, r-, and s-processes) responsible for the synthesis of heavier elements. Extensive studies on sd-shell nuclei of astrophysical relevance have been reported in [22, 37, 40, 43].

A further benchmark for the study of valence-space configurations, in both natural and unnatural parity states, is provided by electromagnetic transition probabilities, which are more directly sensitive to the underlying wave functions. Here, isospin symmetry imposes strict selection rules. For instance, in the limit of good isospin conservation, the B(E1) values in mirror pairs should be identical, since the multipole operator decomposes into isoscalar and isovector components, with the isoscalar contributions expected to cancel out, see [39]. Consequently, measurements of transition probabilities and lifetimes in mirror nuclei offer a stringent test of both the theoretical description and the degree of isospin symmetry conservation, complementing the insights obtained from MED systematics.

Appendix A

List of studied mirror nuclei

In this Appendix are reported all the mirror nuclei studied in this thesis. These are ordered by their isospin $T = \frac{1}{2}, 1, \frac{3}{2}, 2$. All nuclei disposed along the same line ($Z_>$, $Z_<$) are isodiaphers. In the tables are present all the masses related to the positive parity states, while only a subset of them furnished a valuable set of negative parity states, due to the unnatural parity[1] of these intruder states. Negative parity states were studied only for the masses signed in bold type.

		$T = 1/2$							
A	19	**21**	**23**	25	**27**	29	**31**	33	**35**
$Z_>$	$^{19}_{10}Ne_9$	$^{21}_{11}Na_{10}$	$^{23}_{12}Mg_{11}$	$^{25}_{13}Al_{12}$	$^{27}_{14}Si_{13}$	$^{29}_{15}P_{14}$	$^{31}_{16}S_{15}$	$^{33}_{17}Cl_{16}$	$^{35}_{18}Ar_{17}$
$Z_<$	$^{19}_{9}F_{10}$	$^{21}_{10}Ne_{11}$	$^{23}_{11}Na_{12}$	$^{25}_{12}Mg_{13}$	$^{27}_{13}Al_{14}$	$^{29}_{14}Si_{15}$	$^{31}_{15}P_{16}$	$^{33}_{16}S_{17}$	$^{35}_{17}Cl_{18}$

Table A.1: $T = \frac{1}{2}$ mirror nuclei.

			$T = 1$					
A	**20**	22	24	**26**	28	30	**32**	**34**
$Z_>$	$^{20}_{11}Na_9$	$^{22}_{12}Mg_{10}$	$^{24}_{13}Al_{11}$	$^{26}_{14}Si_{12}$	$^{28}_{15}P_{13}$	$^{30}_{16}S_{14}$	$^{32}_{17}Cl_{15}$	$^{34}_{18}Ar_{16}$
$Z_<$	$^{20}_{9}F_{11}$	$^{22}_{10}Ne_{12}$	$^{24}_{11}Na_{13}$	$^{26}_{12}Mg_{14}$	$^{28}_{13}Al_{15}$	$^{30}_{14}Si_{16}$	$^{32}_{15}P_{17}$	$^{34}_{16}S_{18}$

Table A.2: $T = 1$ mirror nuclei.

			$T = 3/2$				
A	**21**	23	25	27	29	31	33
$Z_>$	$^{21}_{12}Mg_9$	$^{23}_{13}Al_{10}$	$^{25}_{14}Si_{11}$	$^{27}_{15}P_{12}$	$^{29}_{16}S_{13}$	$^{31}_{17}Cl_{14}$	$^{33}_{18}Ar_{15}$
$Z_<$	$^{21}_{9}F_{12}$	$^{23}_{10}Ne_{13}$	$^{25}_{11}Na_{14}$	$^{27}_{12}Mg_{15}$	$^{29}_{13}Al_{16}$	$^{31}_{14}Si_{17}$	$^{33}_{15}P_{18}$

Table A.3: $T = \frac{3}{2}$ mirror nuclei.

---

[1]Studying $sd-$shell, the natural parity of the states is the positive one.

		$T = 2$			
A	22	24	28	32	34
$Z_>$	$^{22}_{13}Al_9$	$^{24}_{14}Si_{10}$	$^{28}_{16}S_{12}$	$^{32}_{18}Ar_{14}$	$^{34}_{19}K_{15}$
$Z_<$	$^{22}_{9}F_{13}$	$^{24}_{10}Ne_{14}$	$^{28}_{12}Mg_{16}$	$^{32}_{14}Si_{18}$	$^{34}_{15}P_{19}$

Table A.4: $T = 2$ mirror nuclei.

Bibliography

[1]   N. Auerbach. "Isospin in nuclear physics". In: *Physics Reports* 98 (1983), pp. 273–326. DOI: 10.1016/0370-1573(83)90082-7.

[2]   M. A. Bentley et al. "Isospin-breaking interactions studied through mirror energy differences". In: *Physical Review C* 92 (2015), p. 024310. DOI: 10.1103/PhysRevC.92.024310.

[3]   M.A. Bentley and S.M. Lenzi. "Coulomb energy differences between high-spin states in isobaric multiplets". In: *Progress in Particle and Nuclear Physics* 59.2 (2007), pp. 497–561. ISSN: 0146-6410. DOI: https://doi.org/10.1016/j.ppnp.2006.10.001. URL: https://www.sciencedirect.com/science/article/pii/S0146641006000743.

[4]   Michael A Bentley. "Excited States in Isobaric Multiplets—Experimental Advances and the Shell-Model Approach". In: *Physics* 4.3 (2022), pp. 995–1011. ISSN: 2624-8174. DOI: 10.3390/physics4030066. URL: https://www.mdpi.com/2624-8174/4/3/66.

[5]   A. Bohr and B. R. Mottelson. *Nuclear Structure (In 2 Volumes)*. World Scientific Publishing Company, 1998. ISBN: 9789813105126. URL: https://books.google.it/books?id=NNZQDQAAQBAJ.

[6]   J. Bonnard, S. M. Lenzi, and A. P. Zuker. "Neutron Skins and Halo Orbits in the *sd* and *pf* shells". In: *Physical Review Letters* 116.21 (2016), p. 212501. DOI: 10.1103/PhysRevLett.116.212501. arXiv: 1601.02168 [nucl-th].

[7]   A. Boso et al. "Neutron Skin Effects in Mirror Energy Differences: The Case of ^{23}Mg–^{23}Na". In: *Physical Review Letters* 121 (2018), p. 032502. DOI: 10.1103/PhysRevLett.121.032502.

[8]   Alberto Boso. "Study of Isospin Symmetry Breaking effects in the A=23 and A=46 multiplets". PhD thesis. U. Padua (main), 2017.

[9]   M. Bouhelal et al. "A PSDPF interaction to describe the 1 $\hbar\omega$ intruder states in sd shell nuclei". In: *Nucl. Phys. A* 864 (2011), pp. 113–127. DOI: 10.1016/j.nuclphysa.2011.06.026.

[10]   J. Britz, A. Pape, and M. S. Antony. "Mass excesses and nuclear structure". In: *Atomic Data and Nuclear Data Tables* 69 (1998), pp. 125–157. DOI: 10.1006/adnd.1998.0785.

[11]   B. A. Brown and B. H. Wildenthal. "Status of the Nuclear Shell Model". In: *Annual Review of Nuclear and Particle Science* 38 (1988), pp. 29–66. DOI: 10.1146/annurev.ns.38.120188.000333.

[12]   B. Alex Brown and W. A. Richter. "New "USD" Hamiltonians for the sd shell". In: *Physical Review C* 74.3 (2006), p. 034315. DOI: 10.1103/PhysRevC.74.034315. URL: https://link.aps.org/doi/10.1103/PhysRevC.74.034315.

[13]   P. J. Brussaard and P. W. M. Glaudemans. *Shell-Model Applications in Nuclear Spectroscopy*. Amsterdam: North-Holland, 1977. ISBN: 978-0-7204-2831-2.

[14]   E. Caurier et al. "The shell model as a unified view of nuclear structure". In: *Reviews of Modern Physics* 77.2 (2005), pp. 427–488. DOI: 10.1103/RevModPhys.77.427. URL: https://doi.org/10.1103/revmodphys.77.427.

[15] Etienne Caurier and Frederic Nowacki. "Present Status of Shell Model Techniques". In: *Acta Physica Polonica B* 30.3 (1999), p. 705.

[16] National Nuclear Data Center. *Data extracted using the National Nuclear Data Center World Wide Web site from the evaluated nuclear structure data file.* n.d. URL: `https://www.nndc.bnl.gov/ensdf/`.

[17] J. Duflo and A. P. Zuker. "Microscopic mass formulas". In: *Physical Review C* 66 (2002), p. 051304. DOI: `10.1103/PhysRevC.66.051304`.

[18] J. Duflo and A. P. Zuker. "Mirror displacement energies and neutron skins". In: *Physical Review C* 66.5 (2002). DOI: `10.1103/PhysRevC.66.051304`. URL: `https://doi.org/10.1103/PhysRevC.66.051304`.

[19] J. Ekman et al. "Evidence of $N = 34$ Subshell Closure from the Level Structure of ^{54}Ti". In: *Physical Review Letters* 92 (2004), p. 132502. DOI: `10.1103/PhysRevLett.92.132502`.

[20] A. Frank, J. Jolie, and P. Van Isacker. *Symmetries in Atomic Nuclei.* Heidelberg: Springer-Verlag, 2009. ISBN: 978-3-540-76388-3. DOI: `10.1007/978-3-540-76388-3`.

[21] E. Gapon and D. Iwanenko. "Zur Bestimmung der Isotopenzahl". In: *Naturwissenschaften* 20.43 (1932), pp. 792–793. DOI: `10.1007/BF01494007`.

[22] J. Grineviciute, B. A. Brown, and H. Schatz. "The role of excited states in the rp-process for sd-shell nuclei". In: *arXiv e-prints* (2014). eprint: `1404.7268`. URL: `https://arxiv.org/abs/1404.7268`.

[23] Otto Haxel, J. Hans D. Jensen, and Hans E. Suess. "On the "Magic Numbers" in Nuclear Structure". In: *Physical Review* 75.11 (1949), p. 1766. DOI: `10.1103/PhysRev.75.1766.2`. URL: `https://link.aps.org/doi/10.1103/PhysRev.75.1766.2`.

[24] K. Heyde. *Basic Ideas and Concepts in Nuclear Physics.* Dirac House, Temple Back, Bristol BS1 6BE, UK: Institute of Physics Publishing, 1994.

[25] K. Heyde. *The Nuclear Shell Model.* Heidelberg: Springer-Verlag, 2004.

[26] D. R. Inglis. "Nuclear Moments of Inertia due to Nucleon Motion in a Rotating Well". In: *Phys. Rev.* 103 (6 Sept. 1956), pp. 1786–1795. DOI: `10.1103/PhysRev.103.1786`. URL: `https://link.aps.org/doi/10.1103/PhysRev.103.1786`.

[27] K. Kaneko et al. "Variation in Displacement Energies Due to Isospin-Nonconserving Forces". In: *Physical Review Letters* 110 (2013), p. 172505. DOI: `10.1103/PhysRevLett.110.172505`.

[28] Y.L. Lam. "Isospin Symmetry Breaking in sd Shell Nuclei". Theses. Université de Bordeaux1, Dec. 2011. URL: `https://theses.hal.science/tel-00777498`.

[29] Cornelius Lanczos. "An iteration method for the solution of the eigenvalue problem of linear differential and integral operators". In: *Journal of Research of the National Bureau of Standards* 45 (1950), pp. 255–282.

[30] S. M. Lenzi et al. "Shape Coexistence in ^{36}S and the Onset of Deformation in the $N = 20$ Region". In: *Physical Review Letters* 87 (2001), p. 122501. DOI: `10.1103/PhysRevLett.87.122501`.

[31] Silvia Lenzi and R Lau. "A systematic study of mirror and triplet energy differences". In: *Journal of Physics: Conference Series* 580 (Feb. 2015), p. 012028. DOI: `10.1088/1742-6596/580/1/012028`.

[32] Maria Goeppert Mayer. "On Closed Shells in Nuclei. II". In: *Physical Review* 75.12 (1949), pp. 1969–1970. DOI: `10.1103/PhysRev.75.1969`. URL: `https://link.aps.org/doi/10.1103/PhysRev.75.1969`.

[33] G. A. Miller. "Charge Symmetry Breaking and QCD". In: *Chinese Journal of Physics* 32 (1994), pp. 1075–1084.

[34] W. D. Myers and W. J. Swiatecki. "Nuclear masses and deformations". In: *Nuclear Physics* 81 (1966), pp. 1–60. DOI: 10.1016/0029-5582(66)90639-4.

[35] J. A. Nolen and J. P. Schiffer. "Coulomb Energies". In: *Annual Review of Nuclear Science* 19 (1969), pp. 471–526. DOI: 10.1146/annurev.ns.19.120169.002343.

[36] *NuDat 3.0: Search and plot nuclear structure and decay data interactively.* https://www.nndc.bnl.gov/nudat3/. 2025.

[37] T. Oda et al. "Rate Tables for the Weak Processes of sd-Shell Nuclei in Stellar Matter". In: *Atomic Data and Nuclear Data Tables* 56 (1994), pp. 231–403. DOI: 10.1006/adnd.1994.1007.

[38] W. E. Ormand and B. A. Brown. "Shell-model calculations for the $1s0d$-$0p$ cross-shell interaction". In: *Nuclear Physics A* 491 (1989), pp. 1–30. DOI: 10.1016/0375-9474(89)90338-7.

[39] F. Recchia and AGATA Collaboration. "Electric Dipole Transitions in Mirror Nuclei". In: *AGATA Collaboration Meeting.* Conference presentation. INFN, Italy, 2024. URL: https://agenda.infn.it/event/47146/contributions/270584/attachments/138099/207703/AGATA_19Ne.pdf.

[40] W. A. Richter and B. A. Brown. "Calculation of rp-Process Rates in the sd Shell via the Nuclear Shell Model". In: *Progress of Theoretical Physics Supplement* 196 (2012), pp. 340–345. DOI: 10.1143/PTPS.196.340.

[41] Anwer Al-Sammarraie. "NUCLEAR SHELL STRUCTURE OF ODD-A MAGNESIUM ISOTOPES WITHIN USDA HAMILTONIAN". PhD thesis. Oct. 2015. DOI: 10.13140/RG.2.2.28606.84804.

[42] M. H. Shahnas, H. S. Sherif, and R. S. Mackintosh. "Isospin mixing and Coulomb displacement energies in the $1p-2s1d$ shell nuclei". In: *Physical Review C* 50 (1994), pp. 2346–2354. DOI: 10.1103/PhysRevC.50.2346.

[43] T. Suzuki, H. Toki, and K. Nomoto. "Electron capture and beta-decay rates for sd-shell nuclei in stellar environments relevant to high density O-Ne-Mg cores". In: *arXiv e-prints* (2015). eprint: 1512.00132. URL: https://arxiv.org/abs/1512.00132.

[44] M. Taketani. In: *Progress of Theoretical Physics Supplement* 3 (1956), p. 1.

[45] F. D. Vedova. "Isospin Symmetry in the *sd* Shell: The A=31 and A=35 Mirror Nuclei". PhD thesis. Padua, Italy: University of Padua, 2004.

[46] D. D. Warner, M. A. Bentley, and P. Van Isacker. "The role of isospin symmetry in collective nuclear structure". In: *Nature Physics* 2 (2006), pp. 311–318. DOI: 10.1038/nphys291. URL: https://doi.org/10.1038/nphys291.

[47] D. D. Warner, M. A. Bentley, and P. Van Isacker. "The role of isospin symmetry in nuclear physics". In: *Nature Physics* 2 (2006), pp. 311–318. DOI: 10.1038/nphys305.

[48] W. Weise. In: *Progress of Theoretical Physics Supplement* 170 (2007), p. 161.

[49] Andreas Wendt. "Isospin symmetry in the sd shell: Coulomb excitation of ^{33}Ar at relativistic energies and the new 'Lund-York-Cologne-Calorimeter'". PhD thesis. Universität zu Köln, 2013.

[50] R. R. Whitehead et al. "Computational Methods for Shell-Model Calculations". In: *Advances in Nuclear Physics.* Ed. by Michel Baranger and Erich Vogt. Boston, MA: Springer US, 1977, pp. 123–176. ISBN: 978-1-4615-8234-2. DOI: 10.1007/978-1-4615-8234-2_2. URL: https://doi.org/10.1007/978-1-4615-8234-2_2.

[51] E. P. Wigner. *Proceedings of the Robert A. Welch Foundation Conference on Chemical Research.* 1957.

[52] A. P. Zuker et al. "Isobaric Multiplet Mass Equation: A Tool for Nuclear Physics". In: *Physical Review Letters* 89 (2002), p. 142502. DOI: 10.1103/PhysRevLett.89.142502.

Acknowledgements